On Quantum Information, Thermalization and Gravity

Oleg Kaikov

München 2023

On Quantum Information, Thermalization and Gravity

Oleg Kaikov

Dissertation
an der Fakultät für Physik
der Ludwig-Maximilians-Universität
München

vorgelegt von
Oleg Kaikov
aus Sankt Petersburg, Russland

München, den 22. August 2023

Erstgutachter: Prof. Dr. Georgi Dvali
Zweitgutachter: Prof. Dr. Andreas Weiler
Tag der mündlichen Prüfung: 17. Oktober 2023

Zusammenfassung

Das Verständnis des Ursprungs der informationsprozessierenden Eigenschaften Schwarzer Löcher auf mikroskopischem Niveau ist eine fundamentale Forschungsrichtung in der Physik. Aufgrund dessen, wie sie sich zeitlich entwickeln und Quanteninformation speichern, werden Schwarze Löcher oft als einzigartig betrachtet. Jedoch wurde vor kurzem vorgeschlagen, dass bestimmte Objekte, sogenannte *Saturons*, oder Saturonen (von engl. „to saturate“ – sättigen), die gleichen Eigenschaften wie Schwarze Löcher universell aufweisen. Saturonen sind Objekte, die die maximale Entropie besitzen, die von der Unitarität innerhalb deren jeweiligen Theorien zugelassen ist.

In dieser Dissertation wird zunächst diese Schwarzes Loch–Saturon-Korrespondenz innerhalb einer renormierbaren $SU(N)$-symmetrischen Theorie verifiziert. Wir zeigen, dass das Spektrum dieser Theorie eine Reihe von Energieeigenzuständen in Form von Blasen beinhaltet, die gebundene Zustände aus $SU(N)$-Goldstone-Bosonen darstellen. Trotz der Abwesenheit von Gravitation in dieser Theorie weist eine gesättigte Blase die informationsprozessierenden Merkmale eines Schwarzen Loches auf: deren Entropie ist durch das Bekenstein-Hawking-Flächengesetz gegeben; semiklassisch besitzt sie einen strikten Informationshorizont, evaporiert mit einer thermalen Rate bei einer Temperatur, die zum Kehrwert deren Radius proportional ist; und die minimale Zeit für den Start der Informationsgewinnung ist gleich der Page-Zeit. Diese Schwarzes Loch–Saturon-Korrespondenz zeigt, dass die genannten informationsprozessierenden Charakteristiken nicht spezifisch für Schwarze Löcher oder Gravitation sind. Stattdessen liegt der fundamentale Ursprung dieser Eigenschaften generischer Saturonen in der Sättigung der Unitaritätsgrenzen in den jeweiligen Theorien.

Als nächstes wird der Prozess der Diffusion oder des „Prescrambling“ (von engl. „to scramble“ – vermischen) der Information innerhalb eines mikroskopischen Systems, das zur Modellierung der Einspeicherung und Prozessierung von Information in Schwarzen Löchern entworfen wurde, analysiert. Dementsprechend ist dieses Prototypsystem imstande, große Mengen von Quanteninformation einzuspeichern, da es eine erweiterte Speicherkapazität besitzt. Wir untersuchen die frühzeitige Dynamik des Systems auf Zeitskalen vor Stattfinden des Scrambling, wobei wir die allgemeinste Definition des letzteren verwenden. Obwohl die Zeitentwicklung des Systems unitär ist, breitet sich dessen Zustand allmählich über den gesamten Zustandsraum aus und wird dadurch vermischt. Wir definieren ein Maß für Prescrambling mithilfe einer minimalen Wahrscheinlichkeitsschwelle für die Zustände im Hilbertraum des Systems. Aufgrund unserer Erkenntnisse können einige Vermutungen

über generische Quantensysteme, einschließlich Schwarzer Löcher, aufgestellt werden. Insbesondere weisen unsere Ergebnisse darauf hin, dass die schnellsten Prescrambler eine in der Anzahl ihrer Freiheitsgrade logarithmische Zeit benötigen, dass das untersuchte Prototypmodell ein schneller Prescrambler ist und dass Schwarze Löcher schnelle Prescrambler sind.

Als letztes wird die Thermalisierung innerhalb des selben Prototypsystems, das in einem reinen Anfangszustand $|\text{in}\rangle$ weit vom Gleichgewichtszustand präpariert wurde, untersucht. Insbesondere schlagen wir einen neuen expliziten Mechanismus vor, mittels dessen die Wenigteilchenobservablen innerhalb dieses isolierten Quantensystems unter einer unitären Zeitentwicklung zu ihren statistischen Ensemblemittlewerten ins Gleichgewicht gebracht werden. Die Neuheit dieses Mechanismus ist das Auftreten von Thermalisierung trotz der Korrelationen zwischen den Fluktuationen der Eigenzustandserwartungswerte $\langle\alpha|\,\hat{A}\,|\alpha\rangle$ einer Wenigteilchenobservablen und den Fluktuationen der Koeffizient-Quadraten $|C_\alpha|^2 = |\,\langle\alpha|\text{in}\rangle\,|^2$.

Wir diskutieren die Auswirkungen unserer Erkenntnisse auf die Physik Schwarzer Löcher und isolierter Quantensysteme, sowohl im Sinne deren fundamentalen Verständnisses als auch im Bezug auf mögliche Beobachtungen.

Abstract

Understanding the origin of information-processing properties of black holes at a microscopic level is a fundamental direction of research in physics. Black holes are often regarded as unique due to how they evolve in time and store quantum information. However, it was recently proposed that these properties are universally exhibited by certain objects, the so-called saturons, that possess the maximal entropy permitted by unitarity within their respective theories.

In this dissertation we first verify this black hole–saturon correspondence within a renormalizable $SU(N)$-symmetric theory. We demonstrate that the spectrum of the theory contains a tower of bubbles representing bound states of $SU(N)$ Goldstone bosons. Despite the absence of gravity in this theory, a saturated bubble exhibits the information-processing features of a black hole: Its entropy is given by the Bekenstein-Hawking area-law formula; semiclassically, it possesses a strict information horizon and evaporates at a thermal rate with a temperature proportional to its inverse radius; and the minimum time for the start of information retrieval is equal to the Page time. This black hole–saturon correspondence provides evidence that the above information-processing characteristics are not specific to black holes or gravity. Instead, the fundamental origin of these properties for generic saturons lies in the saturation of the unitarity bounds by the respective theories.

Next, we study the process of diffusion or "prescrambling" of information within a microscopic system designed to model how a black hole stores and processes information. Correspondingly, this prototype system is able to store large amounts of quantum information, that is, it possesses an enhanced memory capacity. We study the early-time dynamics of the system on timescales before scrambling for the most general definition of the latter. Although the time-evolution of the system is unitary, its state gradually spreads over the entire state space and is thus scrambled. We define a measure for prescrambling in terms of a minimum probability threshold for the states in the Hilbert space of the system. Our findings lead us to propose a set of conjectures for generic quantum systems, including black holes. In particular, these state that the most rapid prescramblers take a time logarithmic in the number of degrees of freedom, that the investigated prototype model is a fast prescrambler and that black holes are fast prescramblers.

Last, we consider thermalization within the same prototype system prepared in a pure initial state $|\text{in}\rangle$ far from equilibrium. Specifically, we propose a new explicit mechanism via which under unitary time-evolution few-body observables equilibrate to their statistical ensemble averages within this isolated quantum system. The novelty is the occurrence of

thermalization despite correlations between the fluctuations of the eigenstate expectation values $\langle\alpha|\,\hat{A}\,|\alpha\rangle$ of a few-body observable and the fluctuations of the coefficients-squared $|C_\alpha|^2 = |\,\langle\alpha|\text{in}\rangle\,|^2$.

We discuss the implications of our findings for black hole physics as well as for isolated quantum systems, both fundamental and observational.

Contents

Publications and Projects

This dissertation is based predominantly on the papers that have been published [1, 2] or are in preparation [3]. These are a subset of projects, completed and ongoing, in various collaborations and as a single author, as detailed below. In collaborative papers, all authors share principal authorship and are listed alphabetically by convention in particle physics.

Although some new aspects were added throughout, the purpose of this work is to provide the corresponding necessary background, present these results in a wider context and incorporate them into a unified picture. Therefore, the present dissertation is, to a large extent, a *verbatim* reproduction with respect to text, equations, figures and tables of the papers [1–3], on which the chapters 2, 3 and 4 are based, respectively.

Additionally, chapter 5 includes an outlook on [4] and [5]. Finally, appendix A is an exact reproduction of the appendices of [2, 3].

Published papers:

[1] G. Dvali, O. Kaikov, and J. S. Valbuena-Bermúdez, *How special are black holes? Correspondence with objects saturating unitarity bounds in generic theories*, Phys. Rev. D **105**, 056013 (2022).

[2] O. Kaikov, *Fast prescramblers*, Phys. Rev. D **107**, 116008 (2023).

Ongoing projects:

[3] O. Kaikov, *Thermalization despite correlation*, in preparation.

[4] G. Dvali, O. Kaikov, F. Kühnel, and J. S. Valbuena-Bermúdez, in preparation.

[5] G. Dvali, O. Kaikov, H. Liu, and J. S. Valbuena-Bermúdez, in preparation.

List of Abbreviations

BEC	Bose-Einstein condensate
BHM	Bose-Hubbard model
CGC	Color-glass condensate
ERH	Eigenstate Randomization Hypothesis
ETH	Eigenstate Thermalization Hypothesis
QCD	Quantum Chromodynamics
TDL	Thermodynamic limit
RMSE	Root-mean-square error
SO(N)	Special orthogonal group of degree N
SSB	Spontaneous symmetry breaking
SU(N)	Special unitary group of degree N
SYK	Sachdev-Ye-Kitaev
U(N)	Unitary group of degree N

Chapter 1

Introduction

1.1 Invitation

The main focus of the present dissertation is to further improve the understanding of the information-processing characteristics of black holes. We review these features in the corresponding sections below. This brief section serves the purpose of an overview of the general picture. The current work approaches the task at hand from two directions: First, we consider a renormalizable, non-gravitational theory in which we demonstrate the existence of objects that exhibit the same properties as those of black holes. Second, we consider a specific microscopic prototype model of a black hole. In this quantum setting we investigate the dynamics of how the state of the system evolves over time and how the information within it is processed.

On the one hand our goal is to expand the existing notions concerning black holes to other, in particular non-gravitational, theories. This allows us to provide further evidence that the known black hole features are not specific to gravity. We can thus explain the origin of black hole properties at a more fundamental level. On the other hand, our aim is to suggest new implications and hypotheses for black hole physics. Ultimately, the intention is to propose novel mechanisms and phenomena that could, ideally, be tested in a real setting on cosmological black holes at some point in the future, or, what is currently more realistic, to be tested in simulations and in laboratory experiments on systems of ultracold bosons with attractive interactions, or on analogue systems of black holes.

1.2 Conventions

We use the following conventions throughout the present work. We set $c = k_{\mathrm{B}} = \hbar = 1$, unless explicitly stated otherwise. Here, c is the speed of light, k_{B} is the Boltzmann constant and $\hbar$ is the reduced Planck constant. We denote Newton's gravitational constant by G_{N}. Correspondingly, the Planck length is given by $L_{\mathrm{P}} = \sqrt{\hbar G_{\mathrm{N}}/c^3}$ and the Planck mass is given by $M_{\mathrm{P}} = \sqrt{\hbar c/G_{\mathrm{N}}}$. The metric signature convention in four spacetime dimensions

is given by $(+,-,-,-)$. The general scaling in equations where the specific numerical factors are unimportant is denoted by "$\sim$". Where applicable, for brevity, we denote by "H.c." the Hermitian conjugate of an operator that follows that operator itself.

1.3 Black holes

Black holes are undoubtedly some of the most fascinating objects in the universe. As the core results of the present thesis are relevant for black holes, we review some of their properties below to establish an appropriate foundation. In Schwarzschild coordinates (t, r, θ, ϕ) the Schwarzschild black hole solution [6, 7] of the equations of Einstein's theory of general relativity is given by the line element

$$\mathrm{d}s^2 = \left(1 - \frac{R_\mathrm{S}}{r}\right) \mathrm{d}t^2 - \left(1 - \frac{R_\mathrm{S}}{r}\right)^{-1} \mathrm{d}r^2 - r^2\, \mathrm{d}\Omega^2, \tag{1.1}$$

where

$$R_\mathrm{S} = 2G_\mathrm{N}M \tag{1.2}$$

is the Schwarzschild radius of the black hole, M is its mass and $\mathrm{d}\Omega^2 = (\mathrm{d}\theta^2 + \sin^2\theta\, \mathrm{d}\phi^2)$ is the metric on the two-sphere. The Schwarzschild radius determines the event horizon of the black hole. The corresponding spacetime hypersurface represents a sphere from within which light can no longer escape the gravitational field.

The suggestion that black holes must have an entropy, which is given by [8, 9]

$$S = \frac{\pi R_\mathrm{S}^2}{\hbar G_\mathrm{N}}, \tag{1.3}$$

has further stimulated the interest in how these objects process and store information. In relation to subsequent sections, for convenience, we can express the entropy in Eq. (1.3) in terms of the area of the black hole's event horizon $A = 4\pi R_\mathrm{S}^2$ in units of Planck area L_P^2 as

$$S = \frac{A}{4L_\mathrm{P}^2}. \tag{1.4}$$

A further discovery that black holes must radiate [9, 10] has sparked a long-standing debate [11, 12], dubbed the famous Hawking's "information paradox". The apparent paradox arises due to the assumption that during the full course of its evaporation, a black hole can be treated classically. Consequently, the radiation is assumed to be exactly thermal during the entire evaporation process, leading to loss of information and, therefore, to an apparent violation of unitarity by black holes. However, in a fully quantum theory of a black hole the non-thermal corrections to its Hawking radiation are non-negligible [13]. Specifically, the corrections are suppressed by the inverse powers of entropy [14–17].

Hawking's computations [9, 10] were performed in the semiclassical limit where quantum fields evolve on the background of a fixed classical metric. Therefore, there is no

backreaction of the quantum fields on the black hole. This double-scaling limit is uniquely given by [13]

$$M \to \infty, \quad G_{\rm N} \to 0, \quad \text{but } R_{\rm S} \sim G_{\rm N} M \text{ finite}, \quad \hbar \neq 0. \tag{1.5}$$

In this limit there is no backreaction and the black hole radiates exactly thermally with a Hawking temperature of

$$T = \frac{\hbar}{8\pi G_{\rm N} M}. \tag{1.6}$$

Note from Eq. (1.3) that, consistently with the fact that there is no backreaction, the entropy of the black hole is infinite, $S \to \infty$. For completeness, let us note from Eqs. (1.3) and (1.6) that, as expected, in the classical limit

$$\hbar \to 0, \tag{1.7}$$

the entropy is also infinite, but the black hole does not emit radiation, $T \to 0$.

Only in the fully quantum picture, where $M < \infty$, $G_{\rm N} \neq 0$ and $\hbar \neq 0$ (and hence $S < \infty$), are there non-thermal corrections to the radiation spectrum emitted from the black hole. In [13] it was argued that for a Schwarzschild black hole of entropy S, the non-thermal corrections to its Hawking radiation temperature scale as $\sim 1/S$ in the leading order approximation.

1.4 The quantum N-portrait

A microscopic theory of a black hole was developed in a series of works [14–17], with subsequent papers expanding on this notion. Here we briefly review this concept, largely relying on [14]. The key idea is to view a black hole as a multi-graviton state defined on top of a Minkowski vacuum as a ground state. In this picture, a black hole is regarded as a leaky bound state of a Bose-Einstein condensate (BEC) of a large number $N \gg 1$ of weakly interacting soft gravitons. The wavelength λ of these gravitons is set by the scale of the classical geometry, that is by the Schwarzschild radius $R_{\rm S}$. We can estimate the typical energy of each such constituent of the black hole as [14]

$$E_{\rm gr} \sim \frac{\hbar}{\lambda} \sim \frac{\hbar}{R_{\rm S}}. \tag{1.8}$$

With the total mass of the black hole approximately given by the sum of the energies of its individual quanta as [14]

$$M \sim N E_{\rm gr}, \tag{1.9}$$

we can estimate the number of its constituents as

$$N \sim \frac{M}{E_{\rm gr}} \sim \frac{M R_{\rm S}}{\hbar} \sim \frac{R_{\rm S}^2}{\hbar G_{\rm N}}. \tag{1.10}$$

Equivalently, we can express N in Eq. (1.10) in a more intuitive form of [14]

$$N \sim \frac{M^2}{M_{\rm P}^2} \sim \frac{R_{\rm S}^2}{L_{\rm P}^2}. \tag{1.11}$$

The gravitons in the black hole bound-state interact with a dimensionless quantum self-coupling strength of [14]

$$\alpha_{\rm gr} \sim \frac{\hbar G_{\rm N}}{\lambda^2} \sim \frac{L_{\rm P}^2}{\lambda^2} \sim \frac{1}{N}. \tag{1.12}$$

To escape, a quantum needs to attain an energy that exceeds the collective binding energy of the $\sim N$ gravitons of the condensate. This is given by [14]

$$E_{\rm esc} \sim \alpha_{\rm gr} N \frac{\hbar}{\lambda} \sim \frac{\hbar}{\sqrt{N} L_{\rm P}}. \tag{1.13}$$

The leading order contribution to this process is the $2 \to 2$ scattering [14,15]. The Feynman diagram of this process involves two 3-point interaction vertices. Therefore, the scattering amplitude of this process scales as $\alpha_{\rm gr}$. Consequently, the decay rate scales as $\alpha_{\rm gr}^2$. In a state of N quanta, the rate is enhanced by the combinatorial factor $\binom{N}{2} \sim N^2$ due to the choice of 2 out of the N constituent gravitons. With the typical energy of the process $E_{\rm esc}$, the decay rate reads

$$\Gamma \sim \alpha_{\rm gr}^2 N^2 E_{\rm esc} \sim \frac{\hbar}{\sqrt{N} L_{\rm P}} \tag{1.14}$$

to the leading order in N.

The characteristic timescale corresponding to this rate is given by [14]

$$\Delta t \sim \hbar \Gamma^{-1}, \tag{1.15}$$

during which the black hole emits a graviton of energy $E_{\rm gr}$. The corresponding mass decrease of the condensate is then

$$\Delta M = -E_{\rm gr} = -\frac{\hbar}{\lambda}. \tag{1.16}$$

We can then estimate the emission rate of the black hole as [14]

$$\frac{{\rm d}M}{{\rm d}t} \sim -\frac{\hbar}{\lambda}\frac{\Gamma}{\hbar} \sim -\frac{\hbar}{N L_{\rm P}^2}. \tag{1.17}$$

Using Eq. (1.11), this can be re-cast in an informative form in terms of the occupation number N as [14]

$$\frac{{\rm d}N}{{\rm d}t} \sim -\frac{1}{\sqrt{N} L_{\rm P}}. \tag{1.18}$$

Consistently, the half-life time of the black hole is then given by

$$\tau \sim N^{3/2} L_{\rm P}. \tag{1.19}$$

Restoring the usual units by employing Eq. (1.11) in Eq. (1.19), we recover the well-known Page's time for a black hole [18, 19]

$$\tau \sim t_{\rm min} \sim \frac{G_{\rm N}^2 M^3}{\hbar} \sim \frac{R_{\rm S}^3}{\hbar G_{\rm N}}, \tag{1.20}$$

which is equal to the minimal timescale necessary for the onset of information retrieval from the black hole.

Defining the Hawking temperature as [14]

$$T \sim \frac{\hbar}{\sqrt{N} L_{\rm P}} \tag{1.21}$$

and restoring the usual units we consistently retrieve Eq. (1.6).

We thus obtain a dictionary between the framework of the quantum N-portrait and the usual cosmological description of black holes, where all of the corresponding properties of a black hole can be characterized by a single universal quantum parameter, the occupation number N [14]:

- Occupation number N
- Graviton wavelength $\lambda \sim \sqrt{N} L_{\rm P}$
- Coupling strength $\alpha_{\rm gr} \sim 1/N$
- Mass $M \sim \sqrt{N} M_{\rm P}$
- Schwarzschild radius $R_{\rm S} \sim \sqrt{N} L_{\rm P}$
- Entropy $S \sim N$
- Hawking temperature $T \sim \hbar/(\sqrt{N} L_{\rm P})$
- Half-life time $\tau \sim N^{3/2} L_{\rm P}$.

1.5 Entropy saturation

The properties reviewed in the previous sections are usually attributed as unique to black holes. Here we list them again for convenience: First, they possess an entropy that is given by the area-law, the Bekenstein-Hawking entropy [8, 9]

$$S \sim \frac{Area}{G_{\rm N}}, \tag{1.22}$$

where $Area$ is the area of the black hole event horizon and $G_{\rm N}$ is Newton's gravitational constant. Second, semiclassically, black holes have a strict information horizon. Third, in the semiclassical limit black holes evaporate at a thermal decay rate with a temperature [10]

$$T \sim \frac{1}{R}, \tag{1.23}$$

where R is the radius of the black hole. Fourth, there exists a minimal timescale for the onset of information retrieval, the aforementioned Page's time [19] for a black hole, which

is expressed as

$$t_{\min} \sim \frac{Volume}{G_{\rm N}} \sim SR, \tag{1.24}$$

where $Volume$ is the volume of the black hole.

However, black holes are not special in this regard. In fact, there exist objects in other non-gravitational theories that exhibit the above features [20–22]. These objects are called *saturons*. These are n-particle composite classical objects with maximal entropy. For further related work see [1, 23–27]. For a generic quantum field theory in d dimensions the bound on the entropy for an object of size R is given by [22]

$$S_{\max} = \frac{1}{\alpha} = \frac{Area}{G_{\rm Gold}}, \tag{1.25}$$

where α is the effective running coupling of the theory evaluated at the momentum transfer scale $1/R$, $Area \sim R^{d-2}$ is the area of the sphere in which the object is contained, and $G_{\rm Gold}$ is the coupling of the Goldstone field of a spontaneously broken symmetry. Note that, as a bonus, we recover the Bekenstein bound on entropy [28]

$$S = 2\pi M R_{\rm S}. \tag{1.26}$$

We remark, however, that the Bekenstein bound carries no information regarding the coupling of the system and thus cannot be seen as equally fundamental as the bounds in Eq. (1.25).

The underlying reason for the maximal entropy is the non-perturbative saturation of unitarity by $2 \to n$ particle scattering amplitudes at the point of optimal truncation [22]. Below we briefly review this argument, largely relying on [22]. At large n, the $2 \to n$ cross-section is given by

$$\sigma_{2\to n} = c_n n! \alpha^n, \tag{1.27}$$

where the factor c_n is polynomial in n and is therefore not relevant for such scattering processes. We can thus set c_n to one, with the corresponding error scaling as $\sim \frac{\ln(n)}{n}$. Expanding the above cross-section $\sigma_{2\to n}$ in series of α, we must stop when it reaches a minimum in n. This occurs for $n = \alpha^{-1}$, or, in other words, when the collective coupling

$$\lambda_{\rm c} = \alpha n \tag{1.28}$$

is equal to one [22]. Using Stirling's approximation

$$\ln(n!) = n\ln(n) - n + \mathcal{O}\left[\ln(n)\right], \tag{1.29}$$

we obtain for the cross-section:

$$\sigma_{2\to n} = {\rm e}^{-n} = {\rm e}^{-1/\alpha}. \tag{1.30}$$

Non-perturbative arguments also lead to the same conclusion for $n \gg \alpha^{-1}$ [22]. To obtain the total cross-section we sum the individual $2 \to n$ cross-sections over the $n_{\rm st}$-many

micro-states that correspond to the same classical macro-state that is the product of this scattering,

$$\sigma = \sum_{\text{micr. st.}}^{n_{\text{st}}} \sigma_{2\to n}. \tag{1.31}$$

For large n this sum simplifies to multiplying $\sigma_{2\to n}$ by the micro-state degeneracy factor $n_{\text{st}} = \mathrm{e}^S$, where S is the entropy [22]. Using Eq. (1.30) we then obtain

$$\sigma = \mathrm{e}^{-\frac{1}{\alpha}+S}. \tag{1.32}$$

Therefore, when the entropy S saturates the bound in Eq. (1.25), the cross-section σ in Eq. (1.32) saturates the unitarity bound.

1.6 Enhanced memory capacity

The key property that allows a system to exhibit the microstate entropy as given by Eq. (1.25), is that it is able assume a large number of microstates n_{st} that correspond to a given macrostate. For this to hold, these microstates need to be degenerate in energy and therefore fit within a narrow energy gap [29]. Consequently, they all contribute into the microstate entropy $S = \ln(n_{\text{st}})$. Thus, such a system is able to store large amounts of information. That is, the system possesses an *enhanced memory capacity* [29,30]. See [31–34] for further studies. The brief overview below relies largely on the review [35].

Suppose that we would like to establish such a system, which can store a large amount of information in terms of the occupation numbers of its modes $\hat{a}_k$ for $k = 1, \ldots, K$. We refer to these as *memory modes* [35]. We can assume the modes to be bosonic and the corresponding creation and annihilation operators obeying the standard commutation relations

$$\left[\hat{a}_j, \hat{a}_k^\dagger\right] = \delta_{jk}, \quad [\hat{a}_j, \hat{a}_k] = 0, \quad \left[\hat{a}_j^\dagger, \hat{a}_k^\dagger\right] = 0. \tag{1.33}$$

The various sequences of the occupation numbers of the respective modes $|n_1, \ldots, n_K\rangle$ correspond to the states of the system. We refer to each such distinct state as a *memory pattern* [35].

Given the energy cost ε of occupying one such memory mode, we can express the Hamiltonian of the system as

$$\hat{H} = \varepsilon \sum_{k=1}^{K} \hat{n}_k. \tag{1.34}$$

However, as the energy gap ε is nonzero, storing large amounts of information is very costly. We can solve this by employing the effect of *assisted gaplessness* [34]. Specifically, we introduce an additional bosonic *master mode* $\hat{a}$ with the corresponding occupation number operator denoted by $\hat{n}_a$ [35]. This mode interacts attractively with the memory modes, lowering their effective energy gaps ε_{eff}. The master mode $\hat{a}$ can also exchange occupation number with an external mode $\hat{b}$, with the strength of the corresponding coupling

parametrized by C_b. The Hamiltonian now reads

$$\hat{H} = \underbrace{\left(1 - \frac{\hat{n}_a}{N}\right)\varepsilon}_{=\varepsilon_{\text{eff}}} \sum_{k=1}^{K} \hat{n}_k + C_b \left(\hat{a}^\dagger \hat{b} + \text{H.c.}\right). \tag{1.35}$$

Note that whenever the master mode reaches a certain critical occupation number $\langle \hat{n}_a(t) \rangle = N$, the energy gaps of the memory modes $\hat{a}_k$ become gapless. Consequently, the energy cost to excite them vanishes. The system is now able to accommodate large amounts of information in terms of the occupation numbers of the memory modes.

If we evolve the system from the initial state

$$|\text{in}\rangle = |n_a, n_b, n_1, \ldots, n_K\rangle = |N, 0, n_1, \ldots, n_K\rangle\,, \tag{1.36}$$

the large amount of quantum information stored in the memory modes will backreact onto the master mode, preventing it to lose occupation number quickly. That is, the system becomes stabilized in the above state of enhanced memory capacity and its evolution is slowed down. We refer to this as the *memory burden* effect [30, 33]. In Sec. 3.2 we discuss this further and review how memory burden can be avoided.

1.7 Scrambling

Consider a quantum system of K information-storing degrees of freedom, such as that in Eq. (1.35). To illustrate our point, we include an additional term of the form $(\hat{a}_j^\dagger \hat{a}_k + \text{H.c.})$ in the corresponding Hamiltonian to allow the various information carrying memory modes $\hat{a}_j$, $\hat{a}_k$ with $j, k = 1, \ldots, K$ to exchange occupation number. We parametrize the strength of the corresponding coupling by C_m. Due to the unitary time-evolution of the system, an initial pure state of the system remains pure throughout. Nevertheless, with time, the initial state becomes increasingly and sufficiently entangled with all of the other states in the state space by some measure. We refer to this phenomenon as the system *scrambling* [36–38] the information initially contained only in its original state.

Some of the first various measures of scrambling mentioned in the literature include: Haar-scrambled [36,37] and Page-scrambled [37,39]. However, to understand the process of scrambling at a quantum level, a microscopic picture is necessary. Based on the quantum N-portait, such a framework was suggested in [14, 16, 40–42] and developed in related works. In relation to microscopic models of black holes, the corresponding scrambling measures and the respective timescales discussed in these papers are those of one-particle entanglement [41] and maximal entanglement [42]. Building on the findings above, in chapter 3, which is based on [2], we consider the early-time aspects of scrambling within such a microscopic model of a black hole.

1.8 Thermalization

Thermalization of physical systems has long been a prominent field of research. There exist multiple definitions of thermalization, depending on the specific system and the context of the question being investigated. The concept of scrambling discussed above can also be viewed as a form of apparent thermalization in isolated quantum systems. Let us stress again that an initial pure state of a system evolved unitarily in time remains pure. However, under certain conditions, expectation values of observables may time-evolve to approach their statistical ensemble averages. Thus, finding microscopic mechanisms by which isolated quantum many-body systems thermalize has long been a subject of interest [43]. That is, for such a system prepared in a pure initial state far from equilibrium, what is the underlying reason for few-body observables within that system, under unitary time evolution, to equilibrate to their typical expectation values predicted by an appropriate statistical ensemble? In other words, the goal is to unveil the mechanisms allowing to describe isolated quantum systems by equilibrium statistical mechanics.

The *Eigenstate Thermalization Hypothesis* (ETH) [44, 45] introduced a prominent microscopic mechanism explaining this thermalization. Since then, it has been expanded upon in [46–48] among many other works (for reviews see e.g. [49–53]). Subsequently, a large variety of different thermalization mechanisms were developed: [50, 54–59] to name only a few. We review the ETH in detail in chapter 4, as well as the relevant aspects of the other thermalization mechanisms.

1.9 Outline

The present work is structured as follows. In chapter 2, which is based on [1], we consider a renormalizable $SU(N)$ invariant field theory from [22]. The spectrum of this theory contains a tower of vacuum bubbles that are bound states of $SU(N)$ Goldstones. We show that, despite the absence of gravity, saturated vacuum bubbles exhibit properties that are in one-to-one correspondence to those of black holes. This correspondence is due to the fact that a vacuum bubble that stores quantum information breaks the Poincaré symmetry spontaneously. This results in the existence of a Poincaré Goldstone. We address the implications of our findings for black hole physics.

Chapter 3 is based on [2]. Here we consider the early time-evolution of a prototype system of enhanced memory capacity introduced to model the information processing characteristics of a black hole. Based on this specific example, we suggest a series of conjectures regarding the early stages of the process of information scrambling within generic quantum systems. We denote this novel regime as prescrambling and quantify it. We employ the most nonrestrictive definition of scrambling, namely that the state of the system is sufficiently distributed over the entire Hilbert space with respect to some measure. Our findings are in agreement with the fast scrambling conjecture [36–38]. We also address the relevance of our results to the information-scrambling physics of black holes.

In chapter 4 we consider the long-time behavior of few-body observables in the afore-

mentioned quantum prototype model with enhanced memory capacity. We find indications that the expectation values of these observables equilibrate to their respective microcanonical ensemble averages in the thermodynamic limit (TDL), and thus thermalize in this sense. We demonstrate that the thermalization mechanisms established in the literature cannot explain thermalization in this system for the chosen observables. Our findings therefore lead us to suggest a new thermalization mechanism for isolated quantum systems. The novelty is the occurrence of thermalization despite unignorable correlations between the fluctuations of the eigenstate expectation values $\langle\alpha|\,\hat{A}\,|\alpha\rangle$ of a few-body observable $\hat{A}$ in the eigenstate basis $\{|\alpha\rangle\}$ and the fluctuations of the squared magnitudes of the coefficients $|C_\alpha|^2 = |\,\langle\alpha|\mathrm{in}\rangle\,|^2$ for a non-equilibrium initial state $|\mathrm{in}\rangle$ of the system. We discuss the implications of such correlations for thermalization within isolated quantum systems as well as the application of our results to black hole physics.

In chapter 5 we summarize the results of the dissertation and provide general conclusions and an outlook for future research.

For transparency, let us note that some of the results obtained in joint projects together with collaborators, both published and those in preparation, described in or related to the present dissertation, have been and will be reported in their respective theses and dissertations. Specifically, these include the following: Extensions of the code used for [2,3] were developed in collaboration with Houssem Amami and the respective results appeared in the corresponding Master's thesis based on these findings. Furthermore, results from [1] will also be reported independently in the dissertation by Juan Sebastián Valbuena-Bermúdez (in preparation).

Chapter 2

How Special are Black Holes?

This chapter is based on the work [1]. In the corresponding paper, within a renormalizable $SU(N)$-symmetric theory, we construct bubbles representing bound states of $SU(N)$ Goldstone bosons. These bubbles are able to attain the maximal entropy permitted by unitarity within this theory. Such objects that saturate the corresponding bounds on entropy within the respective theories are called "saturons". As was recently proposed, they possess the properties that are often considered to be uniquely exhibited by black holes, due to the seemingly special time evolution and information processing characteristics of the latter. Despite the absence of gravity in the considered $SU(N)$ invariant theory, a saturated bubble is very similar to a black hole: Its entropy scales as its area; semiclassically, the bubble evaporates thermally with a temperature proportional to its inverse radius and exhibits a strict information horizon; and the minimum time for the onset of information recovery is equal to the Page time. The underlying connection within this black hole–saturon correspondence is due to the transtheoretic notion of a Goldstone boson of spontaneously broken Poincaré symmetry. This correspondence has significant implications for black hole physics, both fundamental and observational.

2.1 Introduction

Due to their information processing characteristics, black holes are often considered to be special. Recently, it has been suggested [22, 24] that these properties are generic for a class of objects called *saturons*. For a given theory, these objects saturate the microstate entropy bound imposed by unitarity within that theory. These findings are based on the works [20, 21], which constructed solitons and instantons that exhibit a high degeneracy of microstates and, correspondingly, a large microstate entropy.

The corresponding entropy bound has two equivalent formulations [22]. For an object of size R in d space-time dimensions, the first form of the bound on entropy is given by

$$S \leq \frac{Area}{G_{\text{Gold}}}, \tag{2.1}$$

where $Area \sim R^{d-2}$ denotes the area of the sphere the object is contained within, and $G_{\rm Gold}$ is the Goldstone field coupling of the spontaneously broken Poincaré symmetry. Any macroscopic object that stores quantum information inevitably breaks the Poincaré symmetry spontaneously. The above bound holds true in arbitrary space-time dimensions, including $d = 2$; see [25] for a specific example.

The bound in Eq. (2.1) has an equivalent form of

$$S \leq \frac{1}{\alpha} \tag{2.2}$$

in terms of an effective running coupling α of the theory, that is evaluated at the momentum transfer scale of $1/R$. Note that the equivalence of the above two formulations of the bound can be seen from the expression for the effective dimensionless Goldstone coupling

$$\alpha_{\rm Gold} \equiv \frac{G_{\rm Gold}}{Area}, \tag{2.3}$$

evaluated at the momentum transfer scale $1/R$. The above two bounds are saturated simultaneously [21]. We can thus write down the combined form of the entropy bound imposed by unitarity as

$$S_{\rm max} = \frac{1}{\alpha} = \frac{Area}{G_{\rm Gold}}. \tag{2.4}$$

Denoting the canonically normalized Goldstone decay constant as f, we can express the Goldstone coupling $G_{\rm Gold}$ of a Poincaré Goldstone as

$$G_{\rm Gold} \equiv f^{-2}. \tag{2.5}$$

For the entirety of the chapter we work in $d = 4$ space-time dimensions. Correspondingly, f has the dimensionality of mass. For any field-theoretic object that is a bound state of N quanta of wavelengths R and is self-sustained, Eq. (2.5) takes the form of

$$G_{\rm Gold} = f^{-2} = \frac{R^2}{N}. \tag{2.6}$$

Saturons, the objects that saturate the entropy bounds in Eqs. (2.1) and (2.2), possess a set of common properties, which are identical to those of black holes [22]

(i) Their entropy obeys the area-law, see Eq. (2.4),

(ii) Semiclassically, i.e. up to $1/S$ corrections, they decay with a thermal rate with a temperature

$$T \sim 1/R, \tag{2.7}$$

(iii) Semiclassically, they possess a strict information horizon,

(iv) The minimal timescale necessary for the onset of information recovery is bounded from below by

$$t_{\rm min} = \frac{Volume}{G_{\rm Gold}} = \frac{R}{\alpha} = S_{\rm max} R, \tag{2.8}$$

with $Volume \sim R^{d-1}$ equal to the volume of the sphere within which the object is contained.

For a black hole, the Goldstone boson of the spontaneously broken Poincaré symmetry comes from the graviton. The latter has the coupling strength $G_{\rm N}$. That is, the mapping

$$G_{\rm Gold} \to G_{\rm N} \tag{2.9}$$

demonstrates the complete correspondence of the above properties to those of a black hole. Under the mapping in Eq. (2.9), from the maximal entropy in Eq. (2.4) we recover the familiar expression of the Bekenstein-Hawking entropy [8, 9]

$$S_{\rm BH} \sim \frac{Area}{G_{\rm N}} \tag{2.10}$$

for a black hole of radius R. Equivalently, we can express this entropy in terms of the quantum gravitational coupling $\alpha_{\rm gr} = G_{\rm N}/Area$ in d space-time dimensions evaluated at the momentum transfer scale of $1/R$ as [14, 16, 22, 60]

$$S_{\rm BH} \sim \frac{1}{\alpha_{\rm gr}}. \tag{2.11}$$

Note that with the mapping in Eq. (2.9), from the timescale in Eq. (2.8) we obtain the Page's time [19] for a black hole; the minimal timescale of the start of information retrieval.

The work of [22] suggests that the above characteristics are exhibited by saturons in arbitrary theories and are thus not unique to black holes or gravity. In addition to [1], various other works provided examples of this correspondence, including solutions in Lorentzian and Euclidean spaces, such as solitons, instantons, and other self-sustained bound states [20–22], bound states in the Gross-Neveu model [25, 61, 62] (see [63, 64] for reviews), the "color-glass condensate" (CGC) exhibiting the properties of a saturon in ordinary QCD [23, 65], as well as the proposal of the existence of saturon dark matter [27].

Note that the saturon correspondence is a correspondence between black holes and bound states within the frameworks of other various theories, instead of between the respective theories themselves. The underlying reason for this trans-theoretic correspondence is the saturation of the entropy bounds given by Eqs. (2.1) and (2.2), which are imposed by unitarity of the respective theories.

As mentioned previously, the black hole-saturon correspondence allows us to improve our understanding of black hole physics. As established by the examples above, saturons exist in renormalizable and calculable theories, while still exhibiting all of the essential characteristics of black holes. Researching saturons in various theories thus allows us, on the one hand, to understand at a more fundamental level the underlying reasons which give rise to the properties of black holes, while on the other hand, to propose new effects and phenomena for black hole physics. The memory burden effect [30, 35], by which the quantum information can stabilize the system that carries this information, is one of such suggested phenomena.

In this chapter, following [1], we demonstrate a further example of the above black hole-saturon correspondence. We study saturons within a renormalizable theory of a scalar field in $d = 4$ space-time dimensions from [22]. The theory possesses a global $SU(N)$ symmetry and multiple degenerate vacuum states corresponding to different patterns of spontaneous symmetry breaking (SSB). As the theory is renormalizable, we can study it at arbitrarily weak coupling and large N. The spectrum of the theory contains solitonic vacuum bubbles which separate the vacua corresponding to distinct SSB patterns.

The spectrum includes an infinite set of bubbles that are stable due to the memory burden effect. These bubbles are bound states containing a large number of Goldstone bosons, which are a result of the SSB. We denote the total occupation number of the Goldstone quanta within a vacuum bubble by N_G. The Goldstones can exist only within the bubble as the symmetry is unbroken in the asymptotic vacuum outside of the bubble and the Goldstone quanta therefore cannot propagate there. If a bubble decays, it releases massive quanta that carry the conserved $SU(N)$ charge into the exterior vacuum. Prior to the bubble's decay, this charge is stored in terms of the occupation numbers of the Goldstone modes in the interior of the bubble. Thus, semiclassically, the bubble is completely stable due to the resulting energy barrier.

We can label the levels of the spectrum by N_G, with each level being exponentially degenerate. Therefore, the vacuum bubbles can have a high microstate entropy. Specifically, we show that the bubbles with a Goldstone occupation number $N_G \sim N$ are saturons, with the entropy of such bound states saturating the bounds in Eqs. (2.1) and (2.2). These vacuum bubbles possess the maximal entropy given by Eq. (2.4), which is imposed by unitarity. In other words, we provide a further concrete example of the black hole-saturon correspondence of [22], with the saturated bound states of the theory possessing all of the aforementioned relevant characteristics of a black hole.

Furthermore, our findings provide additional evidence for the proposed black hole N-portrait [14]. There, a black hole is portrayed as a saturated multi-graviton bound state of N weakly interacting soft gravitons. Similarly, in a direct correspondence to a black hole, a saturated vacuum bubble represents a bound state of N Goldstone bosons. In this chapter we reproduce the black hole properties, demonstrated in the framework of the quantum N-portrait, for the Goldstone bound states within the $SU(N)$ symmetric renormalizable and calculable theory. The $1/N$ corrections to the self-similar Hawking evaporation of black holes are one of these properties.

Let us note that [25] provides yet another example of saturated bound states within the spectrum of the calculable Gross-Neveu theory in $d = 2$ dimensions. This provides further supporting evidence for the correspondence between black holes and generic saturons. The spectrum of the Gross-Neveu theory contains a set of fermion-bound states with increasing mass and degeneracy. Within this theory, the bound state of maximal degeneracy is a saturon [25] and possesses all of the relevant characteristics of saturons of higher-dimensional theories, including black holes and, in particular, the saturons in the four-dimensional theory discussed in this chapter. This demonstrates the ubiquity of large-N physics at the point of unitarity saturation. It is this universality due to which the relevant properties of the saturons both in the Gross-Neveu model and in the model of the present chapter

are identical to each other and to the corresponding characteristics of black holes. This further justifies the suggestion that the underlying cause for the properties of black holes is not rooted in gravity and is instead due to the universal physics of saturation [22].

2.2 Saturon model

2.2.1 The model

We consider the theory of [1] in $d = 4$ space-time dimensions, originally constructed in [22]. This is a theory of a scalar field ϕ in the adjoint representation of $SU(N)$, with $N \geq 3$. Thus, the field ϕ can be represented as an $N \times N$ traceless Hermitian matrix ϕ^{β}_{α} with $\alpha, \beta = 1, \ldots, N$. The Lagrangian density of the theory reads

$$\begin{aligned} \mathcal{L} &= \frac{1}{2}\mathrm{tr}\left[(\partial_\mu \phi)\,(\partial^\mu \phi)\right] - V\left[\phi\right], \\ \text{with } V\left[\phi\right] &= \frac{\alpha}{2}\mathrm{tr}\left[\left(f\phi - \phi^2 + \frac{I}{N}\mathrm{tr}\left[\phi^2\right]\right)^2\right], \end{aligned} \tag{2.12}$$

where I is the unit $N \times N$ matrix, α is a dimensionless coupling, and f is the scale of symmetry breaking.

We note again that the above theory is renormalizable. We perform our analysis in the regime where the fundamental quantum coupling α is weak. Nevertheless, even for an arbitrarily weak coupling α, unitarity of the theory imposes the entirely unperturbative upper bound on the strength of the coupling, which is given by

$$\alpha \lesssim \frac{1}{N}. \tag{2.13}$$

The underlying physical reason is that the 't Hooft coupling [66]

$$\lambda_{\mathrm{t}} = \alpha N \tag{2.14}$$

is the parameter that controls unitarity within the theory, both perturbatively as well as nonperturbatively.

Unitarity is saturated when the 't Hooft coupling becomes order one,

$$\lambda_{\mathrm{t}} \sim 1, \tag{2.15}$$

irrespective of how weak is the coupling α. The breakdown of the loop expansion and the saturation of unitarity by scattering amplitudes both indicate this, as discussed in detail in [22]. The constraint in Eq. (2.13) is a crucial requirement for the upper bound on entropy in Eq. (2.4). In this chapter we demonstrate the saturation of this bound on the specific example of the $SU(N)$ theory in Eq. (2.12).

We adopt the regime of weak coupling α and large N. In the limit when the 't Hooft coupling in Eq. (2.14) approaches the unitarity bound in Eq. (2.13) from below, certain

solitons saturate the entropy bounds in Eqs. (2.1) and (2.2) and assume the relevant properties of black holes.

To find these solitons we first consider the vacuum equations of the theory, which are given by

$$f\phi_\alpha^\beta - (\phi^2)_\alpha^\beta + \frac{\delta_\alpha^\beta}{N}\mathrm{tr}\left[\phi^2\right] = 0. \tag{2.16}$$

These possess a set of solutions that correspond to vacua with different unbroken symmetries. Specifically, these are the unbroken $SU(N)$ symmetry vacuum where $\phi = 0$, and the vacua with the SSB patterns

$$SU(N) \to SU(N-K) \times SU(K) \times U(1), \tag{2.17}$$

with $0 < K < N$. All of the above vacua are degenerate in energy by construction. For the entirety of the chapter we restrict our analysis to two specific vacua, namely the unbroken vacuum $\phi = 0$ and the one with $K = 1$. In the latter vacuum, only the component

$$\phi_\alpha^\beta = \frac{\phi(x)}{\sqrt{N(N-1)}}\mathrm{diag}\left((N-1), -1, \ldots, -1\right) \tag{2.18}$$

has a nonzero expectation value

$$\langle\phi\rangle = f\frac{\sqrt{N(N-1)}}{(N-2)} \simeq f. \tag{2.19}$$

As we perform our analysis at large N, where appropriate, we approximate the expressions by their leading order values in the $N \to \infty$ limit. The symmetry group of this vacuum is $SU(N-1) \times U(1)_Y$, with the generator of $U(1)_Y$ given by

$$\hat{Y} = \frac{1}{\sqrt{2N(N-1)}}\mathrm{diag}\left((N-1), -1, \ldots, -1\right). \tag{2.20}$$

In the vacuum which corresponds to the unbroken $SU(N)$ symmetry, the theory possesses a nonzero mass gap,

$$m = \sqrt{\alpha}f. \tag{2.21}$$

Therefore, no massless excitations can exist in this vacuum. Conversely, the broken symmetry vacuum for $K = 1$ possesses

$$N_{\mathrm{Gold}} = 2(N-1) \tag{2.22}$$

distinct species of massless Goldstone bosons, which we equivalently refer to as flavors. We denote these by $\theta^a(x_\mu)$ with $a = 1, \ldots, N_{\mathrm{Gold}}$. These Goldstones correspond to the spontaneously broken generators T^a. We can express these broken generators in terms of the off-diagonal Pauli matrices as

$$(T^a)_\alpha^\beta = \frac{1}{2}(\delta_\alpha^1\delta_{k+1}^\beta + \delta_\alpha^{k+1}\delta_1^\beta) \quad \text{for } a = 2k-1, \tag{2.23}$$

and

$$(T^a)^\beta_\alpha = \frac{-i}{2}(\delta^1_\alpha \delta^\beta_{k+1} - \delta^{k+1}_\alpha \delta^\beta_1) \quad \text{for } a = 2k, \tag{2.24}$$

with $k = 1, \ldots, N-1$.

The combinations $T^\pm_k = T^{2k-1} \pm i T^{2k}$ of these broken generators form $(N-1)$-dimensional fundamental and antifundamental representations under the unbroken $SU(N-1)$ symmetry group. The charges $Y_\pm = \pm \dfrac{N}{\sqrt{2N(N-1)}}$ of the generators $T^\pm_k$ under the $U(1)_Y$ group obey the relation

$$[\hat{Y}, T^\pm_k] = Y_\pm T^\pm_k. \tag{2.25}$$

The combinations $\theta^\pm_k \equiv \theta^{2k-1} \pm i\theta^{2k}$ of the Goldstones transform under the same representations as the combinations of the broken generators $T^\pm_k$. Consistently with the above, $\sum_a \theta_a T^a = \frac{1}{2}\sum_k \theta^\mp_k T^\pm_k$ holds.

Expressing the field as

$$\phi^\beta_\alpha = (U^\dagger \langle\phi\rangle U)^\beta_\alpha \tag{2.26}$$

where

$$U = \exp[-i\theta^a T^a], \tag{2.27}$$

and substituting this into the action of the theory we can obtain the effective low energy theory of the Goldstones. Up to the second order in θ^a, the corresponding effective Lagrangian density of the Goldstone modes reads

$$\mathcal{L}_{\text{eff}} = \frac{N^2}{4(N-2)^2} f^2 \sum_a (\partial_\mu \theta^a)(\partial^\mu \theta^a) \simeq \frac{1}{4} f^2 \sum_k \left(\partial_\mu \theta^+_k\right)\left(\partial^\mu \theta^-_k\right). \tag{2.28}$$

The theory discussed in this chapter admits solutions in the form of bubbles. The wall of such a bubble separates the broken symmetry vacuum within it and the unbroken symmetry vacuum in its exterior. Therefore, the interior of the bubble can accommodate for a state with a high microstate entropy because of the gapless Goldstone excitations. We construct such vacuum bubble solutions below.

2.2.2 Vacuum bubble

The two vacua $SU(N)$ and $SU(N-1) \times U(1)_Y$ are degenerate in energy. Therefore, there exist solutions in the form of domain walls that separate the two. The component in Eq. (2.18) of the adjoint field for a planar infinite, and therefore static, wall reads

$$\phi(x) = \frac{f}{2}\left[1 \pm \tanh\left(\frac{mx}{2}\right)\right]. \tag{2.29}$$

Here x is the coordinate perpendicular to the wall. The corresponding thickness of the wall is parametrized by

$$\delta_{\text{w}} \sim m^{-1}. \tag{2.30}$$

From such a domain wall solution we can construct a bubble of radius $R \gg \delta_{\mathrm{w}}$. The vacuum of the interior of the bubble corresponds to the broken $SU(N-1) \times U(1)_Y$ symmetry. The vacuum of the bubble exterior corresponds to the unbroken $SU(N)$ symmetry group. For a finite-size vacuum bubble no exact analytic solution is known. Furthermore, the tension of the bubble wall exerts a force directed radially inwards to the center of the bubble. Thus, a bubble of a finite radius R will collapse, unless the force caused by the tension of the bubble walls is balanced out.

In the thin-wall regime $R \gg \delta_{\mathrm{w}}$, the profile of the field ϕ corresponding to a bubble of radius R can be approximated by

$$\phi(r) = \frac{f}{2}\left[1 + \tanh\left(\frac{m(R-r)}{2}\right)\right] \tag{2.31}$$

for a slow-moving bubble wall. Here we denote the radial coordinate by r.

As mentioned previously, because of the spontaneous symmetry breaking with the breaking pattern given by $SU(N) \to SU(N-1) \times U(1)$, there exist gapless Goldstones inside the vacuum bubble. The number of the Goldstone bosons is given by $N_{\mathrm{Gold}} = 2(N-1)$. In the vacuum outside of the bubble, $r \gg R$, the symmetry is unbroken. In this asymptotic vacuum the theory exhibits a nonzero mass gap given in Eq. (2.21). Therefore, no Goldstone modes can propagate out into this region and are thus trapped in the interior of the bubble. As the Goldstones within the bubble are gapless, the bubble possesses a high capacity to store information in terms of the occupation numbers of the Goldstone modes. The information stored in the excitations of the Goldstones prevents the bubble from collapsing and stabilizes it via the memory burden effect [22].

2.3 Bubble stabilization by memory burden

As discussed above, the memory burden effect can considerably alter the time-evolution of the bubble, as it can counteract the collapse of the bubble and stabilize it. We investigate this phenomenon below. Due to the gaplessness of the Goldstones, the energy cost to store quantum information in terms of the occupation numbers of the Goldstone modes is small. Specifically, the information can be encoded in sequences of the occupation numbers n^a of the different species of Goldstone modes with corresponding $SU(N)$ quantum numbers. Each such distinct sequence represents a memory pattern.

In the case that the vacuum bubble decays, the information contained in the excitations of the Goldstone modes within it needs to be stored in terms of the occupation numbers of the outside quanta. However, gapless excitations cannot exist in the exterior $SU(N)$-symmetric vacuum as the theory has a nonzero mass gap there. Therefore, it costs more energy to store information as a memory pattern in the unbroken $SU(N)$ vacuum outside of the bubble than in the broken $SU(N-1) \times U(1)$ interior vacuum. Furthermore, as we demonstrate below, the energy cost to store an information pattern in the exterior vacuum can exceed the energy of the entire vacuum bubble.

As mentioned previously, via the memory burden effect, the total occupation number of the Goldstone modes prevents the bubble from decaying. Specifically, the information stored in these modes backreacts onto the bubble wall and counteracts the collapse. It is important to emphasize that only the total occupation number of the Goldstone modes quantifies the memory burden effect. The specific distribution of the occupation numbers among the distinct Goldstone species is irrelevant. That is, as far as the stability of the bubble is concerned, the regime in which many modes are excited to low levels is equivalent to that in which one single mode is highly excited. A highly excited Goldstone mode can be approximated by a classical field configuration. In this section we study both of the above cases.

We consider a field configuration given by

$$\phi_\alpha^\beta = (U^\dagger \Phi U)_\alpha^\beta \tag{2.32}$$

for the model in Eq. (2.12). Here, similarly to Eq. (2.18), Φ_α^β is given by

$$\Phi_\alpha^\beta = \frac{\varphi(t,\vec{x})}{\sqrt{N(N-1)}}\text{diag}\left((N-1),-1,\ldots,-1\right) \tag{2.33}$$

with

$$U = \exp\left[-i\theta^a(t,\vec{x})T^a\right]. \tag{2.34}$$

With the above ansatz, up to the second order in θ^a, the theory in Eq. (2.12) now reads

$$\mathcal{L} = \frac{1}{2}\left(\partial_\mu\varphi\right)\left(\partial^\mu\varphi\right) + \frac{N}{4(N-1)}\varphi^2\left(\partial_\mu\theta^a\right)\left(\partial^\mu\theta^a\right) - \frac{\alpha}{2}\varphi^2\left(\varphi - f\right)^2, \tag{2.35}$$

where the N-dependent factors of α and f,

$$\tilde{\alpha} \equiv \alpha\frac{(N-2)^2}{N(N-1)}, \quad \tilde{f} \equiv f\frac{\sqrt{N(N-1)}}{(N-2)}, \tag{2.36}$$

are absorbed into the respective redefinitions, $\tilde{\alpha} \to \alpha$ and $\tilde{f} \to f$.

The field φ is assumed to take an initial configuration of a spherically symmetric bubble of finite radius R. The bubble is an "island" of the broken $SU(N-1)\times U(1)$ vacuum embedded in the $SU(N)$-symmetric one. In other words, the field profile at $t = 0$ is a configuration $\varphi(0,r)$ which interpolates between a finite nonzero value at $r = 0$ to zero at $r = \infty$. As discussed above, a vacuum bubble is capable of storing a large amount of information in terms of the occupation numbers of the Goldstone modes θ^a. Each sequence of such occupation numbers constitutes a distinct information pattern. However, if none of the Goldstone modes are occupied, the corresponding memory pattern is empty and has no influence on the time-evolution of the vacuum bubble. In this case the bubble collapses, with the bubble wall undergoing a series of oscillations in the radial direction, before the bubble ultimately decays into the asymptotic modes of the unbroken $SU(N)$ vacuum.

Contrarily, a nonempty memory pattern can prevent the bubble from collapsing. We investigate this below. There are two distinct cases, distinguished by the properties of the distribution of the total Goldstone occupation number among the individual Goldstone species. In the first regime the individual occupation numbers are large. We can therefore employ the Bogoliubov approximation and reduce the field operators of the corresponding Goldstone modes to c-numbers. Here, we can treat the macroscopically occupied Goldstones θ^a as classical fields. However, in the second regime, the individual Goldstone modes possess a small occupation number. That is, they are occupied microscopically. Correspondingly, we cannot use the Bogoliubov approximation to replace the operators to c-numbers, but must instead treat the modes within a quantum framework.

Let us emphasize that the memory burden effect can be equally considerable in the second case as in the first. That is, despite the fact that in the quantum regime the occupation numbers of the individual Goldstone modes are small, their collective effect can be substantial. For large N, correspondingly many (see Eq. (2.22)) Goldstone species can be excited. Therefore, an entirely quantum memory burden can prevent even a classical vacuum bubble from collapsing. Below we demonstrate that this occurs when the bubble saturates the entropy bounds in Eqs. (2.1) and (2.2).

2.3.1 Classical regime

Our goal is to find a solution in the form of a localized stationary vacuum bubble, where the Goldstone modes in its interior have a time dependence. We start with the ansatz

$$\varphi = \varphi(r), \quad \theta^a = \delta^{a1}\omega t, \tag{2.37}$$

with ω parametrizing the rotation frequency in the internal space. As is clear from the above expression, only one Goldstone mode participates in this rotation. That is, only a single Goldstone flavor is macroscopically occupied.

As only the Goldstone with the label $a = 1$ is involved with the rotation, all of the Goldstones with labels $a \neq 1$ can be set to zero. The effective Lagrangian density in Eq. (2.35) is then exact to all orders in θ^a and is a full nonlinear classical theory for the ansatz in Eq. (2.37). This holds true as all other components of the Lagrangian density are bilinear or of higher powers. We can consistently set these components to zero without invalidating the ansatz in Eq. (2.37). As a specific example, consider the ansatz in Eq. (2.32) with a generic $SU(2)$ transformation of the subgroup $SU(2)\times SU(N-2)\times U(1) \subset SU(N)$ parametrized by the rotation matrix

$$U = \begin{pmatrix} \cos\left(\frac{\theta^1}{2}\right) \mathrm{e}^{-i\gamma} & -\sin\left(\frac{\theta^1}{2}\right) \mathrm{e}^{i\delta} \\ \sin\left(\frac{\theta^1}{2}\right) \mathrm{e}^{-i\delta} & \cos\left(\frac{\theta^1}{2}\right) \mathrm{e}^{i\gamma} \end{pmatrix}. \tag{2.38}$$

The resulting effective Lagrangian density, under the same rescaling of α and f as above,

reads

$$\begin{aligned}\mathcal{L} =& \frac{1}{2}\left(\partial_\mu\varphi\right)\left(\partial^\mu\varphi\right) + \frac{N}{4(N-1)}\varphi^2\left(\partial_\mu\theta^1\right)\left(\partial^\mu\theta^1\right) \\ &+ \frac{N\sin^2(\theta^1)}{4(N-1)}\varphi^2\left(\partial_\mu(\gamma+\delta)\right)\left(\partial^\mu(\gamma+\delta)\right) - \frac{\alpha}{2}\varphi^2\left(\varphi-f\right)^2,\end{aligned} \tag{2.39}$$

where $\gamma+\delta=0$ is a valid solution.

To find the stationary profile of the bubble we therefore need to consider the only remaining nontrivial equation

$$\mathrm{d}_r^2\varphi + \frac{2}{r}\,\mathrm{d}_r\varphi + \varphi\left(\omega^2 - \alpha(\varphi-f)(2\varphi-f)\right) = 0. \tag{2.40}$$

As previously, we absorb the N-dependent factors of α and f into their corresponding redefinitions, as well as performing the same for the frequency ω,

$$\tilde{\omega} \equiv \omega\sqrt{\frac{N}{2(N-1)}} \to \omega. \tag{2.41}$$

The boundary conditions for a stationary bubble solution are given by

$$\varphi(0) \neq 0, \quad \varphi(\infty) = 0. \tag{2.42}$$

It is important to note that the Goldstone fields of the primary symmetry breaking, with the breaking pattern $SU(N) \to SU(N-1)\times U(1)_Y$, transform nontrivially under the $SU(N-1)\times U(1)_Y$ group. Therefore, the ansatz in Eq. (2.37) leads to a secondary symmetry breaking down to the symmetry group $SU(N-2)\times U(1)_X$. Here, the generator of the $U(1)_X$ symmetry group reads

$$\hat{X} = \frac{1}{\sqrt{N(N-2)}}\mathrm{diag}\left((N-2)/2, (N-2)/2, -1, \ldots, -1\right). \tag{2.43}$$

This secondary symmetry breaking gives rise to an extra set of $2N-3$ Goldstone bosons. However, let us emphasize that some internal Goldstones mix with the Goldstone boson of the broken time-translation symmetry. This is a crucial aspect, but in the large-N limit its effect on the entropy count is negligible.

Below we consider the stationary classical configuration. Regarding Eq. (2.40), we can think of $\varphi(r)$ as the "coordinate" φ of a particle moving in "time" r in the external potential given by

$$V(\varphi) = \frac{1}{2}\varphi^2\left(\omega^2 - \alpha(\varphi-f)^2\right). \tag{2.44}$$

In the parameter subspace where

$$\frac{\omega^2}{\alpha f^2} < 1, \quad \text{or equivalently,} \quad \omega^2 < m^2, \tag{2.45}$$

the potential $V(\varphi)$ in Eq. (2.44) possesses two maxima, which are given by $\varphi_0 = 0$ and $\varphi_{\max} = \frac{f}{4}\left(3+\sqrt{1+\frac{8\omega^2}{\alpha f^2}}\right)$, with a minimum between these two, given by $\varphi_{\min} = \frac{f}{4}\left(3-\sqrt{1+\frac{8\omega^2}{\alpha f^2}}\right)$. The potential vanishes at $\varphi_0 = 0$ and $\varphi_\pm = f \pm \frac{\omega}{\sqrt{\alpha}}$.

We can argue the validity of the stationary bubble solution as follows: The initial position of the particle φ at time $r = 0$ is $\varphi(0)$. The initial velocity of φ is fixed to zero, $\mathrm{d}_r\varphi(r)|_{r=0} = 0$, to control the friction term, which is singular at $r = 0$. To fully specify the initial conditions of the problem it remains to set the initial coordinate $\varphi(0)$. The initial position must satisfy $\varphi_- < \varphi(0) \leq \varphi_{\max}$ for the particle to reach $\varphi_0 = 0$ in the asymptotic future $r = \infty$. With the initial position and velocity set, the initial acceleration of the particle reads

$$\mathrm{d}_r^2\varphi|_{r=0} = \varphi(0)\left(-\omega^2 + \alpha(\varphi(0)-f)(2\varphi(0)-f)\right). \tag{2.46}$$

By continuously varying the initial position $\varphi(0)$ we can obtain a valid solution with $\varphi(\infty) = 0$. On the one hand, if we set $\varphi(0)$ sufficiently close to $\varphi_{\max}$, the initial acceleration $\mathrm{d}_r^2\varphi|_{r=0}$ can be made correspondingly small. Thus the particle has enough time to remain stationary before the friction term becomes negligible. Consequently, within a finite time, the particle will reach $\varphi_0 = 0$ with nonzero kinetic energy. On the other hand, if we pick $\varphi(0) = \varphi_-$, the particle unavoidably loses energy because of a nonzero friction term and always undershoots. As we vary $\varphi(0)$ continuously, clearly, by the intermediate value theorem, there exists an initial position $\varphi(0) \in (\varphi_-, \varphi_{\max}]$, so that the friction term has exactly the right value in order for φ to reach $\varphi_0 = 0$ at $r = \infty$.

The thin-wall approximation, given by

$$\frac{\omega^2}{\alpha f^2} \ll 1, \quad \text{or equivalently,} \quad \omega^2 \ll m^2, \tag{2.47}$$

allows us to simplify our analysis. In this regime the Goldstone frequency ω is much smaller than the finite mass gap m of the unbroken $SU(N)$ vacuum. We discuss the implications of this from the perspective of quantum physics in a later section.

The energy difference between the two maxima $\varphi_{\max} \simeq f\left(1+\frac{\omega^2}{\alpha f^2}\right)$ and $\varphi_0 = 0$ in the thin-wall regime is approximately

$$V(\varphi_{\max}) \simeq \frac{1}{2}\omega^2 f^2\left(1+\frac{\omega^2}{\alpha f^2}\right). \tag{2.48}$$

To find the radius R of a thin-wall bubble for a given value of ω we extremize the action

$$S = 4\pi\int_0^\infty \left[\frac{1}{2}\left(\mathrm{d}_r\varphi(r)\right)^2 - V\left(\varphi(r)\right)\right] r^2\,\mathrm{d}r, \tag{2.49}$$

evaluated for the bubble solution $\varphi(r)$. In the thin-wall approximation, the particle is close to its initial position near the maximum $\varphi_{\max}$ during the time $r \in (0, R)$. As $\varphi(r)$ is approximately constant on this time interval, the contribution of the $\frac{1}{2}\left(\mathrm{d}_r\varphi(r)\right)^2$ term to the action is negligible in comparison to the contribution of the potential energy $V\left(\varphi(r)\right)$

evaluated at $\varphi_{\max}$. For this part of the action, corresponding to the interior of the bubble, we obtain $S_{\rm int} \simeq -\frac{4\pi}{3} V(\varphi_{\max}) R^3 \simeq -\frac{2\pi}{3}\omega^2 \frac{m^2}{\alpha} R^3$. The most part of the transition of the particle from $\varphi_{\max}$ to $\varphi_0 = 0$ occurs during the time $\Delta r = m^{-1}$. This time interval sets the thickness of the bubble wall $\delta_{\rm w}$. We denote the corresponding portion of the action as $S_{\rm wall} \simeq \frac{2\pi}{3}\frac{m^3}{\alpha} R^2$. For the total action of the thin-wall bubble solution we therefore obtain

$$S_{\rm bubble} = S_{\rm wall} + S_{\rm int} = \frac{2\pi}{3}\frac{m^3}{\alpha}\left(R^2 - \frac{\omega^2}{m} R^3\right). \tag{2.50}$$

We can find the radius R of a stationary bubble by extremizing the action $S_{\rm bubble}$ with respect to R. We thus obtain

$$R = \frac{2}{3}\frac{m}{\omega^2}. \tag{2.51}$$

Note that for $\omega \ll m$ we obtain

$$R \gg \frac{1}{m}. \tag{2.52}$$

This is consistent with the thin-wall approximation $\omega^2 \ll m^2$, where the bubble radius R is much larger than the wall thickness $\delta_{\rm w} \sim m^{-1}$.

The solution $\varphi(r)$ that we found above corresponds to a stationary, spherically symmetric bubble in Minkowski space. The energy of this bubble reads

$$E_{\rm bubble} = E_{\rm wall} + E_{\rm int} = \frac{\omega}{\alpha}\frac{m^5}{\omega^5}\left(\frac{40\pi}{81}\right), \tag{2.53}$$

with

$$E_{\rm int} = \frac{2}{3} E_{\rm wall}, \tag{2.54}$$

where $E_{\rm wall}$ is the energy due to the wall tension and $E_{\rm int}$ is the energy of the interior.

2.3.2 Quantum picture of classical stability

The wall of the bubble consists of mainly the radial excitations of the φ field of mass m. Contrarily, the interior of the bubble consists of mainly the Goldstone excitations of frequency ω. For our analysis it is instructive to express the energies $E_{\rm int}$ and $E_{\rm wall}$ in terms of the corresponding occupation numbers of the respective quanta N_G and N_φ as

$$E_{\rm int} = \omega N_G, \quad \text{with} \quad N_G \equiv \frac{1}{\alpha}\frac{m^5}{\omega^5}\left(\frac{16\pi}{81}\right), \tag{2.55}$$

and

$$E_{\rm wall} = m N_\varphi, \quad \text{with} \quad N_\varphi \equiv \frac{1}{\alpha}\frac{m^4}{\omega^4}\left(\frac{8\pi}{27}\right). \tag{2.56}$$

In the thin-wall approximation, the occupation number of the Goldstone modes is much higher than that of the massive φ quanta for a stationary bubble,

$$\frac{N_G}{N_\varphi} = \frac{2}{3}\frac{m}{\omega} \gg 1. \tag{2.57}$$

We can therefore conclude that the bubble is stationary due to the excitations of the Goldstones. We can view this stability from the perspective of quantum physics. As discussed previously, in the thin-wall approximation of Eq. (2.47), the frequency ω of the Goldstone modes within the bubble is much less than the mass m of the asymptotic quanta in the exterior vacuum. The energy of the interior of the bubble in Eq. (2.55) consists of the excitations of the Goldstone modes. This energy makes up 2/3 of the wall energy, or equivalently, 2/5 of the entire bubble energy.

The bubble is stable due to two reasons: First, the $SU(N)$ charge is conserved. Second, creating a state with the same amount of charge would cost more energy in the unbroken exterior vacuum than in the broken interior vacuum.

As discussed above, in the case that the bubble decays, the $SU(N)$ charge, previously stored in terms of the occupation numbers of the Goldstone modes within the bubble, must be carried away by the outgoing quanta of the unbroken $SU(N)$ vacuum. However, as the minimum energy cost to create one particle in this $SU(N)$-symmetric vacuum is m, which is nonzero, no gapless excitations are possible in this vacuum. Therefore, a state comprised of particles of mass m, that carry the entire $SU(N)$ charge, would cost more energy than the total energy of the bubble by a factor of $\frac{3}{5} + \frac{2}{5}\frac{m}{\omega} \gg 1$. This is the underlying reason for the stability of the bubble.

2.4 Closer look at Goldstones

2.4.1 Goldstones of internal symmetry

The solution in Eq. (2.37) breaks the global $SU(N)$ symmetry spontaneously. This causes the existence of massless Goldstone flavors within the bubble. In the large-N limit, their number scales as $4N \simeq N_{\text{Gold}}$. These Goldstones have a tower of eigenmodes θ^a_ϵ of different eigenfrequencies ϵ. In the limit of an infinite bubble radius these eigenmodes correspond to the momentum modes of the free Goldstone plane waves.

Employing the mode analysis of linearized fluctuations on top of the background of the classical solution we can find the exact form of these mode functions. This will not be covered here as it is not our primary goal. However, we are interested in the eigenmodes of the frequencies $\epsilon = 0$ and $\epsilon = \omega$.

The modes θ^a_0 correspond to $\epsilon = 0$. These modes have zero frequencies and are responsible for the degeneracy of the bubble interior vacuum with respect to the broken $SU(N)$ generators. That is, a set of gapless Goldstone modes is excited when the bubble undergoes a corresponding $SU(N)$ transformation. As these Goldstones are massless, the respective energy cost to excite such a mode is zero. Due to this, the bubbles are degenerate in energy. These bubbles are related by global $SU(N)$ transformations and form irreducible representations under $SU(N)$.

The modes θ^a_ω correspond to $\epsilon = \omega$. These modes are the contents of the bubble. At least some of these modes possess a nonzero occupation number for a stationary bubble. Acting on the bubble solution with an $SU(N)$ rotation we can arbitrarily redistribute

the total occupation number of the Goldstones among the individual θ^a_ω modes, while the energy of the state remains the same.

That is, the modes of the two above frequencies play the following roles in the stationary bubble solution: The Goldstone modes θ^a_ω with frequencies ω are occupied to a total occupation number of N_G. The total energy of these Goldstones corresponds to the energy of the interior of the bubble given by Eq. (2.55). In the ansatz of Eq. (2.37), only the mode flavor $a = 1$ possesses the entire occupation number N_G. However, because the theory is symmetric under $SU(N)$, we can redistribute this total occupation number among the various Goldstone species. All solutions that can be obtained by such an $SU(N)$ rotation are degenerate. The gapless Goldstone bosons θ^a_0 are responsible for this degeneracy in energy.

As discussed above, with an $SU(N)$ transformation we can redistribute the occupation numbers of the individual Goldstones of frequency ω. This can be performed as long as the constraint

$$\sum_a^{2N} n^a = N_G \tag{2.58}$$

(in the large-N limit) is satisfied. A distinct sequence of these occupation numbers n^a results in an individual memory pattern,

$$|\text{pattern}\rangle = |n^1_\omega, n^2_\omega, \ldots\rangle \tag{2.59}$$

that stores information. All of these correspond to classical solutions degenerate in energy and have an energy cost E_{int} given by Eq. (2.55). This is the total energy cost that is necessary to encode the information pattern in terms of the excitations of the Goldstone modes of frequency ω.

Let us emphasize the following point regarding the above information patterns: Consider two distinct memory patterns, $|n^1_\omega, n^2_\omega, \ldots\rangle$ and $|n'^1_\omega, n'^2_\omega, \ldots\rangle$. Furthermore, assume that the differences $\Delta n^a_\omega = |n^a_\omega - n'^a_\omega|$ in occupation number among some modes a are large. Specifically, we consider the case where the ratio $\frac{\Delta n^a_\omega}{N_G}$ is nonzero for $N_G \to \infty$ for some modes a. Such patterns are classically distinguishable.

Now, the patterns that have small differences that vanish in the $N_G \to \infty$ limit constitute subsets of the set of all possible degenerate patterns. These patterns cannot be distinguished classically, but still contribute to the quantum microstate count. We conclude that one part of the memory burden effect can be observed classically, and the other can be observed only at the quantum level.

We remark that in the thin-wall regime of Eq. (2.47), from Eq. (2.55) we obtain

$$N_G \sim \frac{1}{\alpha}\frac{m^5}{\omega^5} \gg \frac{1}{\alpha} \sim N_{\text{Gold}}. \tag{2.60}$$

Note that the number of Goldstone species scales as $N_{\text{Gold}} \sim N$ in the large-N approximation. Furthermore, unitarity of the theory imposes the upper bound $N \sim 1/\alpha$. Thus, for a thin-wall bubble, we obtain that

$$N_G \gg N_{\text{Gold}}. \tag{2.61}$$

In other words, for a bubble in the thin-wall regime, the total Goldstone occupation number N_G greatly exceeds the number of the Goldstone flavors N_{Gold}. For this reason the corresponding memory burden effect is dominated by its classical part. For bubbles of smaller radius the quantum part of the memory burden effect has an equally significant stabilizing role.

In the case that the bubble decays, it releases the quantum information previously stored in the pattern of the form of Eq. (2.59) as external quanta with mass m. Recall that the $SU(N)$ charge is conserved. Therefore, the minimum energy cost corresponding to such a state is

$$E_{\text{pattern}} = mN_G, \tag{2.62}$$

with N_G given in Eq. (2.55). We can rewrite this energy in several convenient forms

$$E_{\text{pattern}} = mN_G = m\frac{1}{\alpha}\frac{m^5}{\omega^5}\left(\frac{16\pi}{81}\right) = \frac{2m}{5\omega}E_{\text{bubble}}. \tag{2.63}$$

We observe that if the bubble decays, the energy cost in the exterior vacuum of the memory pattern corresponding to the information previously stored in the interior of the bubble would be larger than the energy of the bubble by a factor of $2m/(5\omega)$. This is not possible. We therefore conclude that it costs less energy to retain the Goldstone charge in the interior of the bubble, instead of releasing it in terms of the occupied quanta of the exterior vacuum.

We remark that the scenario of releasing the $SU(N)$ charge as smaller bound states with a more favorable mass-to-charge ratio, instead of in the form of free quanta, appears unlikely. Since the coupling α is weak, a bound state of size $R \sim m^{-1}$ would consist of at least $1/\alpha$ particles. Note that because of the energy scale of the problem, $R \sim m^{-1}$ is the smallest possible size a bound state can have. Such an object has the energy $\sim m/\alpha$ and a charge capacity $\sim 1/\alpha$. Such a bound state corresponds to a vacuum bubble with the least possible radius. Evidently, such bound states would not be able to carry the charge of a large bubble that collapsed. In other words, a vacuum bubble cannot decay into multiple smaller bubbles. For a given value of the $SU(N)$ charge, the stationary vacuum bubble configuration obtained above is the optimal solution in terms of energy. That is, at least among the solutions that are spherically symmetric. Our numerical analysis of the problem confirms this.

Note that the theory does not have a parameter that defines the amount of asymmetry for the lowest energy configuration. Such a configuration must exist as it is not possible for it to decay into free quanta. Therefore, non-spherically symmetric deviations from a bubble configuration with zero angular momentum cannot lower its energy.

The fact that there are bubble solutions within this theory is an existence proof for bound states that are able to store the Goldstone charge in a configuration that is more energy-efficient than a set of asymptotic quanta. Therefore, the theory contains bound states that are stabilized by memory burden.

In this regard stationary vacuum bubbles can be viewed as nontopological solitons, or Q-balls [67,68]. These have been studied extensively in the literature. Specifically, Q-balls with arbitrarily small classical charges were considered in [69]. Various related physical

phenomena were also thoroughly investigated, such as the catalysis of proton decay due to symmetry breaking within the Q-ball [70]. Therefore, our work offers an additional perspective on the stability of Q-balls, considering it as a form of memory burden effect.

However, the vacuum bubbles we study differ from Q-balls. The bubbles possess a large microstate entropy, which can also become maximal, saturating the bounds in Eqs. (2.1) and (2.2). Therefore, the information stored in terms of the occupation numbers of the Goldstone modes that stabilize the bubble can be of quantum nature.

This type of stabilization occurs for thick-wall bubbles with $\omega \sim m \sim 1/R$. Here, the quantum portion of the memory burden is as significant as its classical part. This is due to the fact that thick-wall bubbles saturate the bounds in Eqs. (2.1) and (2.2). These saturated bound states are characterized by $N_G \sim N_{\rm Gold} \sim N \sim 1/\alpha$.

2.4.2 Goldstones of broken Poincaré symmetry

We now consider the Goldstones of the broken Poincaré symmetry. These are made up of broken space and time translations. Consequently, the Lorentz boosts are also broken. We study how the various components of the bubble break the space-time symmetries.

The space-translation symmetry is spontaneously broken mostly by the bubble walls. The φ quanta with the corresponding occupation number of N_φ play the main role in this breaking. The contribution of each such quantum into the breaking of space translations is m. Up to order-one numerical factors, we thus find the couplings of the space-translation Goldstones to be

$$G^{(\rm s)}_{\rm Gold} = \frac{R}{mN_\varphi}. \tag{2.64}$$

The time translations are mostly broken by the interior of the bubble because of the nonzero frequency ω of the Goldstones within it. The total occupation number of the Goldstones is N_G. The contribution of each of the Goldstone quanta into the order parameter is ω. Therefore, for we coupling of the time-translation Goldstone bosons we find

$$G^{(\rm t)}_{\rm Gold} = \frac{R}{\omega N_G}. \tag{2.65}$$

From Eq. (2.57), we obtain

$$\omega N_G \sim m N_\varphi. \tag{2.66}$$

We thus observe that the couplings of the space-translation and the time-translation Goldstones are of the same order,

$$G^{(\rm s)}_{\rm Gold} \sim G^{(\rm t)}_{\rm Gold} \sim \frac{R}{\omega N_G}. \tag{2.67}$$

This can also be understood intuitively, as the breaking of time translations by the interior of the bubble stabilizes its walls that break the space-translation symmetry.

Let us emphasize that the expressions in Eqs. (2.66) and (2.67) are valid for any classically stable bubbles, including thick-wall bubbles. Now, we can rewrite the coupling of a

generic Goldstone boson $G^{(\mathrm{P})}_{\mathrm{Gold}}$ corresponding to a broken Poincaré symmetry in terms of the Goldstone occupation number N_G. Using the expression in Eq. (2.51), we obtain

$$G^{(\mathrm{P})}_{\mathrm{Gold}} \sim \frac{R}{\omega}\frac{1}{N_G} \sim \sqrt{\frac{R^3}{m}}\frac{1}{N_G}. \tag{2.68}$$

We can now define the dimensionless effective Poincaré Goldstone coupling $\alpha^{(\mathrm{P})}_{\mathrm{Gold}}$. This coupling is evaluated at the scale $1/R$, which corresponds to the size R of the bubble. As previously, denoting $Area \sim R^2$ as the area of the bubble, we obtain

$$\alpha^{(\mathrm{P})}_{\mathrm{Gold}} \equiv G^{(\mathrm{P})}_{\mathrm{Gold}}\frac{1}{R^2} = \frac{G^{(\mathrm{P})}_{\mathrm{Gold}}}{Area} = \frac{1}{\sqrt{mR}}\frac{1}{N_G} = \frac{\omega}{m}\frac{1}{N_G}. \tag{2.69}$$

We can express the entropy bounds in Eqs. (2.1) and (2.2) in terms of the $SU(N)$ Goldstone occupation number by employing Eqs. (2.68) and (2.69). We thus obtain

$$S_{\max} \sim \frac{1}{\alpha^{(\mathrm{P})}_{\mathrm{Gold}}} \sim \frac{Area}{G^{(\mathrm{P})}_{\mathrm{Gold}}} \sim N_G\sqrt{mR} \sim N_G\frac{m}{\omega}. \tag{2.70}$$

This is the maximum entropy that a bubble can possess in a unitary theory. Below we show that only thick-wall bubbles can saturate this unitarity bound on entropy.

2.5 Spectrum of bubbles

We demonstrated that bubbles are bound states of excited Goldstone modes with the corresponding occupation number N_G. We can write the energy spectrum of the bubbles in terms of this Goldstone occupation number. Thus, for thin-wall bubbles we obtain

$$E_{N_G} = \frac{5}{2}\omega N_G = \frac{5}{\sqrt{6}}\sqrt{\frac{m}{R}}N_G. \tag{2.71}$$

This relation holds for thick-wall bubbles with radius $R \sim 1/m$, up to order-one numerical factors. Below we demonstrate that only thick-wall bubbles can saturate the entropy bound. This occurs when $N_G \sim N \sim 1/\alpha$. The energy of such a saturon vacuum bubble is

$$E_N \sim \frac{N}{R} \sim \frac{1}{\alpha R} \sim \frac{m}{\alpha}. \tag{2.72}$$

In other words, a saturated bubble is a bound state of $N_G \sim N$ Goldstones and $N_\varphi \sim N$ radial modes.

2.6 Entropy of a bubble

In this section we estimate the entropy of a bubble. The number of all possible memory patterns in Eq. (2.59) subject to the constraint in Eq. (2.58) is equal to the total number

of degenerate microstates. We can estimate the number of these degenerate microstates in Stirling's approximation at leading order in large N and N_G as

$$n_{\text{st}} \sim \left(1+\frac{2N}{N_G}\right)^{N_G}\left(1+\frac{N_G}{2N}\right)^{2N}. \tag{2.73}$$

This number of degenerate microstates is typical for solitonic solutions that break the global symmetry spontaneously, as discussed in [20–22]. This can be seen from two complementary viewpoints.

Internal perspective: The microstate degeneracy in Eq. (2.73) represents the degeneracy of the Goldstone vacuum from the viewpoint of the soliton. An observer within the soliton, which is a bubble in our case, observes the SSB of the global $SU(N)$ symmetry and the corresponding emergence of gapless Goldstone species. The resulting broken vacuum is degenerate, like any other Goldstone vacuum. For a bubble of finite radius, there is only a finite number of independent orthogonal vacuum states. For a bubble of infinite size this degeneracy is infinite. Thus, the bubble vacuum is the usual Goldstone vacuum of a four-dimensional theory in the $R \to \infty$ limit. That is, for an internal observer, the various degenerate microstates in Eq. (2.73) correspond to the Goldstone vacua that are related to each other by $SU(N)$ transformations.

External perspective: For an external observer in the asymptotic vacuum, the $SU(N)$ symmetry is unbroken. Therefore, that observer can catalogue all of the states by the representations of the $SU(N)$ group. To the external observer, the vacuum bubble transforms under one such representation, which is exponentially large. This is due to the fact that the bubble consists of a large number of quanta, with each quantum transforming under the adjoint representation of $SU(N)$. We denote the total occupation number of these quanta as N_T. The bubble transforms as a tensor product of N_T adjoint representations. We can represent the wave function of the bubble as the tensor

$$\mathcal{B}^{\beta_1,\ldots,\beta_{N_T}}_{\alpha_1,\ldots,\alpha_{N_T}}. \tag{2.74}$$

This tensor is totally symmetric under both the lower indices $\alpha_1,\ldots,\alpha_{N_T}$ and the upper indices $\beta_1,\ldots,\beta_{N_T}$. The trace of this tensor is zero with respect to each conjugated pair of indices. The dimensionality of this tensor equals the square of the binomial coefficient, to leading order. Again, using Stirling's approximation we can express this dimensionality as

$$n_{\text{st}} \sim \left(1+\frac{2N}{N_T}\right)^{N_T}\left(1+\frac{N_T}{2N}\right)^{2N}. \tag{2.75}$$

As discussed above, it holds that $N_T \simeq N_G$. Using Eq. (2.57), in the thin-wall regime of Eq. (2.47), the total Goldstone occupation number N_G is much larger than the occupation number of the other constituents. Thus, indeed, we obtain $N_T \simeq N_G$. For a thick-wall bubble it holds that $N_\varphi \sim N$. We can therefore state that $N_T \sim N_G$ without loss of generality. Thus, the number of degenerate microstates in Eqs. (2.73) and (2.75) is equal.

Defining $\lambda \equiv 2N/N_G \sim 2N/N_T$, we can calculate the entropy corresponding to this number of degenerate microstates as

$$S = \ln(n_{\rm st}) \simeq 2N \ln\left[(1+\lambda)^{\frac{1}{\lambda}}\left(1+\frac{1}{\lambda}\right)\right]. \tag{2.76}$$

The parameter λ is the ratio of the number of the primary Goldstone species $N_{\rm Gold} \simeq 2N$ to their total occupation number N_G within the bubble. This quantity λ is a measure of saturation of the unitarity bounds by the entropy of the bubble.

2.7 Saturation

In this section we study under which conditions does a bubble saturate the entropy bounds in Eqs. (2.1) and (2.2). One may suggest that we can increase the entropy in Eq. (2.76) indefinitely by increasing N. However, this is impossible as both N and α are subject to the unitarity constraint in Eq. (2.13). Therefore, when the 't Hooft coupling of the theory saturates its upper bound

$$\lambda_{\rm t} = \alpha N \sim 1, \tag{2.77}$$

the parameter N reaches its maximum. An increase of $\lambda_{\rm t}$ beyond this bound leads to a change of the regime. This was discussed in [22]. The breakdown of the loop expansion and the saturation of unitarity by scattering amplitudes both indicate this.

As $N_{\rm Gold} \sim N$, from the saturation of the unitarity bound in Eq. (2.77) we obtain

$$N_{\rm Gold} \sim N \sim \frac{1}{\alpha}. \tag{2.78}$$

This condition needs to be satisfied when calculating the entropy of the bubble. We compute this entropy below both in the thin-wall approximation and in the thick-wall regime.

2.7.1 Entropy of thin-wall bubbles

For a thin-wall bubble, from Eq. (2.55) we obtain

$$N_G \gg \frac{1}{\alpha}. \tag{2.79}$$

In the thin-wall regime, from Eqs. (2.77) and (2.78) we have $\lambda \ll 1$. We can state the above equivalently as

$$N_G \gg N_{\rm Gold} \sim N \sim \frac{1}{\alpha}. \tag{2.80}$$

Thus, for a thin-wall bubble, the entropy in Eq. (2.76) now reads

$$S \simeq 2N \ln\left(\frac{\rm e}{\lambda}\right) \sim \frac{1}{\alpha} \ln\left(\frac{m^{10}}{\omega^{10}}\right). \tag{2.81}$$

To obtain the last term of the above expression we used Eq. (2.77), employing Eq. (2.55) we expressed N_G in terms of α, ω and m. Furthermore, in the logarithm we ignored order-one numerical factors ($8e\pi/81 \sim 1$).

The entropy of such a thin-wall bubble given by Eq. (2.81) is greatly exceeded by the upper bound on the entropy in Eq. (2.2) for the same bubble. Specifically, if we rewrite N_G using Eq. (2.55), we obtain that in the thin-wall regime the maximum entropy in Eq. (2.70) allowed by the Poincaré Goldstone reads

$$S_{\max} \sim \frac{1}{\alpha}\frac{m^6}{\omega^6}. \tag{2.82}$$

Evidently, in the thin-wall regime where $m/\omega \gg 1$, this greatly exceeds the actual entropy of the bubble in Eq. (2.81), as the latter scales logarithmically with m/ω. Therefore, from the perspective of entropy capacity, a thin-wall bubble is an undersaturated bound state.

We can observe the same by considering the entropy bounds imposed by the $SU(N)$ Goldstone bosons. We apply the argument of [22]. We consider an effective dimensionless Goldstone coupling

$$\alpha_{\text{Gold}}^{(SU(N))} = \frac{1}{(fR)^2} \sim \alpha\frac{\omega^4}{m^4}, \tag{2.83}$$

which is taken at the scale $1/R$. The scattering of Goldstones with momentum transfer scale of the process $\sim 1/R$ is controlled by this coupling. We assume the perspective of an observer within the effective low energy theory of the $SU(N)$ Goldstones. This theory has the cutoff $\Lambda_{\text{cutoff}} \sim 1/R$.

For this low energy theory to be consistently valid, the observer needs to verify that it is unitary up to the scale $\sim 1/R$. Due to the mildness of this restriction, the observer may introduce as many as $N_{\text{Gold}} \sim 1/\alpha_{\text{Gold}}^{(SU(N))}$ flavors of Goldstones. By Eq. (2.83), the microstate entropy of a bubble with such a large number of Goldstone species reads

$$S_{\max} \sim \frac{1}{\alpha}\frac{m^4}{\omega^4}. \tag{2.84}$$

The low energy observer would therefore think that it is possible for a bubble of radius R to have such an entropy. However, for this to occur the full theory would have to violate unitarity. Yet the low energy observer cannot know this due to the cutoff of the corresponding low energy theory.

Specifically, note that the value of the parameter N determines the number of the Goldstone flavors within the bubble. Therefore, for the bubble to have the entropy given by Eq. (2.84), N would have to be as large as $N \sim \frac{1}{\alpha}\frac{m^4}{\omega^4}$. However, in this case the full theory would violate the unitarity constraint in Eq. (2.13).

This constraint forbids the number of Goldstone flavors to exceed the value given in Eq. (2.78). This determines the upper bound on the actual entropy capacity of the bubble and is given by Eq. (2.81). The entropy in Eq. (2.81) is much smaller than that in Eq. (2.84). The latter is erroneously assumed by the low energy observer to be the maximal entropy, with the cutoff scale of the corresponding effective low energy theory given by $\Lambda_{\text{cutoff}} \sim 1/R$.

We can thus conclude that the entropy of a thin-wall bubble given in Eq. (2.81) is much smaller than that saturating the bounds in Eqs. (2.1) and (2.2).

2.7.2 Entropy of thick-wall bubbles

The case of thick-wall bubbles, for which $R \sim 1/m$, differs significantly. A classical solution of a stationary bubble, given by Eqs. (2.37) and (2.42), is valid as long as the requirement of Eq. (2.45) is fulfilled, or equivalently if $\omega < m$. For preciseness, we take Eq. (2.45) to be satisfied, and assume that $\omega \sim m$ holds.

For such a bubble configuration we obtain

$$\omega \sim m \sim \frac{1}{R}. \tag{2.85}$$

Consequently, from Eq. (2.55) we have

$$N_G \sim \frac{1}{\alpha}. \tag{2.86}$$

Using the saturation of unitarity in Eq. (2.77), Eq. (2.76) becomes

$$S \sim \frac{1}{\alpha}. \tag{2.87}$$

We therefore conclude that the entropy of such a bubble saturates the unitarity bound in Eq. (2.2).

Correspondingly, this bubble also saturates the area-law bound in Eq. (2.1). In particular, as for such a bubble all three scales in Eq. (2.85) are of the same order, we find that the Poincaré Goldstone coupling in Eq. (2.68) becomes

$$G^{(\mathrm{P})}_{\mathrm{Gold}} \sim \frac{1}{N} Area \sim \alpha Area. \tag{2.88}$$

Evidently, the area-law bound in Eq. (2.1) is saturated by the entropy of the bubble in Eq. (2.87).

Clearly, for a saturated bubble, the couplings of the internal Goldstones and the couplings of the Poincaré Goldstones are equal. Consequently, their corresponding decay constants are also equal. For simplicity, we therefore denote these quantities by G_{Gold} and f, respectively. We also denote the dimensionless Goldstone coupling by α_G from here on.

The couplings and the decay constants of both the internal and the Poincaré Goldstones are given by Eq. (2.6). We express this in the new notation as

$$G_{\mathrm{Gold}} = f^{-2} = \frac{1}{N} Area \sim \alpha Area. \tag{2.89}$$

Furthermore, the fundamental coupling α of the theory is equal to the dimensionless couplings α_G of both the internal and the Poincaré Goldstones, evaluated at the scale $1/R$. Specifically, for a thick-wall bubble we obtain

$$\alpha_G = \frac{G_{\mathrm{Gold}}}{Area} = \frac{1}{(fR)^2} = \alpha. \tag{2.90}$$

Consequently, the entropy of a thick-wall bubble saturates the bounds in Eqs. (2.1) and (2.2) in terms of all couplings and decay constants of the theory.

As discussed in [22], we note that the entropy of a saturated bubble is equal to

$$S \sim E_{\text{bubble}} R. \tag{2.91}$$

This can be obtained by using Eqs. (2.72), (2.87) and (2.85). The entropy in Eq. (2.91) recovers the Bekenstein bound on entropy [28]. However, a priori, this latter bound does not contain any information on the coupling of the system. Contrarily, the bounds in Eqs. (2.1) and (2.2) are more strict, as they prohibit a bubble to have excessive entropy even if the Bekenstein bound on entropy is formally obeyed.

That is, we find that when the theory saturates the bound on unitarity, the bubbles in the thick-wall regime saturate the entropy bounds in Eqs. (2.1) and (2.2). In other words, when the 't Hooft coupling becomes critical (see Eq. (2.13)), a thick-wall bubble becomes a saturon. Thin-wall bubbles, however, are undersaturated bound states. The entropy of these bubbles is greatly exceeded by the bound on entropy within the effective low-energy theory of Goldstone bosons, with the cutoff $\Lambda_{\text{cutoff}} \sim 1/R$. The full theory would have to violate the unitarity constraint in order for the thin-wall bubble to possess such an entropy. We summarize these results in Table 2.1. We note that the same results were obtained in [22] for thin-wall and thick-wall bubbles that were not stabilized by the memory burden effect due to the $SU(N)$ Goldstone charge, but were allowed to oscillate freely and subsequently decay.

	Entropy	
Bubble	Bound on S	Actual S
Thin-wall, $\frac{m}{\omega} \gg 1$	$S \simeq \frac{1}{\alpha}\frac{m^6}{\omega^6}$	$S \simeq \frac{1}{\alpha}\ln\left(\frac{m^{10}}{\omega^{10}}\right)$
Thick-wall, $\frac{m}{\omega} \sim 1$	$S \sim \frac{1}{\alpha}$	$S \sim \frac{1}{\alpha}$

Table 2.1: Entropy bounds and the actual entropies for bubbles in the thin-wall and thick-wall regimes. Evidently, thin-wall bubbles are undersaturated bound states. Only thick-wall bubbles can become saturons.

This exposes a profound relation between the properties of memory burden and the saturation of the entropy bounds. The total occupation number of the Goldstones N_G greatly exceeds the number of the Goldstone flavors $N_{\text{Gold}} \sim N$ for an undersaturated bubble state. Consequently, the memory burden stabilizing such a bubble is classical in nature. However, a saturated bubble can be stabilized by the fully quantum memory burden effect. We study the physics of this below.

2.8 Stabilization by quantum memory burden

We have found above that when the 't Hooft coupling of the theory saturates the unitarity bound in Eq. (2.77), the thick-wall bubble becomes a saturon. We emphasize the

following: Although the solution corresponding to a stationary bubble can be described classically, the memory burden that stabilizes the bubble can be entirely quantum. Let us consider this in detail.

We begin with the ansatz in Eq. (2.37). As mentioned above, in this classical solution a single Goldstone mode, say θ^1, is occupied macroscopically with the corresponding occupation number of $N_G \sim 1/\alpha$, see Eq. (2.86). We can make the occupation number $N_G \sim N$ arbitrarily large by taking the coupling α correspondingly small, as our analysis only improves for weaker α. Up to $\sim 1/N$ corrections, we can regard such a state as classical.

In the thick-wall regime, the number of Goldstone flavors N_{Gold} is of the same order as the total Goldstone occupation number N_G. Furthermore, both of these are of the order of N. For a classical bubble configuration in Eq. (2.37), a single Goldstone flavor possesses the entire occupation number N_G. From the perspective of the memory pattern in Eq. (2.59) we have $n_\omega^a = \delta^{a1} N_G$.

Nevertheless, because of the $SU(N)$ symmetry, with the restriction of Eq. (2.58), the theory allows for bubble solutions in which the occupation number N_G is distributed among the different Goldstone species. These solutions are related via the permitted $SU(N)$ symmetry transformations. This makes them all exactly degenerate in energy.

Within the set of all patterns given by Eq. (2.59), we focus on the ones where the total occupation number N_G is distributed approximately uniformly among all N_{Gold} Goldstone species. For such states, the occupation numbers of all the Goldstone flavors are small, as for a saturated bubble we have $N_G \sim N_{\text{Gold}} \sim N$. Here, the corresponding memory patterns of Eq. (2.59) are characterized by $n_\omega^a \sim 1$ for all a. Thus, the Goldstone modes are all in their respective quantum states, as their individual occupation numbers are microscopic.

The corresponding memory burden possesses the same stabilizing power as that of the classical solution in Eq. (2.37) where $n_\omega^a = \delta^{a1} N_G$, due to the $SU(N)$ symmetry. That is, despite the fact that the bubble states with $n_\omega^a \sim 1$ in Eq. (2.59) are quantum, they have the equivalent stabilizing effect as that of the classical state $n_\omega^a = \delta^{a1} N_G$. Again, these are related to each other by the $SU(N)$ symmetry.

We therefore conclude that saturated thick-wall bubble states are stabilized by the memory burden effect which can be entirely quantum. Such bubbles are similar in their properties to black holes.

2.9 Information horizon

All saturons have a strict information horizon in the semiclassical limit, as discussed in [22]. In other words, in this limit it is impossible to extract any information from the interior of the saturon. We can understand this intuitively as the decoupling of the information-carrying memory modes. Therefore, in the semiclassical limit, the information stored in terms of the occupation numbers of these modes is forever preserved within the saturon.

We show this explicitly for the saturated vacuum bubble solutions within the present theory. Here, the Goldstone modes of the broken $SU(N)$ symmetry correspond to the memory modes. The interaction strength of these modes is suppressed by the corresponding decay constant f. For the effective coupling of a Goldstone mode with frequency ϵ we obtain

$$\alpha_G = \frac{\epsilon^2}{f^2}. \tag{2.92}$$

Below we demonstrate that in the semiclassical limit this coupling vanishes for any finite ϵ.

First, we need to define the correct semiclassical limit. In this limit, the quantum fluctuations do not backreact onto the classical bubble solution of finite size R and frequency ω. Correspondingly, the semiclassical limit is uniquely defined as

$$\alpha \to 0, \quad R = \text{finite}, \quad \omega = \text{finite}, \quad \alpha N = \text{finite}. \tag{2.93}$$

Note that in this limit the mass $m = \sqrt{\alpha} f$ is finite, while the Goldstone decay constant f is infinite. Subsequently, for this limit we obtain

$$f \to \infty, \quad \alpha_G \to 0, \tag{2.94}$$

for any finite frequency ϵ. In other words, the coupling of a Goldstone that has an arbitrarily high finite frequency ϵ goes to zero. Consequently, this also holds for the Goldstone modes with frequencies ϵ exceeding the mass m of the asymptotic quanta in the exterior vacuum. Therefore, in the limit of zero backreaction, no information can be transferred from within the bubble to an observer in the exterior $r \gg R$.

Consider the case when the energy of a Goldstone perturbation greatly exceeds the mass gap of the exterior vacuum. Even such a mode cannot transmit any information to the modes in the outside vacuum. Thus, just like in the case of a black hole, the bubble has an information horizon in the semiclassical limit.

However, even for finite f there exists a Goldstone horizon. At finite f the coupling α_G between the modes is finite. Nevertheless, no Goldstone waves of frequencies $\epsilon \ll m$ can propagate into the exterior vacuum. There are two different cases here.

In the first case the energy of a Goldstone perturbation is less than the mass gap m. Here, no propagation is possible because the energy gap is finite and nonzero.

In the second case the energy of the internal perturbation can be greater than the mass gap at the price of occupying a large number of Goldstones, even if its frequency ϵ is smaller than m. From the classical viewpoint, although the frequency may be very low, the amplitude of the Goldstone wave can be sufficiently high to match the energy given by m.

However, in this case the propagation of the wave is strongly suppressed. We can view this as a process where an initial state of highly occupied soft quanta of frequency $\epsilon \ll m$ and corresponding occupation number n_ϵ transitions into a final state of few quanta with frequencies higher or equal to m. As a specific example, consider $n_\epsilon = m/\epsilon$ Goldstones of frequencies ϵ transitioning into a single mode of mass m in the outside vacuum. This

transition is exponentially suppressed by a factor of e^{-n_ϵ} [22]. Transition processes from high to low occupation numbers are universally exponentially suppressed by such a factor.

2.10 Hawking evaporation

Although stable classically, saturated vacuum bubble states are able to decay via quantum processes. This decay is analogous to the Hawking evaporation of a black hole. This evaporation process occurs universally for all saturons [22]. In the semiclassical limit, similarly to black holes, the bubble evaporates at a thermal rate with a temperature T, which is inversely proportional to its radius R,

$$T \sim \frac{1}{R}. \tag{2.95}$$

In the semiclassical approximation of Eq. (2.93) an outside observer cannot resolve the quantum information contained in the radiated quanta. For a completely quantum theory, the resolution time is defined by Eq. (2.8). Up to numerical factors, this is equal to the Page's time of a black hole.

The asymptotic theory of a physical black hole is gapless, because it contains a massless graviton field. Thus, to elucidate the correspondence between black holes and saturated bubble states we introduce additional massless fields in the exterior vacuum of our theory.

Specifically, we introduce a scalar field ξ_α, which transforms under the fundamental representation of the $SU(N)$ group. Furthermore, we assume that the new theory is the most general $SU(N)$-invariant renormalizable theory of ϕ^β_α and ξ_α. The only condition we impose is that ξ_α is massless in the exterior $SU(N)$-invariant vacuum.

To illustrate the connection between saturated bubbles and black holes we focus on the following terms,

$$\mathcal{L}_\xi = (\partial_\mu \xi^{\dagger\alpha})(\partial^\mu \xi_\alpha) - \alpha_\xi \xi^{\dagger\alpha}(\phi^2)^\beta_\alpha \xi_\beta. \tag{2.96}$$

Here, $\alpha_\xi > 0$ is a coupling constant that obeys the unitarity constraint

$$\alpha_\xi N \lesssim 1. \tag{2.97}$$

This constraint is analogous to the bound in Eq. (2.13) for the coupling α. Again, similarly to α, we take α_ξ close to the saturation point $\alpha_\xi \sim 1/N$ of the above bound.

While the field ξ is massless in the asymptotic unbroken $SU(N)$ vacuum outside of the bubble, its components possess positive mass terms of order $m_\xi^2 \sim \alpha_\xi f^2 \sim m^2$ in the broken $SU(N-1) \times U(1)$ vacuum inside the bubble. Therefore, from the perspective of the field ξ, the bubble is a potential barrier.

First, consider a thin-wall bubble of Eq. (2.47). In this case the wave functions of the ξ modes with momenta $q \ll m$ are exponentially suppressed by a screening factor of $\sim e^{-mR}$ within the bubble, because of their positive mass-squared in its interior.

Now consider a saturated thick-wall bubble. In this case the above suppression is not as powerful. Bubbles in the thick-wall regime obey Eq. (2.85). Therefore, the bubble radius

R is of the same order as the screening depth given by $1/m$. Furthermore, we have $\omega \sim m$. Consequently, the ξ modes and the interior of a saturated bubble have an order-one overlap.

Although the newly added massless field ξ does not influence the classical stability of the bubble, it provides a new quantum decay channel. To obtain the corresponding decay rate within the semiclassical limit, we will need to quantize ξ in the background of the classical bubble solution of Eq. (2.37). However, only thick-wall bubbles can become saturons. The corresponding analytical solution is not known. Therefore, studying a quantized field ξ on top of a classical bubble background will be only qualitative. We do not investigate this here.

Rather, we consider the full quantum theory directly. Here, we employ the universality of Goldstones. Specifically, we exploit the fact that the Goldstone couplings are given by the corresponding symmetry breaking order parameter. Furthermore, recall that the Goldstone modes within the bubble carry most of the quantum information. That is, for an external observer, the processes in which the bubble decays via the Goldstones are the most valuable from the viewpoint of information retrieval.

The Goldstone theorem uniquely defines the couplings between the Goldstones and the modes of the ξ quanta. Moreover, the value of these couplings is set by a single scale. In the framework of the full $(3 + 1)$-dimensional theory, in the vacuum of the broken $SU(N) \times U(1)$ symmetry the coupling between the Goldstone and the ξ modes is local and of the form

$$i\partial_\mu \theta^a \left(\partial^\mu \xi^\dagger T^a \xi - \xi^\dagger T^a \partial^\mu \xi \right) + \cdots . \tag{2.98}$$

Here the dimensionless phases are obtained from the canonically normalized Goldstone fields a^a by $\theta^a \equiv \frac{a^a}{f}$.

In an infinitely large vacuum with the $SU(N-1) \times U(1)$ symmetry, the Goldstones are well defined everywhere. Plane waves represent the mode expansions of both the Goldstones and the ξ quanta. An $SU(N-1) \times U(1)$ vacuum of finite extent, such as in a bubble of finite radius R, changes the mode expansion and the configurations of momentum eigenstates. Specifically, only the bubble interior is inhabited by the Goldstones, which become ill-defined in the exterior vacuum. The scattering between the Goldstones of frequency ω and the ξ modes is controlled by the effective coupling $\alpha_G(\omega) = \frac{\omega^2}{f_\omega^2}$. The effective scale f_ω possesses all of the information regarding the mode profiles and other factors. For a saturated thick-wall bubble we have $f_\omega \sim f$. Again, this is due to the fact that for a saturated bubble, all of the scales are of the same order; see Eq. (2.85). We therefore obtain that the coupling that controls all of the relevant Goldstone processes is given by $\alpha_G = \frac{\omega^2}{f^2}$.

Energy and Goldstone charge conservation are not an issue regarding the bubble decay, as the ξ quanta are massless. However, a decay of a bubble into a large number of ξ modes is very unlikely, as each elementary vertex involving ξ is suppressed by the coupling α_G. Therefore, such an explosive bubble decay process does not constitute a substantial decay channel. In the case of a black hole, a process where the black hole decays explosively into a large number of soft gravitons is analogously suppressed.

There are two types of leading order processes of bubble evaporation. The first cor-

responds to the decays of Goldstones of frequency ω into pairs of ξ quanta. The second describes the rescatterings of pairs of Goldstone quanta into the asymptotic ξ quanta. The rates corresponding to the two categories of these processes read

$$\Gamma_{1\to 2} \sim \omega \alpha_G N_G \sim 1/R \tag{2.99}$$

and

$$\Gamma_{2\to 2} \sim \omega \alpha_G^2 N_G^2 \sim 1/R, \tag{2.100}$$

respectively, where we used the fact that saturated bubbles obey Eq. (2.85) and employed the property $N_G \sim N_{\rm Gold} \sim 1/\alpha_G$. Rescattering processes which include a higher number of Goldstone quanta are more suppressed. For the decay rate of a saturated bubble we therefore obtain

$$\Gamma_{\rm decay} \sim 1/R. \tag{2.101}$$

This decay rate is equivalent to the Hawking rate of an evaporating black hole. Similarly to a black hole, a saturated bubble emits, on average, a quantum of energy $\Delta E \sim 1/R$ during a time interval $\Delta t \sim R$. Therefore, the power of the radiation emitted by the bubble is given by

$$P \sim \frac{1}{R^2} \sim T^2. \tag{2.102}$$

This is nothing else than the power of radiation of a black hole of temperature T given by Eq. (2.95).

For the bubble to emit ξ quanta of energies $E \gg 1/R$, a large number n of Goldstone quanta need to rescatter into a small number of ξ quanta. Processes such as these are strongly suppressed. Specifically, creating $n \gg 1$ of the ξ quanta with energies $E = n/R$ requires the rescattering of $\sim n$ Goldstone quanta. Such processes are additionally suppressed by a factor of e^{-n}, typical for $n \to 2$ processes for $n \gg 1$ [22].

Therefore, an exponential factor of the type

$$\Gamma_{E\gg T} \sim \mathrm{e}^{-ER} \tag{2.103}$$

suppresses the rate of emission of quanta with an energy of $E \gg 1/R$. The suppression factor in Eq. (2.103) can be equivalently viewed as the Boltzmann factor

$$\Gamma_{E\gg T} \sim \mathrm{e}^{-\frac{E}{T}}. \tag{2.104}$$

This is typical for thermal radiation with a corresponding temperature of $T \sim 1/R$, as given by Eq. (2.95). One may therefore expect the saturon state to be thermal. However, this is in contradiction to the full microscopic theory. In particular, the radiation spectrum possesses $1/N$, or equivalently $1/S$, non-thermal corrections. These corrections carry the information about the purity of the state. An observer can fully specify in which pure state the saturon is, only after fully resolving these corrections. The time necessary for the observer to resolve these corrections is rather long and is given by Eq. (2.8). We study this property below.

2.11 Information in Hawking radiation

We now study how Hawking radiation extracts information from the bubble. First, note that in the semiclassical limit of Eq. (2.93), the quantum information encoded in the emitted quanta is completely unresolvable. This is evident as in this limit, all of the quantum couplings vanish, α_G, α_ξ, $\alpha \to 0$. Thus, an external observer cannot resolve the $SU(N)$ quantum numbers of the emitted radiation. The evaporation rate in Eq. (2.101) and the power of the outgoing radiation in Eq. (2.102) remain finite in this limit at the price of infinite N_G.

An external observer therefore perceives the radiation as exactly thermal with the temperature given by Eq. (2.95), and cannot resolve the information contained within it on a finite timescale. Again, in the semiclassical limit of Eq. (2.93), a saturon bubble processes information just like a black hole. We analyze this in detail below.

We consider the evaporation of two distinct saturon bubbles. These bubbles possess different information patterns, given by $|n^1_\omega, n^2_\omega, \ldots\rangle$ and $|n'^1_\omega, n'^2_\omega, \ldots\rangle$. These patterns are related by an $SU(N)$ transformation and obey Eq. (2.58).

We emphasize that although $SU(N)$ commutes with the Hamiltonian of the theory, the two bubbles possess distinct memory patterns. Again, the quantum information patterns are related to each other by an $SU(N)$ transformation. Therefore, the interaction of the corresponding states with a fixed reference probe will differ.

From the previous findings we recall that for a saturon bubble, the following holds,

$$\alpha \sim \alpha_G \sim \alpha_\xi \sim \frac{1}{N_{\text{Gold}}} \sim \frac{1}{N_G} \sim \frac{1}{N}. \tag{2.105}$$

In other words, all of the collective couplings are critical, and the total occupation number of Goldstones N_G is of the order of the number of Goldstone flavors N_{Gold}, which is also of the order N.

For a saturated bubble, the above relation holds both in the semiclassical limit and in the full quantum theory. The distinction is that in the full quantum theory, despite the fact that all numbers are large and, correspondingly, all couplings are weak, these are all finite. However, in the semiclassical regime all three numbers are infinitely large while all three couplings are infinitely weak.

We can therefore summarize the two regimes of a saturon bubble as

$$\alpha \sim \alpha_G \sim \alpha_\xi \sim \frac{1}{N_{\text{Gold}}} \sim \frac{1}{N_G} \sim \frac{1}{N} = \begin{cases} \neq 0, \ll 1 & \text{in full quantum theory,} \\ = 0 & \text{in semiclassical theory.} \end{cases} \tag{2.106}$$

We now compare the radiation emitted by the two bubbles above. All $SU(N)$-invariant properties of the decay are the same for the two bubbles, as the two corresponding memory patterns are related by an $SU(N)$ transformation. One of these common characteristics is the decay rate in Eq. (2.101).

An observer has to carry out a measurement that is sensitive to the differences Δn^a_ω among the individual occupation numbers of the two information patterns, to be able

to distinguish the two corresponding bubbles. In the semiclassical approximation this can be done only if some of the ratios $\Delta n^a_\omega / N_G$ are finite. That is, the observer can only distinguish information patterns that differ classically. The relative fraction of such memory patterns goes to zero in the $N_G \to \infty$ limit. The patterns for which the differences in the individual occupation numbers are small carry the majority of the information. Such patterns are indistinguishable in the semiclassical limit. Consistently, in this limit, the quantum information encoded in the radiation emitted by the bubble cannot be recovered on a finite timescale.

Contrarily, within the full quantum theory, the difference in the radiation emitted by the two bubbles with distinct corresponding patterns can be resolved within a finite time, even if the differences Δn^a_ω are of order one. These differences are encoded in deviations which are of order $1/N_G$ or, equivalently, of order $1/S$.

We illustrate the corresponding radiation process within the effective theory of the bubble as a composite state that transforms as the $SU(N)$ tensor representation given in Eq. (2.74). The effective coupling of the bubble and the ξ quanta reads

$$\mathcal{B}^{\beta_1,\beta_2,\ldots,\beta_{N_T-1},\beta_{N_T}}_{\alpha_1,\alpha_2,\ldots,\alpha_{N_T-1},\alpha_{N_T}} \xi^{\dagger\alpha_{N_T}} \xi_{\beta_{N_T}} \tilde{\mathcal{B}}^{\alpha_1,\alpha_2,\ldots,\alpha_{N_T-1}}_{\beta_1,\beta_2,\ldots,\beta_{N_T-1}} . \tag{2.107}$$

Here, $\tilde{\mathcal{B}}^{\alpha_1,\alpha_2,\ldots,\alpha_{N_T-1}}_{\beta_1,\beta_2,\ldots,\beta_{N_T-1}}$ is the operator that corresponds to a bubble transforming under a smaller representation of $SU(N)$. The emission process can be written as

$$\mathcal{B}^{\beta_1,\beta_2,\ldots,\beta_{N_T-1},\beta_{N_T}}_{\alpha_1,\alpha_2,\ldots,\alpha_{N_T-1},\alpha_{N_T}} \to \xi_{\alpha_{N_T}} + \xi^{\dagger\beta_{N_T}} + \tilde{\mathcal{B}}^{\beta_1,\beta_2,\ldots,\beta_{N_T-1}}_{\alpha_1,\alpha_2,\ldots,\alpha_{N_T-1}} . \tag{2.108}$$

We can visualize this process in the notation of 't Hooft as a planar diagram shown in Fig. 2.1. Here, the flows of global $SU(N)$ "color" and "anticolor" are denoted by oppositely directed arrows.

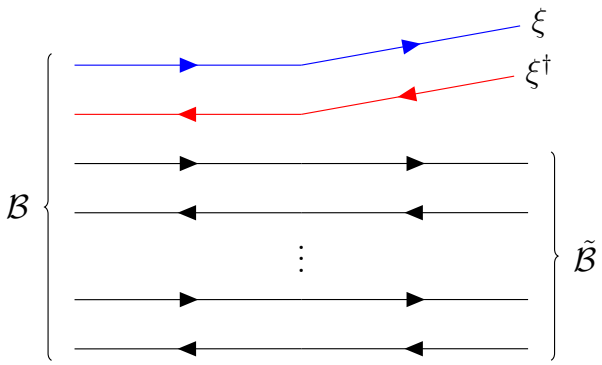

Figure 2.1: The decay process $\mathcal{B} \to \tilde{\mathcal{B}} + \xi + \xi^\dagger$ as a planar diagram in 't Hooft's notation. The flow of $SU(N)$ color and anticolor is denoted by oppositely directed arrows. The red and blue lines denote the quantum numbers carried away by the emitted ξ quanta.

Let us emphasize the usefulness of this diagrammatic visualization in understanding the emission of information by the bubble. Specifically, we can clearly see that a single emission

possesses a negligible fraction of the information stored within the bubble. Moreover, the origin of the exponential suppression factor in Eq. (2.104) is evident. A diagram of the characteristic process contributing to the radiation of highly energetic ξ quanta is given in Fig. 2.2.

Finally, the backreaction onto the bubble due to the emission is of order $1/N$. In the semiclassical treatment of Eq. (2.93), clearly, the initial bubble state $\mathcal{B}$ and the final bubble state $\tilde{\mathcal{B}}$ are indistinguishable. In the full quantum theory, that is for a finite N, the distinction is nonzero. Nevertheless, the time to detect this difference scales with N. This sets the timescale necessary for the extraction of information. We study this below.

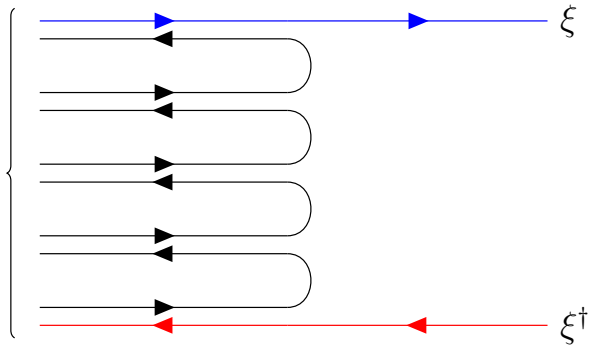

Figure 2.2: Diagram of a many $\to$ 2 scattering process, which results in the emission of highly energetic ξ quanta.

2.12 Timescale of information retrieval

In this section we consider the timescale of the retrieval of information carried by Hawking radiation. In the work [22] it was suggested that any saturon possesses a universal lower bound on the timescale on which information retrieval can start. This bound is given by Eq. (2.8). Applying the logic of [22] to the theory of this chapter, we can verify that this relation is reproduced for a saturon bubble. We have previously demonstrated that thick-wall bubbles of Eq. (2.85) can become saturons with their properties satisfying Eq. (2.105).

As already discussed, the bubble stores quantum information in terms of the occupation numbers of Goldstone modes in a corresponding memory pattern given by Eq. (2.59). Consequently, an interaction involving the Goldstone modes is necessary to extract any quantum information from a bubble. The specific procedure of the corresponding measurement is arbitrary, as long as the Goldstone modes interact with some "agents" that carry $SU(N)$ quantum numbers in the exterior vacuum. There exist two categories of information recovery: Passive and proactive. We discuss these below.

2.12.1 Passive retrieval

In the case of passive information retrieval, an outside observer needs to examine the properties of the Hawking radiation emitted by the bubble. As previously mentioned, up to the zeroth order in $1/N$, or $1/S$, the radiation carries no information. To recover the information contained in the radiation, the observer needs to resolve these $1/S$ deviations. To do this, the external observer has to measure the $SU(N)$ content of the radiation. This measurement requires a long time, due to the following two reasons.

First, for the initial stage of the emission, the radiated quanta carry only a very small fraction of the total information of the bubble. Consider the decay of one Goldstone mode into two ξ quanta. From the viewpoint of the information pattern, this process can be seen as a "spontaneous emission", where the occupation number of one of the Goldstones, say n^1_ω, decreases by one,

$$|n^1_\omega, n^2_\omega, \ldots\rangle \to |n^1_\omega - 1, n^2_\omega, \ldots\rangle + \xi^\dagger + \xi. \tag{2.109}$$

Correspondingly, the $SU(N)$ charge of the decaying Goldstone mode is carried by the ξ quanta. The characteristic wavelength of these emitted ξ quanta is of order R.

An external observer who would like to decode the charge of the radiated ξ particles must pass these through a detector containing some sample particles. If such a detector is maximally packed, it contains probe quanta with an occupation number of $N_\xi \sim 1/\alpha_\xi$ per de Broglie volume $\sim R^3$. The maximum interaction rate for an emitted ξ particle with such a detector is given by $\Gamma_\xi \sim \alpha_\xi^2 N_\xi / R \sim \alpha_\xi / R$. Consequently, the minimum time necessary to be able to resolve the quantum numbers of ξ is

$$t_\xi \sim \frac{R}{\alpha_\xi} \sim SR \sim R^3 f^2. \tag{2.110}$$

However, the measurement of a single emitted quantum does not allow to gain a significant amount of information regarding the information pattern of the bubble. To obtain a sufficient amount of information stored in terms of the occupation numbers of the Goldstone modes within the bubble, at least $\sim N_G$ emitted quanta would need to be measured.

The detection of this number of quanta requires a measurement time of

$$t_{\min} \sim N_G R. \tag{2.111}$$

Again, due to saturation and Eq. (2.105), this time is of the same order as that in Eq. (2.110).

We can therefore summarize with the following: An external observer has to detect $\sim N_G$ radiated particles and measure their $SU(N)$ quantum numbers, to be able to obtain any reasonable amount of information about the $SU(N)$ charge content of the bubble. Both of the timescales corresponding to these processes are given by Eq. (2.110). This timescale is also of the order of that in Eq. (2.8).

2.12.2 Proactive retrieval

There is a different option for an external observer to measure the quantum information contained within the bubble. Namely, the observer can proactively scatter probe particles at the bubble and measure the scattering products, instead of passively waiting for a sufficient portion of the bubble to evaporate. Below we demonstrate that in this scenario the minimum timescale for the onset of information recovery is given by Eq. (2.8).

The underlying reason for this is that $t_{\rm min}$ must be larger than the interaction time between the external probe quanta and the information carrying Goldstone modes. Irrespective of the experimental realization of the scattering process, the Goldstone theorem sets the interaction time in terms of the Goldstone decay constant f.

The interaction rate of the scattering process is suppressed by the square of the coupling α_G, which is taken at the scale $\omega \sim 1/R$. However, the rate is enhanced by the total Goldstone occupation number N_G. In total, the interaction rate is given by

$$\Gamma_{\rm Gold} \sim \alpha_G^2 m N_G \sim \frac{1}{R^3 f^2}. \tag{2.112}$$

The corresponding timescale is then

$$t_{\rm min} = \frac{1}{\Gamma_{\rm Gold}} \sim R^3 f^2. \tag{2.113}$$

This defines the minimum time for the onset of information retrieval by this proactive extraction method. By using the saturation relations we can express the above timescale as

$$t_{\rm min} \sim SR \sim \frac{R}{\alpha}. \tag{2.114}$$

That is, we obtain that, up to numerical factors, the minimum time necessary for the onset of information recovery for both the passive and the proactive extraction methods is given by Eq. (2.8).

We thus recover the result of [22], where it was discussed that generic saturons obey the universal lower bound on the minimal timescale of information retrieval, given in Eq. (2.8). Black holes are therefore not special in this regard: The Page time of a black hole of size R is equal to the time $t_{\rm min}$ for a generic nongravitational saturon of the same size.

Note that the information retrieval time in Eq. (2.113) is in agreement with the notion of an information horizon in the semiclassical approximation. Specifically, from Eqs. (2.93) and (2.94) we obtain that, in the semiclassical limit, the timescale $t_{\rm min}$ becomes infinite. Therefore, with the help of Eqs. (2.113) and (2.114) we can understand why a generic saturon has a strict information horizon in the semiclassical limit of the corresponding theory.

As a final remark, we emphasize that the mechanisms underlying the properties of Hawking radiation and the information recovery timescales are in agreement with the results provided by the framework of the quantum N-portrait of a black hole [14, 16, 60]. This should not be a surprise as within the quantum N-portrait a black hole is regarded as

a saturated bound state of N soft gravitons. Due to the arguments of universality discussed here, the two systems must have similar behavior. At the end of this chapter we provide more comments on the correspondence of black holes and generic saturons.

2.13 Numerical results

To perform a numerical analysis of the problem, we consider the case where a single Goldstone flavor $\theta^a = \delta^{a1}\theta(x)$ is occupied macroscopically. We can then rewrite the Lagrangian density in Eq. (2.12) in terms of the fields φ and θ as

$$\mathcal{L} = \frac{1}{2}\left(\partial_\mu\varphi\right)\left(\partial^\mu\varphi\right) + \frac{N}{4(N-1)}\varphi^2\left(\partial_\mu\theta\right)\left(\partial^\mu\theta\right) - \frac{\tilde{\alpha}}{2}\varphi^2\left(\varphi - \tilde{f}\right)^2, \tag{2.115}$$

where $\tilde{\alpha}$ and $\tilde{f}$ are defined above in Eq. (2.36). To allow for a simpler implementation, we define

$$\Psi = \frac{1}{\sqrt{2}}\rho e^{i\chi/\tilde{f}}, \tag{2.116}$$

where

$$\rho \equiv \varphi, \quad \chi \equiv \sqrt{\frac{N}{2(N-1)}}\tilde{f}\theta. \tag{2.117}$$

We can recover the original fields φ and θ as

$$\varphi = \sqrt{2}\left|\Psi\right|, \quad \theta = \sqrt{\frac{2(N-1)}{N}}\mathrm{Arg}\left(\Psi\right), \tag{2.118}$$

respectively. In terms of the field Ψ the Lagrangian density takes the form of

$$\mathcal{L} = \left(\partial_\mu\Psi^*\right)\left(\partial^\mu\Psi\right) - \tilde{\alpha}\left|\Psi\right|^2\left(\sqrt{2}\left|\Psi\right| - \tilde{f}\right)^2. \tag{2.119}$$

Correspondingly, the equations of motion for Ψ read

$$\Box\Psi + \tilde{\alpha}\Psi\left(\sqrt{2}\left|\Psi\right| - \tilde{f}\right)\left(2\sqrt{2}\left|\Psi\right| - \tilde{f}\right) = 0. \tag{2.120}$$

As initial field configurations at $t = 0$ we could use

$$\Psi(t,r)|_{t=0} = \frac{\tilde{f}}{2\sqrt{2}}\left[1 + \tanh\left(\frac{m(R_0 - r)}{2}\right)\right] \tag{2.121}$$

and

$$\partial_t\Psi(t,r)|_{t=0} = i\tilde{\omega}\frac{\tilde{f}}{2\sqrt{2}}\left[1 + \tanh\left(\frac{m(R_0 - r)}{2}\right)\right]. \tag{2.122}$$

Here, r is the radial coordinate of $(3+1)$-dimensional space-time, R_0 is the bubble radius at $t = 0$, $\tilde{\omega}$ is the initial frequency of the internal rotation of the field χ, and $m = \sqrt{\tilde{\alpha}}\tilde{f} = \sqrt{\alpha}f$ as before. We can express these initial conditions equivalently as

$$\varphi(t,r)|_{t=0} = \frac{\tilde{f}}{2}\left[1 + \tanh\left(\frac{m(R_0 - r)}{2}\right)\right] \tag{2.123}$$

and

$$\dot{\theta} \equiv \partial_t \theta(t,r)|_{t=0} = \sqrt{\frac{2(N-1)}{N}}\tilde{\omega}\,, \tag{2.124}$$

respectively.

However, note that the above ansatz is valid only in the thin-wall approximation. Furthermore, we can obtain more exact initial profiles of the fields by solving Eq. (2.40) numerically. We set this solution as the initial conditions for our simulation. This has two benefits: First, we improve the accuracy of our numerical analysis, and second, we can extend our study to that of thick-wall bubbles.

With the initial configurations obtained from Eq. (2.40), we solve the full equations of motion for $\Psi(t,r)$ in $(3+1)$ space-time dimensions. In our simulations we set $\tilde{\alpha}=1$ and $\tilde{f}=1$ throughout. For simplicity, we again absorb the N-dependent factors into the definitions of $\tilde{\alpha}$, $\tilde{f}$ and $\tilde{\omega}$, resulting in α, f and ω, respectively. From the simulations, we obtain that for a certain critical value of the frequency, which we denote by ω_c, as expected, the bubble is stabilized. The corresponding result is shown in Fig. 2.3. That is, a certain critical Goldstone mode occupation number, set by ω_c, stabilizes the bubble and prevents it from collapsing. Specifically, ω_c corresponds to the frequency in Eq. (2.51). We find this expression again below from the requirement of the conservation of the $SU(N)$ charge. Furthermore, we extend the calculation to estimate the frequency of the bubble-wall oscillations about a static bubble configuration.

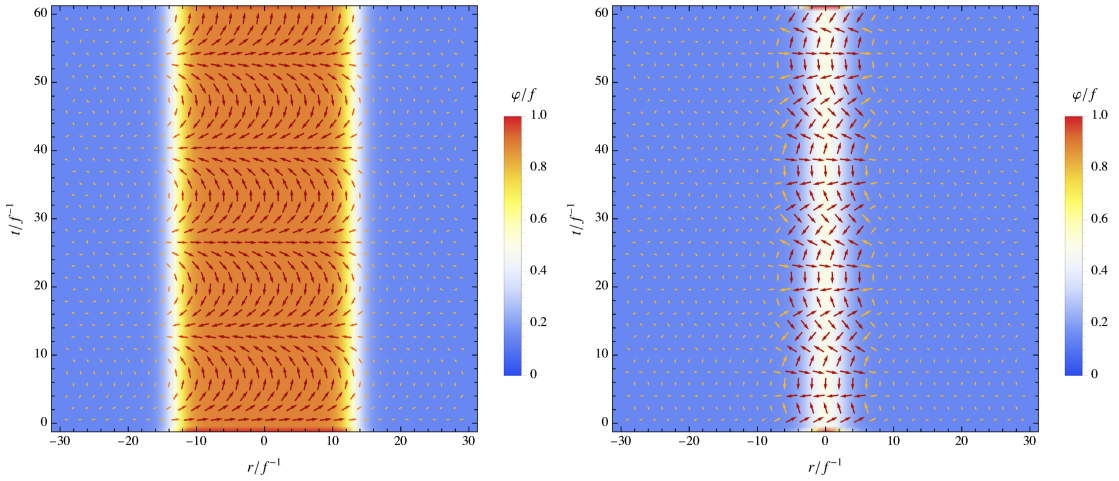

(a) (b)

Figure 2.3: Numerical simulations of the time-evolution of bubbles with initial radii of (a) $R_0 \simeq 13.2/f^{-1}$, (b) $R_0 \simeq 2.5/f^{-1}$. Both bubbles are stable for a certain respective critical frequency ω_c. The color bar represents the value of $\sqrt{2}|\Psi(t,r)|/f = \varphi(t,r)/f$. This is plotted over the radial and time coordinates, r/f^{-1} and t/f^{-1}, respectively. The arrows correspond to the vector $\sqrt{2}\Psi(t,r)/f$ on the complex plane, indicating the value of $\theta(t,r)$.

2.13.1 Critical frequency estimate

As before, we assume our problem to possess spherical symmetry. In the thin-wall approximation, we can write the total energy of the bubble of radius $R \gg 1/m$ as

$$E = \frac{2\pi}{3\alpha} m^3 R^2 \left(1 - \dot{R}^2\right)^{-1/2} + \frac{2\pi}{3\alpha} m^2 \omega^2 R^3. \tag{2.125}$$

Here we also assumed $\omega = \omega(R)$ to be homogeneous in space. We aim to find an expression for ω, for the value of which the bubble is stabilized. We begin from the fact that the $SU(N)$ charge

$$Q = -i \int \left(\Psi^* \partial_t \Psi - \Psi \partial_t \Psi^*\right) r^2 \, \mathrm{d}r \tag{2.126}$$

is conserved in time. That is, $\dot{Q} = 0$. For a thin-wall bubble the charge becomes

$$Q = \frac{2\pi}{3} f^2 \omega R^3 = \frac{2\pi}{3\alpha} m^2 \omega R^3. \tag{2.127}$$

Using Eq. (2.127) in Eq. (2.125), for the total energy of the bubble we obtain

$$E = \frac{2\pi}{3\alpha} m^3 R^2 \left(1 - \dot{R}^2\right)^{-1/2} + \frac{2\pi}{3\alpha} m^2 \left(\frac{3\alpha Q}{2\pi m^2 R^3}\right)^2 R^3. \tag{2.128}$$

For a static bubble configuration we have $\dot{R} = 0$. Consequently, the total energy in the expression above simplifies to

$$E = \frac{2\pi}{3\alpha} m^3 R^2 + \frac{3\alpha Q^2}{2\pi m^2 R^3}. \tag{2.129}$$

Now, solving $\frac{\mathrm{d}E}{\mathrm{d}R} = 0$ for R, we obtain

$$R_0 \equiv \left[\frac{3}{2}\left(\frac{3\alpha Q}{2\pi}\right)^2\right]^{1/5} m^{-1}. \tag{2.130}$$

Finally, using Eq. (2.127), we find that the critical frequency for which the bubble is stable is equivalent to that in Eq. (2.51) and reads

$$\omega_\mathrm{c} = \sqrt{\frac{2m}{3R_0}}. \tag{2.131}$$

The initial bubble radius is denoted by R_0 in the initial conditions of the numerical simulations below. The total energy and the total $SU(N)$ charge for a static bubble configuration are given by

$$E_0 \equiv \frac{40\pi m^5}{81\alpha\omega_\mathrm{c}^4} \quad \text{and} \quad Q_0 \equiv \frac{16\pi}{81\alpha}\left(\frac{m}{\omega_\mathrm{c}}\right)^5, \tag{2.132}$$

respectively.

In this section we verify the above findings and analyze how the system behaves in various frequency regimes. Additionally, we can estimate the frequency of the radius oscillations ω_0 in the near-critical frequency regime as follows: Let $R = R_0 + \delta R$. The total energy of the bubble given in Eq. (2.125) now reads

$$E = \frac{10\pi m^3 R_0^2}{9\alpha} + \left(\frac{\pi m^3 R_0^2}{3\alpha}\right)\delta\dot{R}^2 + \left(\frac{10\pi m^3}{3\alpha}\right)\delta R^2 + \mathcal{O}\left(\delta R^3, \delta R^2\delta\dot{R}, \delta R\,\delta\dot{R}^2, \delta\dot{R}^3\right). \quad (2.133)$$

From the above, we obtain that the frequency of the radius oscillations is given by

$$\omega_0 \equiv \sqrt{10}R_0^{-1} = \sqrt{10}\frac{3\omega_c^2}{2m}. \quad (2.134)$$

We investigate this also numerically below.

2.13.2 Critical frequency regime

For a critical Goldstone occupation number, corresponding to ω_c, a vacuum bubble is stable. We show this in Fig. 2.3. We demonstrate below that bubbles in the low frequency regime, in particular with $\omega = 0.1\omega_c$, collapse at a time $t_{col} \sim R_0$. However here, in the critical frequency regime, the bubbles have not collapsed at $4t_{col} \simeq 60/f^{-1}$.

Now, for a frequency that differs slightly from ω_c, the bubble radius oscillates about its mean position R_m. We observe at least two frequencies characterizing these oscillations. We present the corresponding results of this near-critical regime in Fig. 2.4.

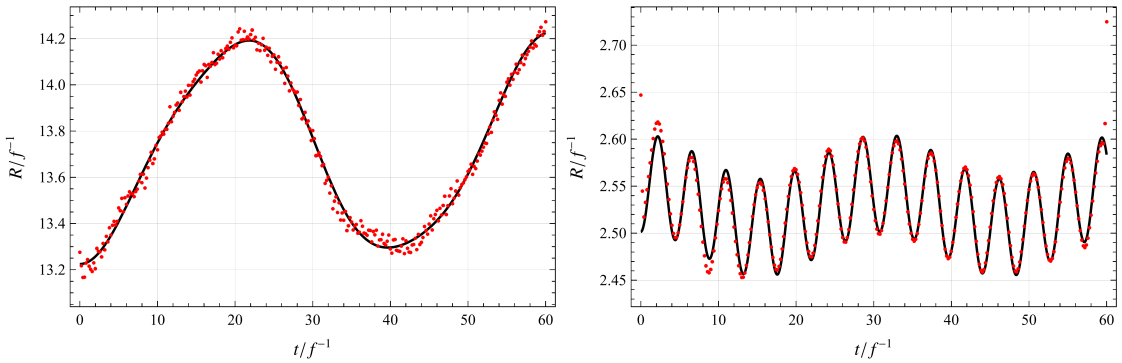

(a) (b)

Figure 2.4: Bubble radius oscillations in the near-critical frequency regime for a frequency $\omega = 1.1\omega_c$. The individual panels show the numerical data for the bubble radius R/f^{-1} in red over time t/f^{-1}. The radius is determined by the coordinate r corresponding to the maximum of the energy density. The numerical fits of these data $R(t) = R_m + A_0\cos(\omega_0 t) + A_1\cos(\omega_1 t)$ are shown in black. The initial radii of the respective simulations are (a) $R_0 \simeq 13.2/f^{-1}$, (b) $R_0 \simeq 2.5/f^{-1}$.

The fit parameters of the fit function $R(t) = R_m + A_0\cos(\omega_0 t) + A_1\cos(\omega_1 t)$ in figure 2.4 read as follows: For the large bubble we obtain: $R_m = 13.730 \pm 0.002$, $A_0 = -0.464 \pm 0.003$,

$\omega_0 = 0.1537 \pm 0.0002$, $A_1 = -0.042 \pm 0.002$ and $\omega_1 = 0.370 \pm 0.002$. The coefficient of determination $\overline{R}^2$ and the unbiased root-mean-square error (RMSE), both adjusted for the number of fit-model parameters, are 0.999995 and 0.0301, respectively. For the small bubble we have: $R_m = 2.5297 \pm 0.0004$, $A_0 = -0.0519 \pm 0.0005$, $\omega_0 = 1.4287 \pm 0.0003$, $A_1 = -0.0237 \pm 0.0005$ and $\omega_1 = 0.2023 \pm 0.0006$, with $\overline{R}^2 = 0.999994$ and RMSE = 0.00599. Four outlier data points were excluded from the fit for the small bubble. Both numerically obtained estimates of ω_0 are close to the analytical result of $\omega_0 = \sqrt{10}R_0^{-1}$ from above. Specifically, we have $\omega_0 = 0.264$ for the large bubble and $\omega_0 = 3.11$ for the small bubble.

2.13.3 Low frequency regime

The bubble decays for sufficiently low values of the frequency ω. This is due to the fact that in this case the tension of the bubble wall greatly exceeds the pressure due to the rotation of the χ field. Therefore, the bubble collapses. We have numerically obtained the result that the bubble collapses for $\omega = 0$. This case has been thoroughly investigated in the existing literature. In our study we consider the case $\omega = 0.1\omega_c$. We find that also in this case the bubble collapses. Our results are shown in Fig. 2.5. From the simulation for the large bubble, we can estimate its collapse time as $t_{\text{col}} \simeq 1.1R_0 \simeq 15/f^{-1}$. For the small bubble we estimate its collapse time to be $t_{\text{col}} \sim R_0$.

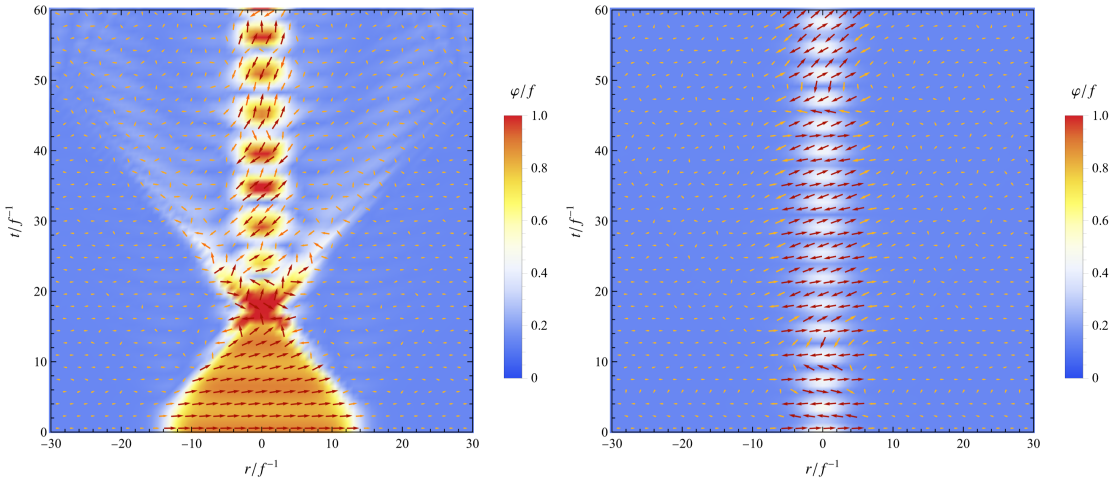

Figure 2.5: Numerical simulations of the time-evolution of bubbles in the low frequency regime $\omega = 0.1\omega_c$ for different initial radii (a) $R_0 \simeq 13.2/f^{-1}$, (b) $R_0 \simeq 2.5/f^{-1}$. For such low frequencies, the bubbles collapse.

2.13.4 High frequency regime

In the high frequency regime, where $\omega > \omega_c$, the time-evolution of the bubble begins with its expansion. The corresponding simulation results are presented in Fig. 2.6. This

should not be surprising, as initially the pressure from the internal rotation exceeds the tension of the bubble wall. After the bubble expands to a radius where the wall tension is able to counterbalance the internal pressure, it begins to shrink back. Subsequently, these oscillations repeat. Note, however, that a part of the energy is emitted. This is also expected, and is a consistency check for our numerical simulations. In the semiclassical approximation, as discussed above, the energy of the bubble is infinite. Consequently, any finite gap results in the propagation of waves emitted by the oscillating bubble. This is precisely what we observe in our simulations.

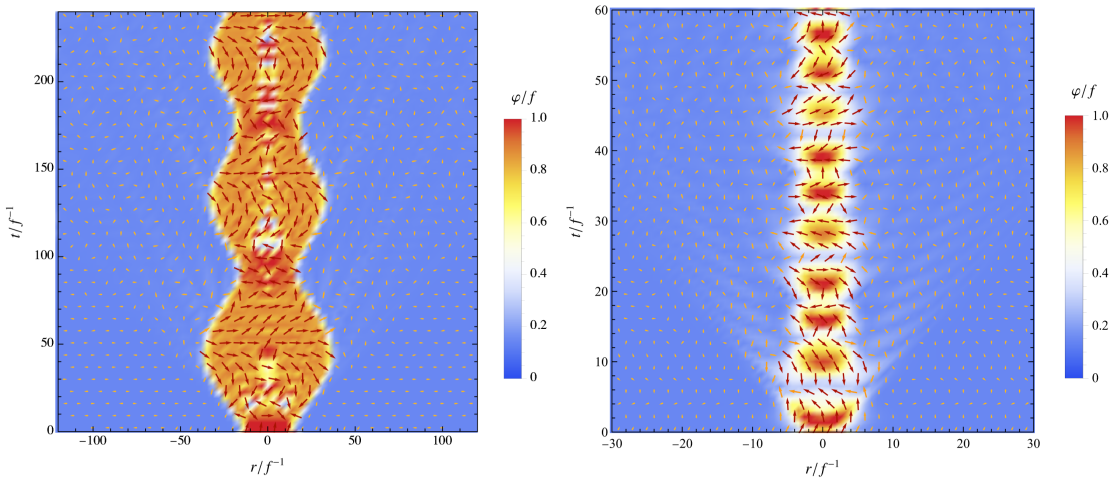

(a) (b)

Figure 2.6: Numerical simulations of the time-evolution of bubbles in the high frequency regime $\omega = 4\omega_c$ for different initial radii (a) $R_0 \simeq 13.2/f^{-1}$, (b) $R_0 \simeq 2.5/f^{-1}$. Clearly, the bubbles initially expand. Note the increased space-time domain of the simulation in panel (a).

2.13.5 Information horizon

Here we provide results of numerical simulations that illustrate the notion of an information horizon for a bubble in the semiclassical approximation. In the corresponding simulations, shown in Fig. 2.7, we consider a perturbation

$$p(r) = \exp\left[\frac{i\pi}{2}\frac{f(r)}{f(0)}\right] \tag{2.135}$$

of the initial r profile of θ. Here,

$$f(r) = \frac{1}{\sigma\sqrt{2\pi}} e^{-\frac{1}{2}(r/\sigma)^2} \tag{2.136}$$

is the probability density function of a normal distribution. The corresponding size of the perturbation is set by $\sigma \equiv 5/m \gg 1/m$.

That is, we obtain the new initial conditions from the old ones via the mapping $\Psi|_{t=0} \to \Psi|_{t=0} p(r)$ and $\partial_t \Psi|_{t=0} \to \partial_t \Psi|_{t=0} p(r)$. From the simulations we observe that both the total energy and the total $SU(N)$ charge are conserved throughout the evolution of the bubble. Furthermore, no waves are emitted, as opposed to in the case of the high frequency regime. We emphasize that the perturbation of θ remains within the bubble. Moreover, note that the profile of θ is not homogeneous in the interior of the bubble. This can be clearly seen when compared to the stabilized bubble in Fig. 2.3. Specifically, for a bubble with a perturbation of θ, the variations of θ within the bubble can be seen from the r-dependent directions of the vector arrows in Fig. 2.7.

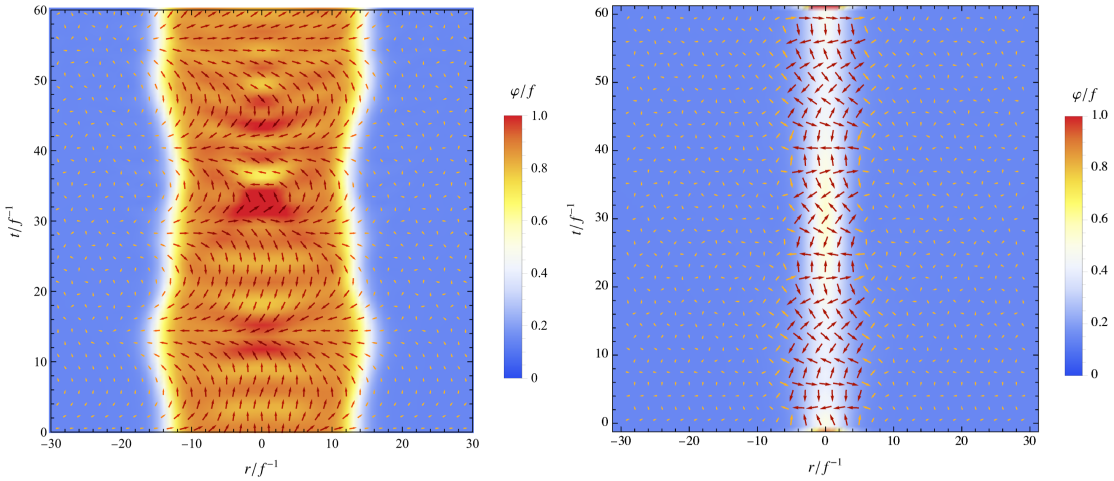

(a) (b)

Figure 2.7: Numerical simulations of the time-evolution of bubbles, with a perturbation of the r profile of θ, for different initial radii (a) $R_0 \simeq 13.2/f^{-1}$, (b) $R_0 \simeq 2.5/f^{-1}$. The perturbation of θ is contained within the bubble.

2.14 Correspondence to black holes

As argued in [22], we have verified the correspondence between black holes and generic saturons on the example of a saturated vacuum bubble. This connection is set up via the Goldstone coupling $G^{(\mathrm{P})}_{\mathrm{Gold}}$ of the Goldstone boson due to the spontaneously broken Poincaré symmetry. The similarities between the properties of a black hole in the theory of gravity and a saturon bubble of the $SU(N)$ theory become evident when these are expressed in terms of $G^{(\mathrm{P})}_{\mathrm{Gold}}$. The SSB of Poincaré symmetry by any self-sustained physical state is a generic phenomenon. Therefore, the corresponding coupling $G^{(\mathrm{P})}_{\mathrm{Gold}}$ is well defined in both theories. In the case of a black hole, $G^{(\mathrm{P})}_{\mathrm{Gold}}$ corresponds to Newton's gravitational constant G_{N}. Correspondingly, the decay constant f is equal to the Planck mass M_{P}. Thus, there is a direct correspondence between the properties of black holes and those of generic saturons. We summarize this correspondence in Table 2.2.

	Object	
Quantity	Saturons S	Black holes
S	$(fR)^2 = \alpha^{-1}$	$(RM_{\rm P})^2$
T	R^{-1}	R^{-1}
$t_{\rm min}$	$R^3 f^2 = SR$	$R^3 M_{\rm P}^2 = SR$

Table 2.2: Correspondence between characteristics of generic saturons and their specific realizations in gravity – black holes.

We can now apply the knowledge obtained from this correspondence to improve our understanding of black hole physics. First, note that the $1/S$, or equivalently $1/N$, corrections to the thermality of the radiation are crucial for the purification of the state and the retrieval of information from it. Correspondingly, the evaporation of a black hole cannot be self-similar. That is, although two black holes may appear identical in the semiclassical treatment, viewed from the perspective of the full quantum theory they are not. Furthermore, we conclude that during its evaporation, the black hole develops inner entanglement. This was previously discussed in [14,16,60]. We also clearly see the mechanism of the memory burden effect [30,35] at play. Specifically, a saturon bubble is stabilized by the quantum information it contains.

The above findings provide further compelling evidence that a black hole is a saturated bound state of soft gravitons, as proposed by the quantum N-portrait [14]. Moreover, this is supported by the fact that the characteristics of both black holes and generic saturons can be described using the trans-theoretic notion of the Poincaré Goldstone. The graviton and the Poincaré Goldstone have one common fundamental property: Both couple to everything that possesses energy-momentum. For a black hole, the above two are the same. In other words, the collective excitations of the graviton "condensate" give rise to the Goldstone boson of the Poincaré symmetry.

A further important aspect of the correspondence of black hole physics and saturons is that of the information horizon in the semiclassical limit. For the $SU(N)$-symmetric theory discussed here, this limit is given by Eq. (2.93). As demonstrated above, a saturon bubble possesses an information horizon in this limit. Let us compare the information horizon of a saturated vacuum bubble to the black hole horizon.

The information horizon of a saturon bubble prohibits the transmission of the information, which is contained within it in terms of the occupation numbers of the Goldstone modes, to an outside observer. This is due to the fact that the collective coupling $\lambda_{\rm t} = \alpha N$ completely dominates the scattering process, while the exchange of the individual Goldstone occupation numbers is additionally suppressed by powers of $1/N$, resulting in a vanishing rate.

The main distinction of this horizon to that of a black hole is that in the latter case any sort of particle cannot escape into the exterior. This difference arises because of the aforementioned universality of gravitational interaction.

Contrarily, the horizon of saturons in nongravitational theories is less limiting. This

is because the universality of the Goldstone coupling is limited by the Goldstone theorem only to the quanta that carry the $SU(N)$ charge. Therefore, only particles carrying an $SU(N)$ charge are restricted by the information horizon.

Nevertheless, this distinction indicates a universal phenomenon. That is, the above connection becomes clearer if the notion of the horizon is addressed from the perspective of the quantum numbers of the information-storing modes contained in a saturon. For a black hole, the information-storing agents are likely the different energy-momentum excitations of the graviton modes. These quantum numbers source gravity. That is, any quantum that has energy-momentum can carry information. The black hole horizon prohibits the escape of such quanta into the exterior.

Similarly, an $SU(N)$ saturated bubble possesses an horizon for the quanta that carry $SU(N)$ charge. These information carriers correspond to nontrivial representations of $SU(N)$. We conclude that, formulated in terms of the quanta that carry information, the similarity between the horizon of a black hole and that of an $SU(N)$ saturon becomes very clear.

Note that the saturon bubble is stable in the fully classical limit of vanishing Planck constant $\hbar$. We can see this from the expression of the decay rate in Eq. (2.101), which is proportional to $\hbar$. Recall that in our quantum calculations we have set $\hbar = 1$. However, in a classical calculation for a saturon of finite mass, $\hbar = 0$ holds and therefore Γ_{decay} vanishes. This is in one-to-one correspondence with a black hole which also becomes stable in the classical limit.

One may ask whether saturons possess an analogue of the singularity in the case of black holes. The saturons discussed here are solitonic objects, which are given by smooth solutions in the semiclassical limit of Eq. (2.93). Note, however, that in this limit the radius R is finite, while the expectation value at the origin f is infinite. Therefore, the radial gradient of the field becomes infinite as well. We can see this infinite field gradient as being similar to a singularity, although locally the field profile is smooth for any finite f. The correspondence of this type of singularity with that of a semiclassical black hole still needs to be thoroughly studied.

Nevertheless, we can argue that the black hole singularity is usually considered to be a feature of the semiclassical regime alone, and this issue is assumed to be solved within a fully quantum framework. From this point of view, formally, the results presented here can be seen as a form of such a solution. That is, the singularity is present in the semiclassical limit of Eq. (2.93), but is absent in the quantum theory for finite N. Nevertheless, again, whether this is only a superficial analogy or of fundamental physical significance still needs to be studied.

We now comment on the predicted observational phenomena regarding black hole physics. As stated previously, the correspondence between black holes and generic saturons allows us to predict new phenomena for black holes. The $1/S$ corrections to the thermality of the emitted radiation are one such phenomenon. In the semiclassical limit of Eq. (2.93) we have $S \to \infty$, and therefore these non-thermal corrections vanish. However, for a finite S, these corrections have a significant effect over timescales comparable to the black hole's half-decay time, which is proportional to S.

Consequently, deviations from the semiclassical approximation are easier to observe for black holes that are old and closer to their half-life time. Large astrophysical black holes are unfortunately too young to exhibit such departures from the semiclassical regime. However, for primordial black holes of small mass, under the condition that these exist, such effects may be within an observable window [35]. Let us note that vorticity is another recently proposed [26] observational phenomenon for rotating black holes.

Another natural direction of research is the realization of entropy-saturated systems in laboratory experiments. One specific example could be the study of nonrelativistic saturated many-body systems of the type [29, 34] in experiments with ultracold bosons with attractive interactions.

Investigating saturation in various laboratory analogs of black holes also appears promising. Examples of such attempts include realizations based on sound propagation in fluids [71–73], black hole analogs for photon systems [74–76], and dielectrics [77]. Hawking-like radiation within analogue systems has been discussed in [78, 79].

The realization of saturated systems in many-body experiments could also provide a new perspective for the investigation of black hole analogs.

2.15 Summary and discussion

In this chapter we provided further evidence for the following ideas suggested in [22]: First, the entropy of a self-sustained field-theoretic object obeys the bounds in Eqs. (2.1) and (2.2), which arise due to the saturation of the unitarity bound of the corresponding theory. Second, these entropy-saturating objects, called saturons, possess the same characteristics as black holes. The overview of this correspondence is given in Table 2.2. Various other works have also discussed this connection [20, 21, 23, 25, 27]. The work contained in this chapter provides a further advancement of this general framework.

Furthermore, we have observed explicitly that the memory burden effect [30, 35] plays a significant role in the time evolution of systems that possess an enhanced capacity to store information. This is a universal phenomenon for such systems. In short, via this phenomenon, the quantum information stored within a system is able to stabilize it. Previous works have suggested that also black holes are so long-lived because of this universal phenomenon. Here we have illustrated this effect on a specific example of a saturon within an $SU(N)$-symmetric theory.

We have analyzed the black hole–saturon correspondence both analytically and numerically for a concrete model, initially discussed in [22]. The corresponding theory is renormalizable, and possesses a global $SU(N)$ symmetry and a coupling α. In our analysis, we took α as arbitrarily small, while scaling N accordingly to keep their product, αN, finite. The theory possesses a set of degenerate vacua. The $SU(N)$ symmetry is spontaneously broken in these vacua to various maximal subgroups. We considered bubbles of the $SU(N-1) \times U(1)$ vacuum inside an asymptotic $SU(N)$-symmetric vacuum. The bubble contains $N_{\text{Gold}} \sim N$ Goldstone flavors due to the spontaneous symmetry breaking.

We have demonstrated that a tower of stationary bubbles is contained within the spec-

trum of the theory. From a quantum viewpoint, the bubble is a bound state of Goldstone modes with a total occupation number N_G. The bubble configurations that have the least energy cost to contain a given $SU(N)$ charge are classically stable. This stability can be seen as a particular realization of the memory burden effect. That is, the bubble is stable because of the quantum information stored in terms of the occupation numbers of the Goldstone modes within it. Due to the nonzero energy gap outside of the bubble, the energy cost of a state containing the quantum information in the exterior vacuum would greatly exceed the energy cost to store this information within the bubble.

The stabilized bubbles considered here can be seen as a generalization of nontopological solitons, or Q-balls [67, 68]. The key significant property of the saturon bubble is its high microstate entropy. This entropy is carried by the Goldstone modes, which are contained in the interior of the bubble. We note that a different version of a high-entropy Q-ball is studied in [80]. When the theory saturates the bound on unitarity, the entropy of the bubble reaches the limit given by Eq. (2.1), or equivalently by Eq. (2.2). A bubble that is saturated possesses the key characteristics of a black hole. Specifically, its entropy obeys the area-law, in the semiclassical limit the bubble exhibits an information horizon and evaporates at a thermal rate with a temperature $T \sim 1/R$, and the timescale of information recovery is similar to the Page time. Written in terms of the universal quantities G_{Gold} or α_G, the above properties have the same corresponding expressions for a black hole and a saturated bubble.

Near the saturation point, the vacuum bubbles of the present $(3 + 1)$-dimensional $SU(N)$ theory are similar to the saturated bound states [25] of the $(1 + 1)$-dimensional Gross-Neveu theory [61]. The underlying reason for this is the trans-theoretic phenomenon of unitarity saturation.

Additionally, there is a correlation between the degree to which the memory burden is quantum and the entropy saturation. Regarding the stability of the bubble, only the total Goldstone occupation number N_G is relevant. That is, the memory burden effect, and therefore the stability of the bubble, depend on N_G alone and are indifferent to its specific distribution among the different Goldstone flavors. Specifically, in view of the bubble stability alone, occupying a single Goldstone mode macroscopically is equivalent to occupying multiple Goldstone modes microscopically.

When the total occupation number N_G exceeds the number of Goldstone flavors N_{Gold}, the corresponding memory burden can be described classically. This is due to the fact that for $N_G \gg N_{\text{Gold}}$ some of the modes have to be macroscopically occupied. Bubbles that are stabilized in this way possess an entropy that is much less than the entropy bounds of Eqs. (2.1) and (2.2). In other words, vacuum bubbles that are stable due to a classical memory burden effect represent undersaturated bound states.

Contrarily, bubbles with $N_G \sim N_{\text{Gold}}$ are able to saturate the bounds of Eqs. (2.1) and (2.2). These bubbles form a multiplet under the $SU(N)$ symmetry, in which the bubbles stabilized by classical memory burden and those that are stable due to a quantum memory burden are fully degenerate.

The results presented here can be generalized to constructions within theories with other symmetries and field content. For example, the group $SO(N)$ with a symmetric

representation is very similar to the model discussed here. Additionally, one can consider supersymmetric extensions of the present model.

For all known examples of saturons, the occupation number of their quanta, their inverse couplings and their entropy are all of the same order. Consequently, the black hole–saturon correspondence provides evidence for a composite view of a black hole [14, 16, 60]. In this picture, a black hole corresponds to a bound state of N weakly interacting soft gravitons. Clearly, this is analogous to the saturated bound state of N Goldstones within the $SU(N)$ theory discussed here. There is a direct correspondence between the black hole characteristics proposed by the quantum N-portrait [14] and the characteristics of saturon bubbles of the present $SU(N)$ theory. Specifically, the quantum information is contained in the $1/S$ deviations from a thermal radiation spectrum. These deviations lead to an information recovery timescale of Eq. (2.114).

The above correspondence provides further evidence for the presence of the memory burden effect in black holes. Additionally, there is compelling evidence that black holes do not evaporate self-similarly.

Chapter 3

Fast Prescramblers

In this chapter we discuss the process of diffusion or "prescrambling" of information in a quantum system, based on the work in [2]. We define a measure for this spreading of the system's state in terms of a minimum probability threshold for the states in the Hilbert space. We demonstrate our findings within the framework of a specific prototype model with enhanced memory capacity. We conjecture: (1) The fastest prescramblers require a time logarithmic in the number of degrees of freedom. (2) The investigated enhanced memory capacity model is a fast prescrambler. (3) (Fast) prescrambling occurs not later than (fast) scrambling. (4) Fast scramblers are fast prescramblers. (5) Black holes are fast prescramblers.

3.1 Introduction

3.1.1 Scrambling

First, as an introduction, we recapitulate and elaborate upon the phenomenon of scrambling. Consider a physical quantum system of K degrees of freedom that carry information. The system is prepared in a pure state, which transforms under unitary time-evolution. Therefore, the state of the system remains pure throughout. However, over time, the system thermalizes in the following sense: Although the time-evolution is unitary, the initial state gradually becomes increasingly entangled with the other states within the Hilbert space. The information originally carried only by the initial state becomes more and more spread over the other states. That is, the system mixes up, or "scrambles" [36, 37] the information. We call *scrambling time* t_{s} [36,37] the timescale on which this process occurs.

Let us now review the definition of scrambling. For this we follow the works of [36–38], which introduced the notion of scrambling. We refer to a system as *scrambled* if its state, or equivalently the information contained within it, is sufficiently distributed over the entire Hilbert space according to some chosen measure.

We emphasize two important aspects of this definition: First, scrambling requires the state to be spread over the entire state space of the system. Second, the definition of the

scrambling measure is deliberately kept general. The latter aspect allows us to apply our findings to a large set of specific measures. Multiple distinct formulations of such measures are defined in the literature. We provide a brief overview of several of these. One of the first definitions of a scrambling measure is the Haar measure in relation to the choice of the mixing unitary transformation [36]. This measure has also been applied to states and dubbed "Haar-scrambling" in [37]. Another measure of scrambling in [37] concerns a model of K qubits, following the work of [39]. For this scrambling measure, a system is said to be "Page-scrambled" if the entanglement entropy of any subsystem of $n < K/2$ qubits equals $S_n = n - O(\exp[2n - K])$. Ultimately, to be able to explain scrambling at the fundamental quantum level, especially in the case of black holes, a microscopic framework is necessary. Such a picture was suggested in a series of works including [14, 16, 40–42]. In particular, this framework proposes the notion of "memory modes". We review this concept below. Additionally, these works consider "one-particle entanglement" [41] and "maximal entanglement" [42] and the corresponding timescales in application to microscopic models of black holes.

Here we consider a new regime. This regime applies on timescales smaller than those of the various scrambling measures above. That is, we define and quantify a new pre-scrambling stage during the time evolution of a system. We emphasize that the findings presented here are independent of a specific definition of the scrambling measure.

Having reviewed the definition of scrambling, we can now discuss the corresponding scrambling time. As suggested by [36–38], the fastest scramblers require a time logarithmic in the number of degrees of freedom. These are commonly referred to as *fast scramblers*. We generalize the number of degrees of freedom in the above definition to the number of generic quantum labels, such as modes or sites. Additionally, to be as general as possible, we do not consider a specific temperature dependence of scrambling, or any bound on the scrambling time due to the temperature of the system, such as those discussed in [37, 81–83] as well as in other works. We emphasize that the findings presented here are valid for a general definition of scrambling, with the only condition that the scrambling time of fast scramblers scales logarithmically with the number of its degrees of freedom K. We consider the temperature dependent scrambling time for the prototype model in Sec. 3.2 in a separate work [84]. Here, instead, the study this model at timescales before its scrambling time.

3.1.2 Enhanced memory capacity

Here we review the notion of "enhanced memory capacity" and the concepts related to it, mostly relying on [35]. Systems that can accommodate states of a high capacity to store information are studied as part of a larger program of [1, 14, 16, 20–27, 29–35, 40, 85, 86]. Such systems are referred to as those with *enhanced memory capacity* [16, 20–22, 29–35, 40, 85, 86]. The introduction of this concept was motivated by the goal to create a prototype mechanism to model the information storing and processing properties of black holes, in correspondence to the black hole's quantum N-portrait [14]. One universal feature of systems with enhanced memory capacity is that of "memory burden" [30, 33].

To illustrate this effect, we consider a quantum system of K degrees of freedom. These are commonly described as quantum oscillators. We can therefore label the states of the system by the different sequences $|n_1, \ldots, n_K\rangle$ of the occupation numbers of the K oscillators. Each such sequence constitutes a *memory pattern* that carries the information. The memory capacity of the system corresponds to the number of distinct such states that are degenerate in energy and can therefore be stored within a narrow energy gap [32, 34]. The microstate entropy of n_{st}-many such degenerate states corresponding to distinct patterns is given by $S = \ln(n_{\text{st}})$. Via the *memory burden* effect [30, 33], an information pattern that stores a large amount of quantum information stabilizes the system and prevents it from departing from an enhanced memory capacity state.

A system can attain a state of enhanced memory capacity via the effect of *assisted gaplessness* [34]. This can be achieved by introducing an additional highly occupied *master mode* into the system. This master mode interacts attractively with the set of information-storing *memory modes*. This results in smaller energy gaps for the memory modes, and consequently, lower energy costs for storing large amounts of information in terms of the excitations of those modes. Consequently, due to the memory burden effect, the memory modes backreact on the master mode impeding the change of its occupation number, thus preventing the system from departing from the state of an enhanced memory capacity. It has been suggested in [30] and further studied in [35], that the effect of memory burden can be avoided by introducing an additional set of memory modes K' into the system. The system can then transfer the information-storing memory patterns from the K modes to the new K' modes, thus allowing the master mode to evade the memory burden effect. We recapitulate the corresponding details below.

3.2 A prototype model

As discussed above, memory burden can be alleviated by including a second set of modes K' into the system. We consider such a prototype model with enhanced memory capacity given in Eq. (34) of [35]. The Hamiltonian of this model is reproduced in Eq. (3.6) with minor notation changes. The model possesses two sets of bosonic memory modes K and K'. The corresponding creation and annihilation operators $\hat{a}_k^\dagger, \hat{a}_k$ and $\hat{a}_{k'}^\dagger, \hat{a}_{k'}$ obey the standard commutation relations

$$\left[\hat{a}_{j^{(\prime)}}, \hat{a}_{k^{(\prime)}}^\dagger\right] = \delta_{j^{(\prime)}k^{(\prime)}}, \quad \left[\hat{a}_{j^{(\prime)}}, \hat{a}_{k^{(\prime)}}\right] = 0, \quad \left[\hat{a}_{j^{(\prime)}}^\dagger, \hat{a}_{k^{(\prime)}}^\dagger\right] = 0 \tag{3.1}$$

for $j^{(\prime)}, k^{(\prime)} = 1, \ldots, K^{(\prime)}$. The occupation number operators corresponding to these are given by $\hat{n}_{k^{(\prime)}} = \hat{a}_{k^{(\prime)}}^\dagger \hat{a}_{k^{(\prime)}}$. The eigenvalues and the eigenstates of the occupation number operators are given by $n_{k^{(\prime)}}$ and $|n_{k^{(\prime)}}\rangle$, respectively. The interaction strength among the memory modes $\hat{n}_{k^{(\prime)}}$ is controlled by the coupling C_m. The model contains two more bosonic modes $\hat{n}_a$ and $\hat{n}_b$ with creation and annihilation operators $\hat{a}^\dagger$, $\hat{a}$ and $\hat{b}^\dagger$, $\hat{b}$, respectively. These satisfy commutation relations analogous to those in Eq. (3.1). The corresponding exchange of occupation number is parametrized by the coupling C_b. We refer to the mode $\hat{n}_a$ as the *master mode*.

The distinction in the effective energy gaps

$$\varepsilon_k \equiv \varepsilon\left(1-\frac{n_a}{N}\right) \quad \text{and} \quad \varepsilon_{k'} \equiv \varepsilon\left(1-\frac{n_a}{N-\Delta}\right) \tag{3.2}$$

of the $\hat{n}_k$ and $\hat{n}_{k'}$ modes, respectively, is set by Δ. Note that the modes of the K and K' sectors become effectively gapless for $n_a = N$ and $n_a = N-\Delta$, respectively. That is, in the initial state of the system, given by Eq. (3.5), $n_a = N$ and the K modes are gapless, while the K' modes have a finite nonzero gap. Initially, the K memory modes contain the entire information, while the K' modes are empty. Now, as n_a evolves and departs from N, a state where $n_a = N-\Delta$, $n_b = \Delta$ and the K' modes store the quantum information becomes energetically available. Thus, the memory patterns are transferred to the K' sector, and memory burden is avoided.

The total occupation number of the two memory sectors is conserved and is given by

$$N_m \equiv \sum_{k=1}^{K} n_k + \sum_{k'=1}^{K'} n_{k'}. \tag{3.3}$$

As in [35], all modes within the memory sectors are truncated to qubits. The various states of the system are denoted by

$$|n_a, n_b, n_1, \ldots, n_K, n_{1'}, \ldots, n_{K'}\rangle \equiv |n_a\rangle \otimes |n_b\rangle \bigotimes_{k=1}^{K} |n_k\rangle \bigotimes_{k'=1}^{K'} |n_{k'}\rangle\,. \tag{3.4}$$

The system is evolved from an initial state

$$|\text{in}\rangle = |\underbrace{N}_{a}, \underbrace{0}_{b}, \underbrace{\overbrace{1,\ldots,1}^{=N_m},0,\ldots,0}_{K}, \underbrace{0,\ldots,0}_{K'}\rangle \tag{3.5}$$

where the $\hat{n}_a$ and $\hat{n}_b$ modes are occupied by N and 0, respectively, and only the first N_m modes of the K sector contain one particle each. As in [35], the basic energy unit is set to unity, $e \equiv 1$. The Hamiltonian of the model then reads

$$\begin{aligned}\hat{H} = {} & \varepsilon\left(1-\frac{\hat{n}_a}{N}\right)\sum_{k=1}^{K}\hat{n}_k + \varepsilon\left(1-\frac{\hat{n}_a}{N-\Delta}\right)\sum_{k'=1}^{K'}\hat{n}_{k'} + C_b\left(\hat{a}^\dagger\hat{b} + \text{H.c.}\right) + \\ & + C_m\left\{\sum_{k=1}^{K}\sum_{k'=1}^{K'} f_1(k,k')\left(\hat{a}_k^\dagger\hat{a}_{k'} + \text{H.c.}\right) + \sum_{k=1}^{K}\sum_{l=k+1}^{K} f_2(k,l)\left(\hat{a}_k^\dagger\hat{a}_l + \text{H.c.}\right) + \right. \\ & \left. + \sum_{k'=1}^{K'}\sum_{l'=k'+1}^{K'} f_3(k',l')\left(\hat{a}_{k'}^\dagger\hat{a}_{l'} + \text{H.c.}\right)\right\},\end{aligned} \tag{3.6}$$

with

$$f_i(k,l) = \begin{cases} F_i(k,l) - 1\,, & F_i(k,l) < 0.5 \\ F_i(k,l)\,, & F_i(k,l) \geq 0.5 \end{cases} \tag{3.7}$$

and

$$F_i(k,l) = \left(\sqrt{2}(k+\Delta k_i)^3 + \sqrt{7}(l+\Delta l_i)^5\right) \mod 1, \tag{3.8}$$

where

$$\Delta k_1 = \Delta k_2 = 1, \quad \Delta k_3 = K+1, \quad \Delta l_1 = \Delta l_3 = K+1, \quad \Delta l_2 = 1. \tag{3.9}$$

This makes the individual couplings among the memory modes essentially random.

In the case of a spherically symmetric system, specifically a static black hole, we can label its quantum states by the quantum numbers (l,m) of the spherical harmonics $Y_l^m(\theta,\phi)$. We can thus determine the free energy gap ε of the corresponding memory modes [35]. In particular, we can estimate the energy of the highest mode and therefore also the value of ε from the number of independent solutions for one degree l of a given spherical harmonic $Y_l^m(\theta,\phi)$ as [35]

$$\varepsilon = \sqrt{K}. \tag{3.10}$$

The memory modes should remain effectively gapless, which imposes the following constraints on the couplings [35]

$$C_b \lesssim \frac{1}{\sqrt{N}}, \quad C_m \lesssim \frac{1}{\sqrt{N_m}\sqrt{K}}. \tag{3.11}$$

Following [35], we set

$$K = K'. \tag{3.12}$$

Finally, the condition that close to the initial state in Eq. (3.5) the K' memory sector is not gapless provides the constraint $|\varepsilon_{k'}| \gg 1/\sqrt{N_m}$ [35], which can also be expressed as a constraint on Δ as

$$\Delta \gg \frac{N}{1+\sqrt{N_m}\sqrt{K}}. \tag{3.13}$$

Since the numerical simulations require a considerable time to complete, for the majority of our numerical analysis we pick a value of Δ that does not satisfy this constraint. However, first, from the scan over the parameter Δ we are able to observe a clear dependence of the analyzed quantities over the majority of the Δ-range. Second, one of the two considered quantities changes its Δ-dependence only when Δ is very close to N. We are therefore left with a set of six free and constrained parameters

$$N, K, N_m, \Delta, C_b, C_m. \tag{3.14}$$

Within the framework of the quantum N-portrait [14] of a black hole of entropy $S \gg 1$, the parameter space is constrained to $N = S$, $K = S$, $N_m = S/2$ [35]. We consider this scaling in Sec. 3.4.2.

3.3 Two effects

As mentioned previously, a microscopic framework of scrambling was developed in [40–42, 60, 85–91], based on the quantum N-portrait of a black hole [14]. For a precise and

consistent definition of scrambling, a specific measure of the uniformity of the distribution of the state needs to be chosen. Nevertheless, as discussed above, our results are general and do not depend on a particular definition of the measure. The only requirement we demand is that the state of a scrambled system is sufficiently distributed over the *entire* state space. This is a general property of all definitions of scrambling. Correspondingly, there are two effects that we expect to occur before the system is scrambled:

(1) The wave function of the system $|\psi(t)\rangle$, originally in a single basis state $|\text{in}\rangle$, diffuses over the entire particle basis $\{|v_i\rangle\}$, given a minimum state probability threshold.

(2) The most probable state that the system can assume, changes from $|\text{in}\rangle$ to another basis state $|v_i\rangle \neq |\text{in}\rangle$.

Les us quantify these effects and the corresponding times. On a finite, nonzero timescale, $|\psi(t)\rangle$ spreads over the entire basis $\{|v_i\rangle\}$, with the probability $|C_i|^2 = |\langle\psi(t)|v_i\rangle|^2$ of each state rounded to a finite, fixed and sufficiently small precision $p < 1/\dim(\{|v_i\rangle\})$. For a given value of p, we denote by f the fraction of the basis that $|\psi(t)\rangle$ spreads over, and by t_f the earliest time for which $f = 1$ holds. Specifically, we define

$$f \equiv \frac{1}{\mathcal{N}} \sum_{i=1}^{\mathcal{N}} H(|C_i|^2 - p) \ , \quad H(x) = \begin{cases} 0, & x \leq 0 \\ 1, & x > 0 \end{cases} . \tag{3.15}$$

Here, $\mathcal{N} \equiv \dim(\{|v_i\rangle\})$ is the number of basis states, or equivalently the dimension of the Hilbert space, and $H(x)$ is the left-continuous Heaviside step function. Evidently, for the system in Eq. (3.6), p is nonzero as soon as the system starts evolving. In other words, $|\psi(t)\rangle$ spreads essentially instantaneously over the whole basis, but with minuscule contributions of most of the states. Nevertheless, at the time t_f, all of the corresponding states probabilities have a value $> p$.

In addition, we denote the time when the most probable state of the system changes from $|\text{in}\rangle$ to a different basis state $|v_i\rangle \neq |\text{in}\rangle$ by t_c. That is, t_c is the earliest time for which $\max_i(|C_i|^2) \neq |C_{\text{in}}|^2$ holds.

We study the above two effects for the system of Eq. (3.6) in Sec. 3.4. Our primary objective is to investigate the dependence of the times t_f and t_c on the parameters in Eq. (3.14). We emphasize that the definitions of the above two effects of spreading of the state of the system include quantitative measures of the distribution of the state in terms of probabilities. Therefore, our definitions are different from those of the diffusion discussed in [38]. In addition, our definitions are also different from that of *minimal scrambling* in [42], which, for a system of N qubits, is defined as the state of the system reaching a uniform superposition of N basis states, each with $1/N$ probability. Note that this is different to a superposition over all 2^N basis states.

3.4 Numerical results

We expect the system to exhibit the following behavior during its time-evolution: Initially, for the state $|\text{in}\rangle$, we have $f = 1/\mathcal{N}$ and $\max_i(|C_i|^2) = |C_{\text{in}}|^2$. With the system

evolving in time, the master mode will gradually transfer its occupation number n_a to that of the $\hat{b}$ mode. Therefore, as n_a departs from N, a state in which the K' modes store the quantum information becomes energetically available. Correspondingly, the occupation number of the memory modes is gradually transferred from the K sector to the K' sector. Thus, the system explores increasingly larger portions of the Hilbert space. Correspondingly, f will increase until reaching unity at the time t_f. In other words, the state of the system is diffused over the entire state space with a probability $|C_i|^2 > p$ of each basis state i for a chosen value of p. In addition, we expect the state corresponding to $\max_i(|C_i|^2)$ to change from $|\text{in}\rangle$ to a different state at the time t_c. Our goal is to understand how the timescales t_f and t_c scale with the parameters of the model.

By our definition of t_f, specifically because of the condition for the state to diffuse over the entire Hilbert space, we expect t_f to obey an upper logarithmic bound for N, K and N_m. We expect this for the following reasons: The model given by Eq. (3.6) is designed to simulate the information-processing characteristics of a black hole. At the same time, black holes are conjectured to be the fastest scramblers [36,37]. Moreover, the fastest scramblers are conjectured to scramble information on timescales that are logarithmic in the number of their degrees of freedom [36,37]. According to all definitions of scrambling, the information within a system is scrambled when its state is sufficiently spread over the entire Hilbert space. Therefore, before a system is truly scrambled by any scrambling measure, we expect the state of the system to become distributed over the entire Hilbert space with a minimal probability of each of the basis states. We call this process "prescrambling".

This provides us with a tool to test whether the prototype model in Eq. (3.6) complies with the conjectures of [36, 37] at the level of prescrambling. This would be fulfilled if $t_f \leq t_s \sim \ln(\#\text{ d.o.f.s})$. We investigate this numerically below.

We perform our simulations using QuSpin [92–94]. Unless otherwise stated, and except for the parameter(s) varied, the values of the parameters are given by

$$p = 5 \cdot 10^{-21}, \quad N = 4, \quad K = 4, \quad N_m = 2, \quad \Delta = 1, \quad C_b = 0.1, \quad C_m = 0.1. \tag{3.16}$$

Constraining our baseline parameter choice to these values, we thus adopt the quantum N-portrait scaling regime of a black hole: $N = S$, $K = S$, $N_m = S/2$. From the basis of this choice we analyze the individual parameter scaling outside of this regime. Note that as the model in Eq. (3.6) was proposed to capture how a black hole processes and stores information, the scaling regime of black hole's quantum N-portrait is the one of significance. The Hilbert space of the system grows rapidly with an increase in the above parameters. We therefore restrict their values to the choice $N = 4$, $K = 4$, $N_m = 2$. This allows us to scale the individual parameters over a greater domain, which in its own turn provides a better insight into the large-value scaling limit of each of the parameters.

In our simulations we constrain the values of C_b and C_m to satisfy the bounds in Eq. (3.11). For the value of p in Eq. (3.16), we round each $|C_i|^2$ to 20 decimal places and include its contribution in f. The precision p has such a small value because for sufficiently large values of N and/or K, t_f begins to diverge from its logarithmic behavior and starts increasing more rapidly. Nevertheless, for an arbitrary but fixed range of N and/or K we

expect a sufficiently small value of p to exist, such that t_f scales logarithmically for that range. We show an exemplary plot of the two effects and their corresponding timescales for these parameter values in Fig. 3.1.

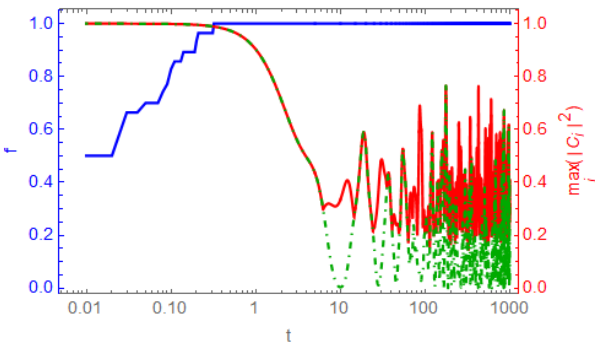

Figure 3.1: Left (blue): Fraction f of Hilbert space that the state of the system is spread over with a contribution $p > 5 \cdot 10^{-21}$ of each state. The corresponding basis has 140 states. Right (red): Maximum probability $|C_i|^2$ of any single basis state $|v_i\rangle$ with $i \in [1, 140]$, and (green, dot-dashed): Probability of the initial state $|C_{\text{in}}|^2$. The time step of the simulation is 10^{-2}. Note that the timescale is logarithmic. For this example we obtain $t_f = 0.32$ and $t_c = 6.25$.

We observe in a few of our simulations that the value of f, after reaching unity, temporarily decreases back below 1, but then increases to 1 again before remaining at this value. However, in the majority of our simulations, once f reaches unity, it tends to stay at that value. The effect of a temporary decrease in f occurs as the system may sometimes predominantly occupy only a fraction of the states in the Hilbert space for a limited duration. That is, the system can be temporarily found in a superposition of only a subset of the states, before again becoming more diffused. However, we have more commonly observed that the diffusion of the state occurs in a continuous and increasing manner. Similarly, as depicted in Fig. 3.1, we find that $\max_i(|C_i|^2)$ may also come back to being equal to $|C_{\text{in}}|^2$ after a departure from it. However, this return is nonpermanent. Finally, we note that t_f does not always precede t_c. This is evident as f depends on the particular choice of p.

From our numerical analysis we expect large N, K and N_m, that is large systems with large sizes of the corresponding state spaces, to slow down the spread of the wave function $|\psi(t)\rangle$. Likewise, for a large difference in the energy gaps of the memory modes, parametrized by Δ, and for weak coupling strengths C_b and C_m, we expect the same to occur. In our simulations we want to first, verify, and second, quantify the corresponding parameter scalings. Let us emphasize that the diffusion of the state as defined previously in terms of f is expected to be an important precondition for scrambling. This is due to the fact that, clearly, before a state of a quantum system becomes scrambled over the entire Hilbert space with respect to some measure by any definition of scrambling, it needs to

first spread over the entire Hilbert space with a nonzero contribution of every basis state. Moreover, note that every mode in the system of Eq. (3.6) is directly coupled to every other mode of the corresponding sector(s). We therefore expect there to be no "diffusers" or "prescramblers" that are faster than this system. Below we study how fast this "fast prescrambler" is.

3.4.1 Individual parameter scaling

In this part of our analysis we vary the parameters individually. The results are depicted in Fig. 3.2, along with the corresponding best obtained fit functions. For compactness, only the general scaling is presented in the individual panels of Fig. (3.2). The detailed scaling with the corresponding fit parameters is listed in Table A.1 in the Appendix. In the simulations we are able to verify that large values of N, K, N_m and Δ, and small values of C_b and C_m slow down the spreading in terms of t_f. Furthermore, we find the quantitative dependence of t_f and t_c on the parameters of the model. However, let us note that we were unable to extract the dependence of t_c on N_m because of the irregularity of the data. Additionally, we remark that for the scaling of t_f with N_m the standard errors of the free fit-model parameters are of the same order as the values of the parameters themselves. Consequently, we cannot assume this to be a good fit for the obtained data. To be able to find a conclusive scaling of t_f with N_m, more data is needed. As N_m is the most costly of all parameters in view of the simulation run-time, this dependence remains to be studied.

Nevertheless, for larger values of N_m we expect t_f to grow as $\ln(N_m)$ for the following two reasons: First, we observe that t_f does not scale logarithmically also for small N. Instead, the logarithmic scaling emerges only for larger N. Second, only the parameters N, K and N_m determine the dimension of the Hilbert space of the system. We expect the size of this state space to be the property determining how quickly the wave function spreads. Consequently, this sets the scaling of t_f, and we expect it to depend on N, K and N_m in the same way.

We find a clear dependence of t_f and t_c on all of the other parameters of the model. Our most significant observation is the scaling

$$t_f \sim \ln(K). \tag{3.17}$$

In other words, given a fixed p, the time t_f that the system requires to diffuse the initial state over the entire Hilbert space $\{|v_i\rangle\}$ with a probability $|C_i|^2 > p \; \forall \; i \in [1, \mathcal{N}]$ increases logarithmically with the number of memory modes K. Note that the model in Eq. (3.6) has all-to-all couplings among the modes of each sector. Therefore, we expect the "diffusion" or "prescrambling" of Eq. (3.17) to be the most rapid for any physical system.

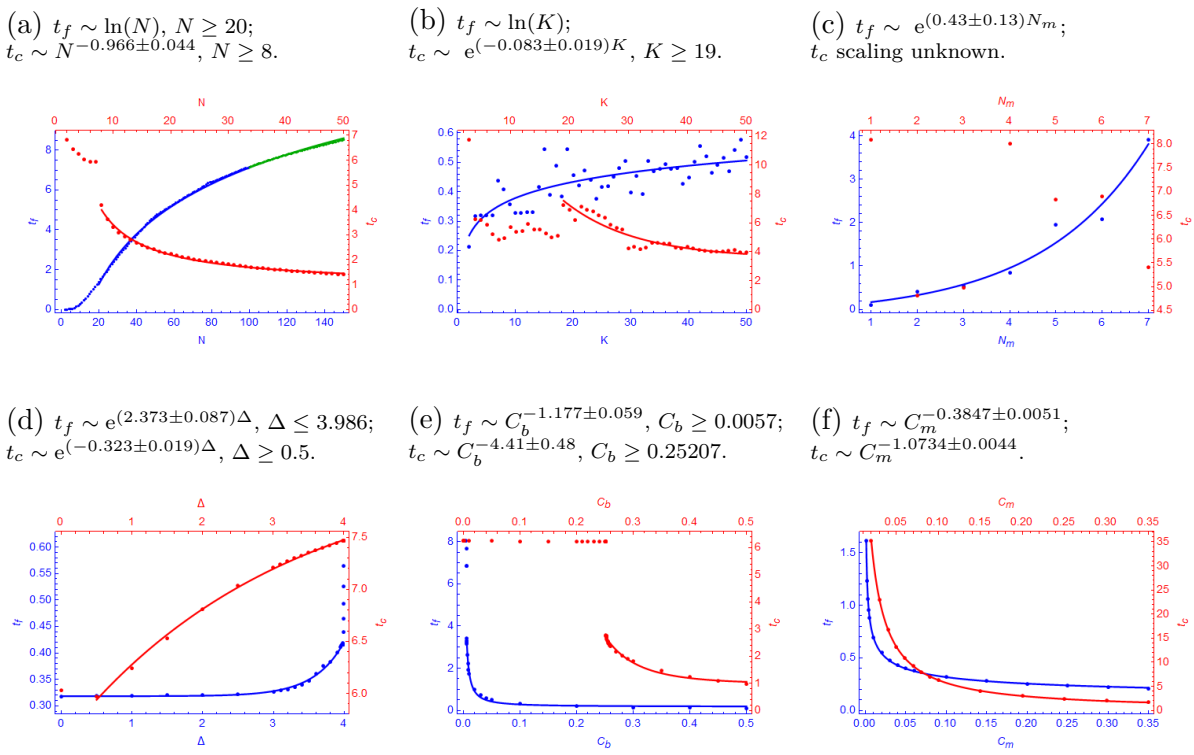

Figure 3.2: The general scaling of t_f and t_c with the individual parameters N, K, N_m, Δ, C_b, and C_m. The numerical data is shown as points, with the corresponding fits represented by solid lines. The dependence of t_f on the individual parameters is shown in blue (left and bottom axes), and that of t_c is shown in red (right and top axes). Note the different ranges of the axes. In addition to the scaling of the individual parameters, the parameters changed from the baseline choice of Eq. (3.16) are: Panel (a) for only the t_f scan: $p = 5 \cdot 10^{-41}$, also, N is scanned over up to 150 for a better fit; the permitted range is $N \leq 100$, see Eq. (3.11). The points for $N \in [101, 150]$ and the respective fit are marked green. Panel (c) for both t_f and t_c scans: $K = 8$. For panels (b), (d)-(f) no parameters were additionally changed.

> We thus define a system to be a *fast prescrambler*, if, given an arbitrarily large but fixed range of number of degrees of freedom K, there exists a sufficiently small minimum state probability threshold $p < 1/\dim(\{|v_i\rangle\})$, such that the state of the system $|\psi(t)\rangle$, initially in a single state $|\text{in}\rangle$, spreads over the entire Hilbert space $\{|v_i\rangle\}$ into a superposition of all $\dim(\{|v_i\rangle\})$ basis states each with a probability $|C_i|^2 = |\langle\psi(t)|v_i\rangle|^2 > p$, in a time logarithmic in K.

We call this phenomenon "prescrambling" for the following two reasons: First, we want to emphasize the difference to diffusion in [38] and minimal scrambling in [42]. Second, note that the threshold p can be arbitrarily small. Therefore, this type of diffusion of the state will occur on timescales before scrambling, for which the state needs to be sufficiently spread by some chosen measure. It is possible to define a scrambling measure that is equal to that of our prescrambling. Then, however, for some systems a scenario is possible in which the initial state, despite some degree of diffusion over the entire basis, remains the most probable state. That is, if $t_f < t_c$. Consequently, it would be problematic to call the state as truly scrambled.

3.4.2 Application to black holes

We recall that according to the quantum N-portrait of a black hole [14] the parameters of the model in Eq. (3.6) scale as $N = S$, $K = S$, $N_m = S/2$. A thorough scan in this parameter regime is very costly regarding resources and run-time (in the order of months per single data point for $N \sim \mathcal{O}(10)$, and scaling exponentially with N). Additionally, requiring Δ to fulfill Eq. (3.13) would slow down the time-evolution of the system. Consequently, the evolution of the system would need to be considered over longer times. This would further increase the simulation run-time. Nevertheless, we expect the times t_f and t_c to scale in this regime as follows: First, as argued above, we expect t_f to scale logarithmically with N, K and N_m. Second, from supplementary scans of t_f and t_c for $N = K \leq 15$, $N_m = 2$ fixed constant, and thresholds $p = 5 \cdot 10^{-41}$ and $p = 5 \cdot 10^{-21}$, respectively, we find that both t_f and t_c each scale as their corresponding N scans.

Furthermore, as discussed in [36, 37], black holes are conjectured to be fast scramblers. That is, they scramble information in a time logarithmic in the number of degrees of freedom. Therefore, prescrambling is expected to take place during times not later than scrambling, independent of the particular definition of the scrambling measure. We recall that the model in Eq. (3.6) possesses direct all-to-all couplings between the modes of the respective sectors. Consequently, we expect this model to exhibit the fastest prescrambling time, in terms of the number of degrees of freedom, that a physical system can have. We have found indications above that this system prescrambles in a time that scales logarithmically with N, K and N_m separately. We therefore expect this model to prescramble in a time logarithmic in N for the black hole scaling regime.

3.5 Conjectures

Our observations lead us to conjecture the following:

(1) The time in which the fastest prescramblers diffuse the initial state of the system over its entire state space scales logarithmically with the number of degrees of freedom, given a minimum state probability threshold.

(2) The enhanced memory capacity model in Eq. (3.6) is a fast prescrambler.

(3) (Fast) prescrambling occurs not later than (fast) scrambling, irrespective of the choice of a specific measure of the uniformity of the state distribution for the latter.

(4) Therefore, fast scramblers are fast prescramblers.

(5) Specifically, black holes are fast prescramblers.

We emphasize that we do *not* claim that all fast prescramblers are fast scramblers. Likewise, we do not claim that all fast prescramblers have direct all-to-all couplings between the degrees of freedom of the model. Finally, we note that the above are conjectures and should not be viewed as proofs.

3.6 Summary and discussion

In addition to the conjectures above, we conclude this chapter with supplementary comments. First, we note that the spreading of the state of the system, as measured by t_f, has an at least exponential scaling with Δ. Second, our findings provide further evidence that the effects observed within the prototype model with an enhanced memory capacity in Eq. (3.6) agree with the characteristics that black holes are expected to exhibit. Note also that the all-to-all coupling of the modes in the system of Eq. (3.6) fully agrees with the picture of a black hole as a fast scrambler in [38]. Third, one may speculate that the Sachdev-Ye-Kitaev (SYK) model [81,95] is a fast prescrambler, as its modes have all-to-all direct couplings and as it was shown to be a fast scrambler. In the context of prescrambling, our findings also verify that quantum information stored by the system stabilizes it via the memory burden effect.

Based on the observations presented in this chapter, we can introduce several applications of prescrambling. First, systems of enhanced memory capacity, such the the model considered here, may be realized in ultracold boson experiments. Correspondingly, the information-processing properties of such systems, including prescrambling, could be tested. Thus, on the one hand, the enhanced memory capacity model could be realized in the physical regime of large N. On the other hand, the proposed information-processing

characteristics of such systems could be tested in real physical systems. Moreover, if new effects are observed in the experiments, these would allow to propose corresponding new phenomena for black holes. Second, as discussed above, prescrambling supports the arguments of previous works on how black holes store and process information. This contributes to our understanding of these mechanisms at a quantum level. This, in turn, allows us to improve the corresponding microscopic models. At the level of prescrambling, the model in Eq. (3.6) is thus far in agreement with the fast scrambling conjectures of [36,37]. Furthermore, via prescrambling, we may quantitatively conjecture how the first stages of information scrambling occur within a black hole. Third, our prescrambling conjectures, if true, provide a supplementary test on whether a system is a fast scrambler or not, for a large variety of definitions of scrambling. Specifically, if a system is not a fast prescrambler, then it also is not a fast scrambler. This is due to the fact that in this case the state of the system does not diffuse over the entire state space fast enough to allow for fast scrambling.

We note, as an outlook, that a future work [84] will study the temperature dependent scrambling [37,81–83] for the model in Eq. (3.6). Additionally, scrambling within this model and its relation to the Eigenstate Thermalization Hypothesis [44, 45] will be considered in a separate work [96].

Chapter 4

Thermalization Despite Correlation

This chapter is based on the work [3], which is currently in preparation. In it we propose a new thermalization mechanism for isolated quantum systems. The novelty is the occurrence of thermalization despite unignorable correlations between the fluctuations of the eigenstate expectation values $\langle\alpha|\,\hat{A}\,|\alpha\rangle$ of a few-body observable $\hat{A}$ in the eigenstate basis $\{|\alpha\rangle\}$ and the fluctuations of the squared magnitudes of the coefficients $|C_\alpha|^2 = |\,\langle\alpha|\mathrm{in}\rangle\,|^2$ for a non-equilibrium initial state $|\mathrm{in}\rangle$ of the system. We consider a quantum prototype system of enhanced memory capacity introduced to model the information processing characteristics of a black hole. The numerical finite-size analysis of this system provides indications that it approaches thermality in the large system size limit via a variation of the above thermalization mechanism. We discuss the implications of such correlations for thermalization within isolated quantum systems as well as the application of our results to black hole physics.

4.1 Introduction

The first goal of this chapter is to propose a new thermalization mechanism. It is not more general than the already existing ones. However, we are not aware of such a mechanism in the literature. The novelty is that thermalization can still occur even if the fluctuations of the eigenstate expectation values $\langle\alpha|\,\hat{A}\,|\alpha\rangle$ of a few-body observable $\hat{A}$ in the eigenstate basis $\{|\alpha\rangle\}$ and the fluctuations of the squared magnitudes of the coefficients $|C_\alpha|^2 = |\,\langle\alpha|\mathrm{in}\rangle\,|^2$ for a non-equilibrium initial state $|\mathrm{in}\rangle$ possess non-negligible correlations.

The distinctive feature of this thermalization mechanism is that the large fluctuations of both the diagonal matrix elements $A_{\alpha\alpha} = \langle\alpha|\,\hat{A}\,|\alpha\rangle$ and the squared magnitudes of the coefficients $|C_\alpha|^2$ around their respective averages are correlated in such a way that the infinite-time average is equal to the microcanonical ensemble average.

Our second goal is to test thermalization within a quantum prototype system [30, 35] introduced to model the information processing characteristics of a black hole. First, extrapolating the finite-size analysis of this system we find indications that it approaches thermality in the large system size limit. Second, we provide numerical evidence allowing

us to hypothesize that the corresponding thermalization occurs via a variation of the above mechanism, in which only a few of the diagonal matrix elements $A_{\alpha\alpha}$ deviate strongly from their average. Nevertheless, the fluctuations of the $A_{\alpha\alpha}$ elements are correlated with the fluctuations of the $|C_\alpha|^2$ coefficients. Moreover, the $|C_\alpha|^2$'s perform a biased sampling of the distribution of $A_{\alpha\alpha}$'s, but in such a way that the infinite-time average is equal to the microcanonical ensemble average.

The above results provide us with further insight [2, 36, 37, 41] into how black holes may process information. Furthermore, this can allow us to formulate new hypotheses which could be testable for black holes. Moreover, we gain deeper understanding of the phenomenon of quantum thermalization, as well as obtain a further indication that there could exist a thermalization mechanism that would unify the already existing ones and that would operate on a set of more general conditions.

4.1.1 Thermalization

Let $\hat{H}$ be a Hamiltonian of an isolated quantum many-body system of N degrees of freedom with $\mathcal{N}$ energy eigenstates $|\alpha\rangle$ and corresponding energies E_α. Furthermore, let $\hat{A}(t) = \mathrm{e}^{i\hat{H}t}\hat{A}\mathrm{e}^{-i\hat{H}t}$ be a local few-body Hermitian operator in the Heisenberg representation (here and throughout this chapter we set $\hbar \equiv 1$). We assume that the system is prepared in an initial state $|\mathrm{in}\rangle$, for which $\langle \mathrm{in}|\,\hat{A}\,|\mathrm{in}\rangle$ is sufficiently far from the expectation value of the physically reasonable few-body observable $\hat{A}$ predicted by the microcanonical ensemble taken at the energy of the system $\langle \mathrm{in}|\,\hat{H}\,|\mathrm{in}\rangle$. Following a common definition [51], we say that the observable $\hat{A}(t)$ *thermalizes* if:

(i) The infinite-time average of the expectation value of the observable $\overline{\langle \hat{A}(t)\rangle}$ is equal to its microcanonical average, and

(ii) The temporal fluctuations of $\langle \hat{A}(t)\rangle$ about the microcanonical average are small at most later times.

The ETH states that an observable $\hat{A}(t)$ will thermalize if [44, 45, 47, 48, 97, 98]:

(1) The diagonal matrix elements $A_{\alpha\alpha} = \langle\alpha|\,\hat{A}\,|\alpha\rangle$ vary approximately smoothly with E_α *and* the magnitude of the difference between neighboring values $|A_{\alpha+1,\alpha+1} - A_{\alpha\alpha}|$ is exponentially small in N, and

(2) The magnitudes of the off-diagonal matrix elements $|A_{\alpha\beta}| = |\,\langle\alpha|\,\hat{A}\,|\beta\rangle\,|$ with $\alpha \neq \beta$ are themselves exponentially small in N.

These ETH conditions on the matrix elements are often compactly summarized as [47, 48, 99–101]

$$A_{\alpha\beta} = \mathcal{A}(E)\delta_{\alpha\beta} + \mathrm{e}^{-S(E)/2} f_A(E,\omega) R_{\alpha\beta}, \tag{4.1}$$

where $E = (E_\alpha + E_\beta)/2$, $\omega = E_\alpha - E_\beta$, and $\mathcal{A}(E) = \mathrm{tr}[\hat{\rho}\hat{A}]$ is the microcanonical average at energy E with the thermal density matrix $\hat{\rho} \equiv \mathrm{e}^{-\beta\hat{H}}/Z$, the partition function $Z \equiv \mathrm{tr}[\mathrm{e}^{-\beta\hat{H}}]$,

and the inverse temperature β which is set by $E = \mathrm{tr}[\hat{\rho}\hat{H}]$. Furthermore, $S(E)$ is the thermodynamic entropy at energy E given by the logarithm of the number of degenerate microstates, and $f_A(E,\omega)$ is a real function that depends on the specific operator $\hat{A}$ with $f_A(E,\omega) = f_A(E,-\omega)$. Both $\mathcal{A}(E)$ and $f_A(E,\omega)$ are smooth functions of their arguments. Finally, $R_{\alpha\beta}$ is a random Hermitian matrix of entries with zero mean and unit variance.

Additionally, it is commonly assumed that all the energy eigenvalues E_α are non-degenerate [47, 102]. Finally, the condition that the system is prepared in an initial state with a relatively small energy uncertainty [45–48, 55, 98] is frequently assumed to hold implicitly in the literature. We call this the 0-th condition of the ETH:

(0) The initial state $|\mathrm{in}\rangle$ is assumed to be a superposition of energy eigenstates, which are all sufficiently close in energy.

There exist systems that thermalize, but do not fulfill the conditions of the ETH. This has motivated the formulation of various thermalization mechanisms, such as those mentioned previously. Below we briefly review the mechanisms discussed in [55]. This allows for a clearer connection to the thermalization mechanism introduced in this chapter. Under the assumption that the initial state has a sufficiently narrow spread in energy, the authors of [55] suggest two possible mechanisms that are distinct from the ETH for achieving thermalization:

(i) Even for eigenstates that are close in energy, there are large fluctuations in both the eigenstate expectation values $A_{\alpha\alpha} = \langle\alpha|\,\hat{A}\,|\alpha\rangle$ and the squared magnitudes of the coefficients $|C_\alpha|^2 = |\,\langle\alpha|\mathrm{in}\rangle\,|^2$. However, the fluctuations for these two quantities are not correlated for initial states of physical interest. Therefore, there is an unbiased sampling of the $A_{\alpha\alpha}$ values by the squared magnitudes of the coefficients $|C_\alpha|^2$ when performing the sum for the diagonal ensemble $\overline{\langle\hat{A}(t)\rangle} = \sum_{\alpha=1}^{\mathcal{N}} |C_\alpha|^2 A_{\alpha\alpha}$.

(ii) The squared magnitudes of the coefficients $|C_\alpha|^2$ exhibit essentially no fluctuations between eigenstates close in energy for initial conditions of physical interest.

However, as noted by the authors themselves, for the above two mechanisms, in contrast to ETH, there may exist initial states for which the system does not thermalize.

The thermalization mechanism proposed in this chapter is a modification of the mechanism (i) above. Namely, we allow for correlations, irrespective of how small, between the fluctuations of $A_{\alpha\alpha}$ and $|C_\alpha|^2$. The specific magnitude and form of the correlations are unimportant, as far as when performing a hypothesis test with the null hypothesis that the two aforementioned sets of fluctuations are independent and an alternative hypothesis that they are not, the test shows that the null hypothesis is to be rejected at a chosen significance level. In this chapter we provide numerical evidence that a system in [30, 35] approaches thermality in the large system size limit via a variation of this mechanism, with the independence hypothesis rejected at the 0.05 significance level by the majority of the applied independence tests.

In the finite-size scaling analysis of the system we find that only a few of the elements $A_{\alpha\alpha}$ differ strongly from their average, but are biased towards and are strongly weighted by the $|C_\alpha|^2$'s. However, the fluctuations of $A_{\alpha\alpha}$ and $|C_\alpha|^2$ are distributed and correlated in such a way that these biases collectively balance each other out. It is important to note that from our numerical analysis we expect the maxima of the fluctuations of the $A_{\alpha\alpha}$'s, within an appropriate energy window centered around the energy of the system, *not* to vanish in the thermodynamic limit, i.e. in the limit of large system size. In fact, we observe that, within the energy window, the maximal absolute difference of the $A_{\alpha\alpha}$'s that are neighbors in energy, in the thermodynamic limit approaches a value comparable (with a factor in the range of $[1.035, 1.122]$) to the average value of the $A_{\alpha\alpha}$'s within that energy window.

4.1.2 The model

As a prototype model of enhanced memory capacity we again consider the setup of Eqs. (3.1)-(3.13) from Sec. 3.2. As before, we set $K = K'$. Additionally, we take the coupling strengths at their maximum values $C_b = 1/\sqrt{N}$, $C_m = 1/(\sqrt{N_m}\sqrt{K})$. Furthermore, we adopt the following scaling regime: In accordance with the black hole's quantum N-portrait [14], the parameters scale as $N = S$, $K = S$, $N_m = S/2$ for a black hole of entropy $S \gg 1$ [35]. If the occupation number of the master mode N is odd, we round the total occupation number of the memory modes down to the nearest integer: $N_m = \lfloor N/2 \rfloor$. Finally, we choose $\Delta = N/2$, which satisfies the constraint in Eq. (3.13) for large N. This leaves a single free parameter: The system size N, which we vary in the simulations below. The numerical analysis is performed with QuSpin [92–94]. For the entirety of the chapter we assume that the Hamiltonian of the system does not have any degenerate eigenvalues E_α for any values of N.

4.2 Test of thermalization

To test thermalization within the model in Eq. (3.6) we need to verify that the conditions (i) and (ii) of thermalization in Sec. 4.1.1 are satisfied. We deliberately consider only one realization of the system. That is, the values of the couplings of the individual modes as well as the initial state of the system are unique and fixed. This avoids averaging over multiple realizations and thereby obtaining a false positive result. As the values of the couplings between the individual memory modes were chosen essentially at random, we claim that this one realization of the system is a typical representative. Additionally, for the same reason as above, as the few-body observable we consider the occupation number $\hat{n}_i$ of only the mode $i = 1$ from the K sector. We provide numerical evidence that this observable approaches thermality in the large system size limit.

To calculate the quantities considered in the numerical analysis we express the initial

state in Eq. (3.5) as

$$|\text{in}\rangle = \sum_{\alpha=1}^{\mathcal{N}} C_\alpha \, |\alpha\rangle \tag{4.2}$$

with the normalization $\sum_{\alpha=1}^{\mathcal{N}} |C_\alpha|^2 = 1$. The dimension of the Hilbert space is denoted by $\mathcal{N}$. Assuming no degeneracy in the eigenvalues E_α, we define the infinite-time average of the operator $\hat{n}_i$ as

$$\overline{n}_i \equiv \overline{\langle \hat{n}_i(t) \rangle} = \lim_{T\to\infty} \frac{1}{T} \int_0^T \langle \hat{n}_i(t) \rangle \, \mathrm{d}t = \sum_{\alpha=1}^{\mathcal{N}} |C_\alpha|^2 n_{i,\alpha\alpha}. \tag{4.3}$$

The magnitude of the temporal fluctuations of $\langle \hat{n}_1(t) \rangle$ about $\overline{n}_i$ can be calculated as

$$\sigma_{i,t} \equiv \left[\overline{\langle \hat{n}_i(t) \rangle^2} - \overline{n}_i^2 \right]^{1/2} = \left[\sum_{\substack{\alpha,\beta \\ \alpha\neq\beta}} |C_\alpha|^2 |C_\beta|^2 |n_{i,\alpha\beta}|^2 \right]^{1/2}. \tag{4.4}$$

The energy of the system is given by

$$\overline{E} = \langle \hat{H} \rangle = \sum_{\alpha=1}^{\mathcal{N}} |C_\alpha|^2 E_\alpha. \tag{4.5}$$

We define the half-spread of the energy range of the eigenvalues E_α as

$$\Delta E \equiv \frac{1}{2} \left(E_{\alpha,\max} - E_{\alpha,\min} \right). \tag{4.6}$$

As the half-width of the energy window for the microcanonical ensemble average we take the quantum energy uncertainty [45–48, 98]

$$\sigma_{E,\mathrm{q}} \equiv \left[\langle \hat{H}^2 \rangle - \langle \hat{H} \rangle^2 \right]^{1/2} = \left[\sum_{\alpha=1}^{\mathcal{N}} |C_\alpha|^2 \left(E_\alpha - \overline{E} \right)^2 \right]^{1/2} = \left[\left(\sum_{\alpha=1}^{\mathcal{N}} |C_\alpha|^2 E_\alpha^2 \right) - \overline{E}^2 \right]^{1/2}. \tag{4.7}$$

We denote the number of eigenvalues E_α contained within the interval $(\overline{E} - \sigma_{E,\mathrm{q}}, \overline{E} + \sigma_{E,\mathrm{q}})$ by $\mathcal{N}_{\sigma_{E,\mathrm{q}}}$. Finally, we define the microcanonical average of $\hat{n}_i$ as

$$n_{i,\mathrm{mc}} \equiv \frac{1}{\mathcal{N}_{\sigma_{E,\mathrm{q}}}} \sum_{\substack{\alpha \\ |\overline{E} - E_\alpha| < \sigma_{E,\mathrm{q}}}} n_{i,\alpha\alpha}. \tag{4.8}$$

Figure 4.1 depicts an exemplary plot of $\langle \hat{n}_1(t) \rangle$ over time t for $N = 8$. We observe similar behavior of the observable for other values of N. In Fig. 4.1, the expectation value of the occupation number of the mode $i = 1$ equilibrates to $\overline{n}_1 \approx 0.32$ with small temporal fluctuations at later times. Evidently, it does not thermalize ideally, as for this to be the case $\overline{n}_1 = n_{1,\mathrm{mc}} = 0.25$ would have to hold, since $K = K'$ and $N_m = \lfloor K/2 \rfloor$.

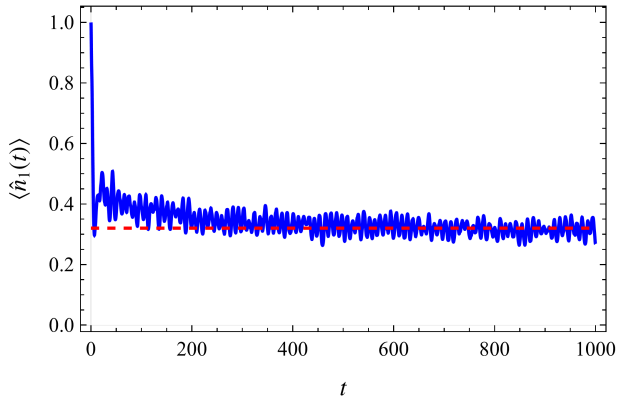

Figure 4.1: Relaxation dynamics. Exemplary plot of the expectation value of the time-evolved occupation number of the first mode from the K memory sector $\langle \hat{n}_1(t) \rangle$ over time t for $N = 8$, marked by the solid blue line. The corresponding infinite-time average $\overline{n}_1 \approx 0.32$ is marked by the red dashed line.

However, we would like to know how the system behaves in the thermodynamic limit. To analyze this numerically, we perform finite-size scans of the system over N. The results are shown in Fig. 4.2 with the respective best obtained fit functions for the various quantities. The full list of the corresponding fit parameters is presented in Table A.2 in the Appendix. The fits that are plotted in the figures of the chapter and the corresponding values of the fit parameters are marked with a "*" in Table A.2. Table A.2 additionally includes other fits that may also be appropriate for the obtained data. We include these for completeness and to aid the comparison. Moreover, we do not want to exclude the possibility that these fit functions may become more suitable in a future study where more numerical data for larger N will be available.

To avoid the effects of small values of N, we consider the fit of $n_{1,\mathrm{mc}}$ only for even N, where $N_m = K/2$ without the need to round down to the nearest integer as is the case for odd N. We expect $\overline{n}_1$ and $n_{1,\mathrm{mc}}$, shown in Figs. 4.2 (a) and (b), respectively, to possess the same scaling with N. The fit results of Table A.2 provide evidence that the thermalization condition (i) of Sec. 4.1.1, namely that $\overline{n}_1 = n_{1,\mathrm{mc}} = 0.25$, can be fulfilled ideally in the large-N limit if these quantities scale as $\exp(-cN)$ with c a positive constant. We observe from Fig. 4.2 (b) that the data points for both the even and the odd N appear to converge to 0.25. The results therefore suggest that the thermalization condition (i) is satisfied, with deviations from ideal thermality exponentially small in N. The fit results in Table A.2 suggest that the temporal fluctuations $\sigma_{1,t}$ of $\langle \hat{n}_1(t) \rangle$ about $\overline{n}_1$, shown in Fig. 4.2 (c), vanish exponentially with N in the large system size limit. This suggests that the thermalization condition (ii) of Sec. 4.1.1 is fulfilled. We can therefore conclude that the numerical data provides evidence that the observable $\hat{n}_1$ thermalizes ideally in the thermodynamic limit.

The energy of the system $\overline{E}$ is zero, as can be seen from Eqs. (3.5) and (3.6), and as is numerically confirmed in Fig. 4.2 (d). Therefore, we cannot judge the smallness of the

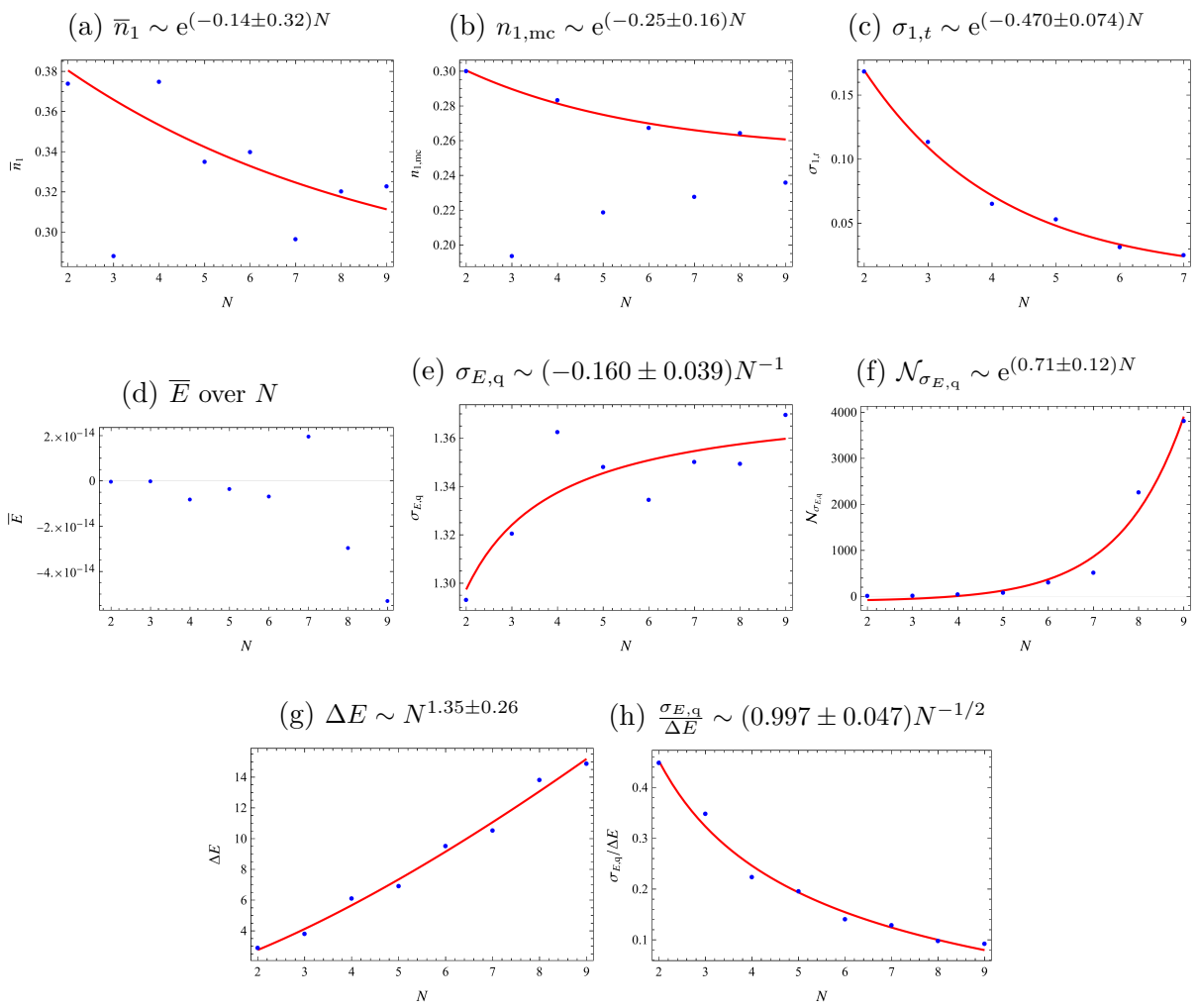

Figure 4.2: Thermalization. The subfigures show the scaling of the various quantities with N. For compactness, only the general scaling is presented in the subcaptions. The complete list of fit parameter values is given in Table A.2 in the Appendix. The numerical data is represented by points and the corresponding fits are shown as solid lines. The individual subfigures show: (a) the infinite-time average $\overline{n}_1$ of $\hat{n}_1$, (b) the microcanonical average $n_{1,\mathrm{mc}}$ of $\hat{n}_1$, (c) the temporal fluctuations $\sigma_{1,t}$ of $\langle \hat{n}_1(t) \rangle$ about $\overline{n}_1$, (d) the energy of the system $\overline{E}$, (e) the quantum energy uncertainty $\sigma_{E,\mathrm{q}}$, (f) the number of eigenvalues $\mathcal{N}_{\sigma_{E,\mathrm{q}}}$ within the interval $(\overline{E} - \sigma_{E,\mathrm{q}}, \overline{E} + \sigma_{E,\mathrm{q}})$, (g) the half-spread of the energy range ΔE, (h) the ratio of the quantum energy uncertainty to the half-spread of the energy range $\sigma_{E,\mathrm{q}}/\Delta E$. For $\overline{n}_1(N)$ the data point $N = 3$ was excluded from the fits. The fits of $n_{1,\mathrm{mc}}(N)$ were performed only over the data points with even N.

quantum energy uncertainty $\sigma_{E,\mathrm{q}}$, which we take as the half-width of the energy window for the microcanonical ensemble average, by comparing it with $\overline{E}$. Instead, as a criterion for the smallness of the microcanonical energy window, we compare $\sigma_{E,\mathrm{q}}$ to the half-spread ΔE of the energy range of the eigenvalues E_α. The corresponding results are shown in Figs. 4.2 (e), (g) and (h). All fit functions for $\sigma_{E,\mathrm{q}}$ in Table A.2 indicate that it approaches a constant value in the interval $[1.344, 1.437]$ in the large-N limit. Conversely, the fit results of Table A.2 suggest that ΔE increases with N, and, consistently, $\sigma_{E,\mathrm{q}}/\Delta E$ approaches zero with increasing N. The fit results therefore indicate that the microcanonical energy window becomes infinitely thin in the large system size limit, when compared to the energy range of the eigenvalues.

Note that although $\sigma_{E,\mathrm{q}}$ approaches a constant in the large system size limit, the number of eigenvalues $\mathcal{N}_{\sigma_{E,\mathrm{q}}}$ contained within the interval $(\overline{E}-\sigma_{E,\mathrm{q}}, \overline{E}+\sigma_{E,\mathrm{q}})$, as shown in Fig. 4.2 (f), increases rapidly with N, as suggested by the fit results in Table A.2.

4.3 Test of ETH

In this section we test the ETH conditions (0), (1) and (2) listed in Sec. 4.1.1. We provide numerical evidence that the observable $\hat{n}_1$ within the model in Eq. (3.6) does not fulfill the ETH conditions. Specifically, the ETH condition (1) on the diagonal matrix elements $n_{1,\alpha\alpha}$ is not satisfied.

4.3.1 Condition (0)

To fulfill the ETH condition (0), the initial state of the system has to have a relatively small energy uncertainty. That is, the initial state needs to be in a superposition of eigenstates that are all sufficiently close in energy. Figure 4.3 shows an exemplary plot of the coefficients C_α over the eigenstate energy E_α for $N = 8$. The points within the interval $(\overline{E} - \sigma_{E,\mathrm{q}}, \overline{E} + \sigma_{E,\mathrm{q}})$ are marked in red, and the rest are marked in blue. As can be seen from the plot, the points closer to $\overline{E} = 0$ have weights C_α with greater absolute values. We observe analogous behavior for other values of N. Additionally, as discussed in the previous section, the relative width of the energy window $\sigma_{E,\mathrm{q}}/\Delta E$ appears to approach zero with increasing N. This provides evidence that the initial state in Eq. (3.5) is indeed a superposition of eigenstates that are close in energy. The results therefore suggest that the ETH condition (0) is fulfilled, also in the large-N limit.

4.3.2 Condition (1)

For the observable $\hat{n}_1$ to fulfill condition (1) of the ETH, the diagonal matrix elements $n_{1,\alpha\alpha}$ need to vary approximately smoothly with E_α and the magnitude of the difference between neighboring values $|n_{1;\alpha+1,\alpha+1} - n_{1;\alpha,\alpha}|$ needs to be exponentially small in N. We test both parts of this condition below. First, we define an auxiliary quantity, the average

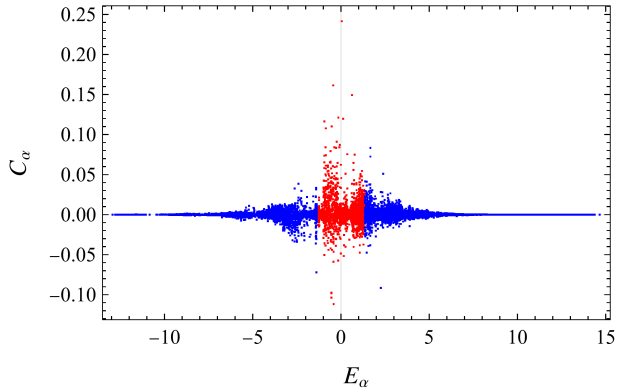

Figure 4.3: Exemplary plot of C_α over the eigenstate energy E_α for $N = 8$. The data points within the energy shell, i.e. for which $|\overline{E} - E_\alpha| < \sigma_{E,\mathrm{q}}$, are marked in red, and those on or outside the shell are marked in blue.

value of all diagonal matrix elements,

$$n_{i,\mathrm{av}} \equiv \frac{1}{\mathcal{N}} \sum_{\alpha=1}^{\mathcal{N}} n_{i,\alpha\alpha}. \tag{4.9}$$

This auxiliary factor allows us to appropriately normalize and compare the magnitude of the difference between diagonal elements neighboring in energy for different N. To do this, we define the normalized average absolute difference between neighboring diagonal matrix elements

$$\delta_i \equiv \frac{1}{n_{i,\mathrm{av}}} \frac{1}{\mathcal{N}-1} \sum_{\alpha=1}^{\mathcal{N}-1} |n_{i;\alpha+1,\alpha+1} - n_{i;\alpha,\alpha}|, \tag{4.10}$$

and its normalized corrected standard deviation

$$\sigma_i \equiv \frac{1}{n_{i,\mathrm{av}}} \left[\frac{1}{\mathcal{N}-2} \sum_{\alpha=1}^{\mathcal{N}-1} \left(|n_{i;\alpha+1,\alpha+1} - n_{i;\alpha,\alpha}| - n_{i,\mathrm{av}} \delta_i \right)^2 \right]^{1/2}. \tag{4.11}$$

Similarly, we define analogous quantities for the data points within the microcanonical energy window,

$$\delta_{i,\mathrm{mc}} \equiv \frac{1}{n_{i,\mathrm{mc}}} \frac{1}{\mathcal{N}_{\sigma_{E,\mathrm{q}}} - 1} \sum_{\substack{\alpha \\ |\overline{E}-E_\alpha|<\sigma_{E,\mathrm{q}} \\ |\overline{E}-E_{\alpha+1}|<\sigma_{E,\mathrm{q}}}} |n_{i;\alpha+1,\alpha+1} - n_{i;\alpha,\alpha}| \tag{4.12}$$

and

$$\sigma_{i,\mathrm{mc}} \equiv \frac{1}{n_{i,\mathrm{mc}}} \left[\frac{1}{\mathcal{N}_{\sigma_{E,\mathrm{q}}} - 2} \sum_{\substack{\alpha \\ |\overline{E}-E_\alpha|<\sigma_{E,\mathrm{q}} \\ |\overline{E}-E_{\alpha+1}|<\sigma_{E,\mathrm{q}}}} \left(|n_{i;\alpha+1,\alpha+1} - n_{i;\alpha,\alpha}| - n_{i,\mathrm{mc}} \delta_{i,\mathrm{mc}} \right)^2 \right]^{1/2}. \tag{4.13}$$

Additionally, we define the maximum absolute difference among all pairs of neighboring diagonal elements by

$$\delta_{i,\max} \equiv \frac{1}{n_{i,\mathrm{av}}} \max\{|n_{i;\alpha+1,\alpha+1} - n_{i;\alpha,\alpha}|\}. \tag{4.14}$$

Finally, we define the maximum absolute difference among pairs of neighboring diagonal elements within $\sigma_{E,\mathrm{q}}$, i.e. for $|\overline{E} - E_\alpha| < \sigma_{E,\mathrm{q}}$ and $|\overline{E} - E_{\alpha+1}| < \sigma_{E,\mathrm{q}}$, by

$$\delta_{i,\max}^{\mathrm{mc}} \equiv \frac{1}{n_{i,\mathrm{mc}}} \max\{|n_{i;\alpha+1,\alpha+1} - n_{i;\alpha,\alpha}|\}. \tag{4.15}$$

As can be seen from Fig. 4.4 (a), the diagonal matrix elements $n_{1,\alpha\alpha}$ do not vary smoothly over E_α for $N = 8$. We observe analogous behavior for other values of N. This is already in conflict with the first part of the ETH condition (1). However, we are interested in the large-N limit, and whether the fluctuations between neighboring diagonal elements decay exponentially in N.

First, from Fig. 4.4 (b) we observe that for even N the average of all diagonal elements $n_{1,\mathrm{av}}$ is equal to 0.25, with its value approaching 0.25 as $\mathcal{O}(N^{-1})$ for odd N. To minimize small-N effects, we nevertheless perform the fits of δ_1 and $\delta_{1,\mathrm{mc}}$ only over the data points with even N. The results are shown in Figs. 4.4 (c) and (d), correspondingly. We observe that both fits approach zero exponentially in the large-N limit. This is explained by the fact that the diagonal elements $n_{1,\alpha\alpha}$ are clustered around $n_{1,\mathrm{av}}$, with their number increasing exponentially both in total and within the microcanonical energy window (see Fig. 4.2 (f)). In other words, we find that *on average*, the magnitude of the difference between neighboring diagonal elements is indeed exponentially small in N. However, the fluctuations between the individual diagonal elements can still be substantial.

To investigate this, we consider the maximum absolute difference among pairs of neighboring diagonal elements both in the entire range of energy eigenvalues, $\delta_{1,\max}$, and also within the microcanonical energy window, $\delta_{1,\max;\mathrm{mc}}$. The results are shown in Fig. 4.4 (e) as blue and red data points, respectively. For the fit we consider the maximum absolute difference among pairs of neighboring diagonal elements only within $\sigma_{E,\mathrm{q}}$ and only for even N. As can be seen from Fig. 4.4 (e), these fluctuations are also the smallest. We find that $\delta_{1,\max;\mathrm{mc}}$ approaches a value that lies within the interval $[1.035, 1.122]$ in the thermodynamic limit. In other words, the maximum difference between neighboring diagonal elements within the microcanonical energy window slightly exceeds the microcanonical average itself. Clearly, this is a considerable fluctuation. Note from Fig. 4.4 (e), that this maximal fluctuation is even larger for points both outside of the microcanonical energy shell and for other values of N.

Therefore, the numerical results suggest that the ETH condition (1) is not fulfilled, as the elements $n_{1,\alpha\alpha}$ do not vary smoothly with E_α and the magnitude of the difference between neighboring values $|n_{1;\alpha+1,\alpha+1} - n_{1;\alpha,\alpha}|$ is not exponentially small in N. This holds not only for finite N, but also in the large system size limit. Nevertheless, as shown previously, $\overline{n}_1$ and $n_{1,\mathrm{mc}}$ both appear to approach the same value of 0.25 in the thermodynamic limit. In a later section we discuss the details of the corresponding thermalization mechanism.

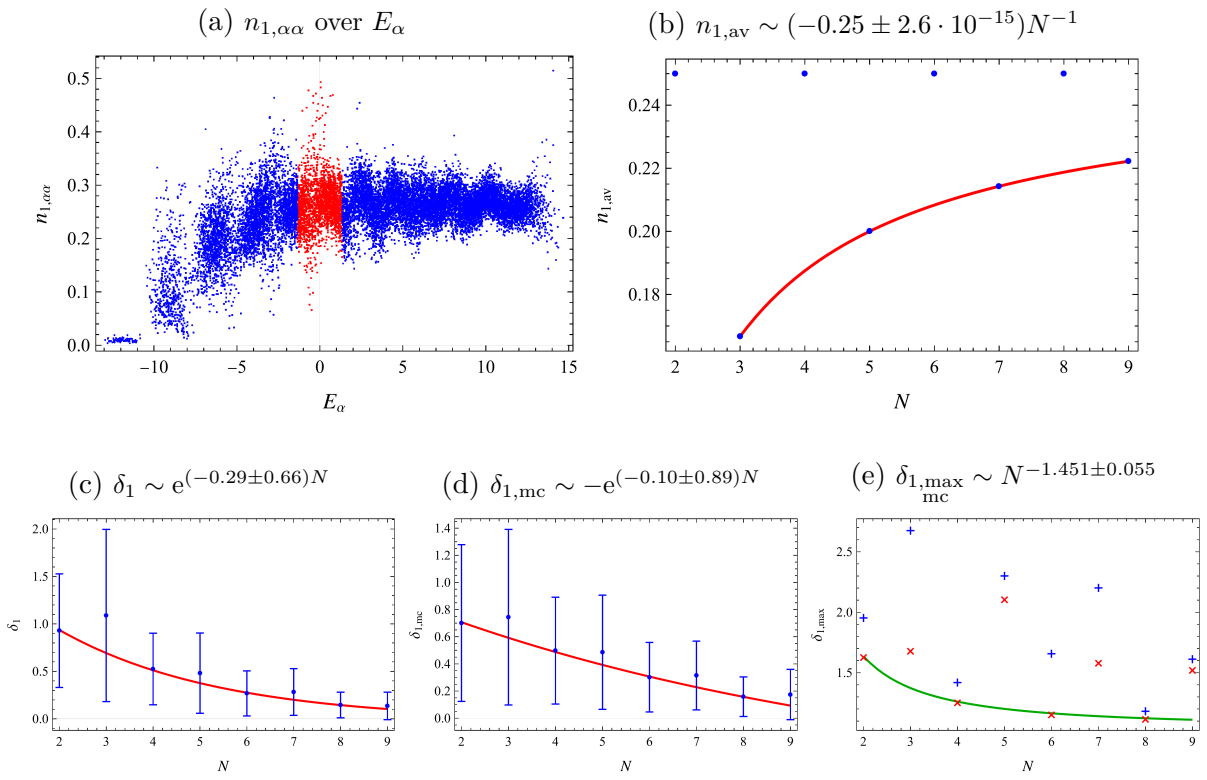

Figure 4.4: Test of ETH condition (1). Subfigure (a) shows an exemplary plot of $n_{1,\alpha\alpha}$ over E_α for $N = 8$. The points within the interval $(\overline{E} - \sigma_{E,\mathrm{q}}, \overline{E} + \sigma_{E,\mathrm{q}})$ are marked in red, the rest are marked in blue. The other subfigures show the scaling of the various quantities with N. As previously, only the general scaling is presented here, with the full list of fit parameter values given in Table A.2 in the Appendix. The numerical data is represented by points and the corresponding fits are depicted by solid lines. The individual subfigures show: (b) the average of all diagonal elements $n_{1,\mathrm{av}}$ with the corresponding fit performed only over the data points with odd N, (c) the normalized average absolute difference δ_1 between neighboring diagonal elements with its normalized corrected standard deviation σ_1 depicted by error bars, (d) the normalized average absolute difference $\delta_{1,\mathrm{mc}}$ within the microcanonical energy window with the corresponding normalized corrected standard deviation $\sigma_{1,\mathrm{mc}}$ as error bars, (e) the maximum absolute difference among all pairs of neighboring diagonal elements $\delta_{i,\max}$ marked with blue "+"-s, the analogous quantity for the diagonal elements within $\sigma_{E,\mathrm{q}}$ marked with red "×"-s and the fit over the latter data points for even N marked as a solid green line. The fits of δ_1 and $\delta_{1,\mathrm{mc}}$ are weighted fits with inverse squares of the corresponding normalized corrected standard deviations as weights, performed only over the data points with even N.

4.3.3 Condition (2)

For the observable $\hat{n}_1$ to fulfill condition (2) of the ETH, the magnitudes of the off-diagonal matrix elements need to be exponentially small in N. If this condition is satisfied, it leads to the fulfillment of thermalization condition (ii) on the temporal fluctuations of the observable. We have previously argued the latter to be satisfied. In this section we provide numerical evidence that the ETH condition (2) is fulfilled. The results are presented in Fig. 4.5. The diagonal matrix elements dominate over the off-diagonal ones, as shown in Fig. 4.5 (a). We observe analogous behavior also for other values of N. Moreover, the average absolute value $\mu_{|n_{1,\alpha\beta}|}$ of the off-diagonal matrix elements $n_{1,\alpha\beta}$ with $\alpha \neq \beta$ decays exponentially to zero with increasing N, as can be seen from Fig. 4.5 (b) and the corresponding fit results in Table A.2.

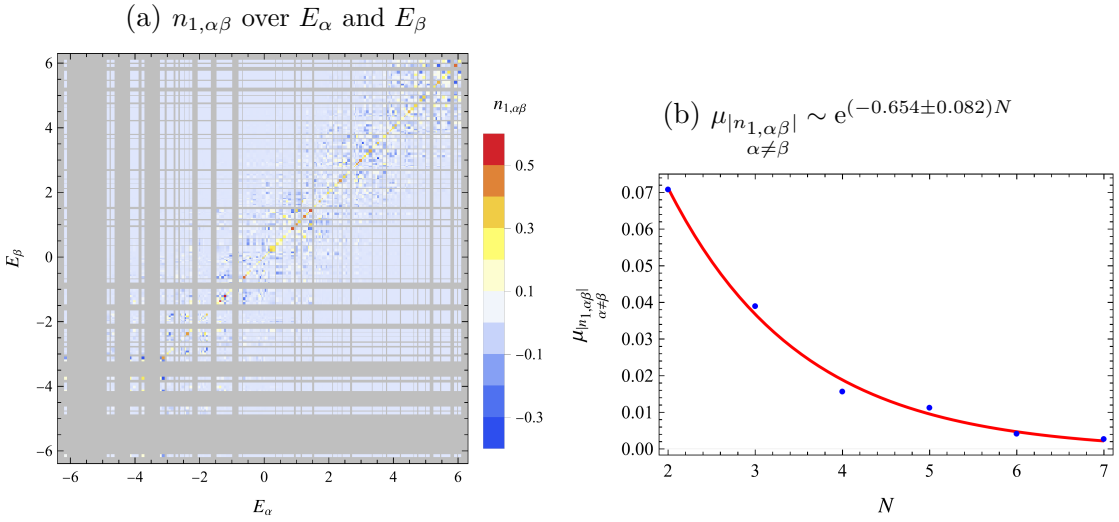

Figure 4.5: Test of ETH condition (2). Subfigure (a) shows an exemplary plot of $n_{1,\alpha\beta}$ over E_α and E_β for $N = 4$. The color bar represents the value of the individual matrix elements. Subfigure (b) shows the mean absolute value of the off-diagonal matrix elements over N. The data is represented by points and the corresponding fit by a solid line.

4.4 Tests of other mechanisms

We have established above that within the system in Eq. (3.6) the observable $\hat{n}_1$ appears to thermalize not according to the ETH, as the condition (1) is violated, but via a different mechanism. In this section we provide arguments on why this thermalization cannot be explained with the other various thermalization mechanisms mentioned previously.

The squared magnitudes of the coefficients $|C_\alpha|^2$ exhibit fluctuations (see Fig. 4.3 for the fluctuations of the C_α's) between eigenstates close in energy, especially within the

interval $(\overline{E} - \sigma_{E,\mathrm{q}}, \overline{E} + \sigma_{E,\mathrm{q}})$. Therefore, thermalization cannot occur via the mechanism (ii) of [55], discussed in Sec. 4.1.1.

The fluctuations of diagonal elements $n_{1,\alpha\alpha}$ do not vanish in the thermodynamic limit (see Fig. 4.4 (e)). The *thermal ETH* and the *smoothness ETH* mechanisms [58] therefore also do not apply.

The thermalization of $\hat{n}_1$ within the model of Eq. (3.6) cannot be explained also by *thermalization due to integrability* [59]. We consider the isolated quantum system in Eq. (3.6) to be non-integrable (see, for example, [50, 103] for detailed discussions on integrability). That is, among other properties, in the context of [59], not analytically solvable. Additionally, note that the authors of [59] discuss thermalization on an example of a time-dependent Hamiltonian, which is not the case for the system in Eq. (3.6).

As we regard the model investigated in this chapter as non-integrable, we consequently consider it to be also not nearly integrable. Additionally, we do not observe two separate relaxation timescales. That is, we do not see a process in which the system first equilibrates on a short timescale to a meta-stable state, and then on a longer timescale reaches the true thermal equilibrium. We therefore conclude that *prethermalization* [54] is not the mechanism responsible for the thermalization of this observable in this system.

Concerning the distribution of the diagonal matrix elements $n_{1,\alpha\alpha}$ around their average value, there are two factors at play: First, the fraction of points that deviate from the mean, and second, their support, i.e. how large is the deviation of their values from the mean. The mechanism behind the *strong ETH* [56] is that in the thermodynamic limit, the support of the distribution of the diagonal elements of the observable in the eigenstate basis around its thermal value shrinks to zero. That is, the rare non-thermal states disappear completely. As can be observed from Fig. 4.4 (e), the rare states do not vanish in the large-N limit, since $|n_{1;\alpha+1,\alpha+1} - n_{1;\alpha,\alpha}|$ approaches a value approximately equal to $n_{1,\mathrm{mc}}$. This provides evidence for the existence of a rare state in the thermodynamic limit with a deviation of $\gtrsim n_{1,\mathrm{mc}}/2$ within the microcanonical energy window. We therefore conclude that this thermalization mechanism is not applicable to our case.

If thermalization occurs via the *weak ETH* [56], the fraction of the non-thermal states vanishes in the thermodynamic limit, so that the distribution of the diagonal matrix elements shrinks around the thermal value. However, in contrast to the strong ETH, the support of the elements does not shrink towards their thermal value. That is, rare states exist, but the $|C_\alpha|^2$'s do not bias them too much. In the next section we provide numerical evidence that this is not the case for our observable and system. Note that the authors of [56] also suggest that a plausible, but not necessary, assumption for achieving thermalization via the weak ETH is that the $|C_\alpha|^2$'s sample the elements $n_{1,\alpha\alpha}$ with the same energy rather uniformly. Similarly, other works [104, 105] also conjecture the randomness of the $|C_\alpha|^2$'s in the context of the ETH.

Mechanisms with the general idea that the fluctuations of the quantities are random include the mechanism (i) of [55], discussed in Sec. 4.1.1, and the *Eigenstate Randomization Hypothesis* (ERH) [57]. The former states that the fluctuations of $n_{1,\alpha\alpha}$ and those of $|C_\alpha|^2$ are not correlated. The latter states that the elements $n_{1,\alpha\alpha}$ fluctuate randomly. Below we argue that both of the above conditions are not fulfilled, as the two sets of fluctuations are

unignorably correlated.

4.5 Thermalization despite correlation

In this section we provide numerical evidence that the weak ETH, as well as both the mechanism (i) of [55] (discussed in Sec. 4.1.1) and the ERH are not applicable to our system. We demonstrate this by considering the correlations in the fluctuations of the coefficients-squared C_α^2 and of the diagonal matrix elements $n_{i,\alpha\alpha}$. We define the normalized fluctuations of $n_{i,\alpha\alpha}$ about their average $n_{i,\mathrm{av}}$ as

$$\Delta_{n_{i,\alpha\alpha}} \equiv \frac{n_{i,\alpha\alpha} - n_{i,\mathrm{av}}}{n_{i,\mathrm{av}}} = \frac{n_{i,\alpha\alpha}}{n_{i,\mathrm{av}}} - 1, \tag{4.16}$$

and the normalized fluctuations in C_α^2 as

$$\Delta_{C_\alpha^2} \equiv \frac{C_\alpha^2 - 1/\mathcal{N}}{1/\mathcal{N}} = C_\alpha^2 \mathcal{N} - 1. \tag{4.17}$$

Exemplary plots for $N = 8$ are shown in Figs. 4.6 (a), (b), (c), (d), (e) and (f). We observe that the two sets of fluctuations appear to be clearly correlated, with the larger values of $n_{1,\alpha\alpha}$ biased towards by the higher C_α^2 values. Plots for other values of N exhibit the same trait. This is already a strong indication against the fulfillment of conditions for the weak ETH. Note from Figs. 4.6 (d) and (e) that the tails of the distribution for the diagonal matrix elements decay differently as $n_{1,\alpha\alpha}$ diverges from $n_{1,\mathrm{av}}$. Namely, the tail of the distribution for $n_{1,\alpha\alpha} < n_{1,\mathrm{av}}$ decays slower than that for $n_{1,\alpha\alpha} > n_{1,\mathrm{av}}$. This is a significant component of the thermalization mechanism that we discuss in the next section.

We first attempt to investigate how the correlation between the two sets of fluctuations depends on N by analyzing two quantities: The mutual information of $\Delta_{n_{1,\alpha\alpha}}$ and $\Delta_{C_\alpha^2}$, and the Pearson correlation coefficient. We calculate the mutual information of variables X and Y as

$$I(X,Y) = H(X) + H(Y) - H(X,Y) \tag{4.18}$$

with marginal entropies $H(X)$ and $H(Y)$, where $H(X)$ is defined by

$$H(X) = -\sum_{x\in\mathcal{X}} p(x) \ln p(x), \tag{4.19}$$

with $H(Y)$ defined analogously, and the joint entropy of X and Y

$$H(X,Y) = -\sum_{x\in\mathcal{X}} \sum_{y\in\mathcal{Y}} p(x,y) \ln p(x,y). \tag{4.20}$$

The mutual information $I(X,Y)$ is a measure of how much information about one variable is obtained by measuring the other, and vice versa. Note that, however, $I(X,Y)$ depends on

the binning method of the data. For the sake of brevity, we define the mutual information of $\Delta_{n_{1,\alpha\alpha}}$ and $\Delta_{C^2_\alpha}$ as

$$I \equiv I\left(\Delta_{n_{1,\alpha\alpha}}; \Delta_{C^2_\alpha}\right). \tag{4.21}$$

We also calculate the Pearson correlation coefficient of variables X and Y,

$$\rho_{X,Y} = \frac{\mathrm{cov}(X,Y)}{\sigma_X \sigma_Y}, \tag{4.22}$$

where $\mathrm{cov}(X,Y)$ is the covariance of X and Y, and σ_X and σ_Y are the standard deviations of X and Y, respectively. Note, however, that first, $\rho_{X,Y}$ depends on the binning method of the data, and second, it is a measure of linear dependence only. Again, for compactness, we define

$$\rho \equiv \rho_{\Delta_{n_{1,\alpha\alpha}}, \Delta_{C^2_\alpha}}. \tag{4.23}$$

The results are shown in Figs. 4.6 (g) and (h) with the corresponding fit results listed in Table A.2.

We observe that for the bulk of the range of N, both I and ρ decrease with increasing N. However, both quantities appear to increase for $N = 9$. Nevertheless, this could be an effect of small N, as the data points for both odd and even N separately exhibit monotonically decreasing behavior for $N \geq 3$. Both quantities appear to approach zero exponentially. Recall, however, that both depend on the binning method, Moreover, ρ is a measure of linear correlation only. Nonetheless, for a more robust statement, the data of I and ρ for larger values of N would need to be considered. It would then be possible to make a more refined statement whether these quantities approach zero in the large-N limit.

We remark that the conditions of the mechanism (i) of [55] and the ERH require the fluctuations of the two observables to be *completely* uncorrelated. That is, any amount of correlation, provided it persists in the thermodynamic limit, would be sufficient to conclude that these two mechanisms are not applicable. To test this, for each N we perform a hypothesis test on the data sets $\Delta_{n_{1,\alpha\alpha}}$ and $\Delta_{C^2_\alpha}$ with the null hypothesis H_0 that the values of these quantities are independent, and an alternative hypothesis H_a that they are not. The significance level α is set equal to 0.05. Each independence test returns a p-value, short for probability value p. Only if the p-value is less than the chosen significance level α, is the null hypothesis to be rejected at the chosen level of significance. The results are presented in Fig. 4.7.

We observe that except for the data points for $N = 2$ and $N = 8$ in the Blomqvist β independence test in Fig. 4.7 (a), all points lie below the chosen significance level of $\alpha = 0.05$. That is, at this significance level, the null hypothesis that the two sets of fluctuations $\Delta_{n_{1,\alpha\alpha}}$ and $\Delta_{C^2_\alpha}$ are uncorrelated is rejected. Moreover, for the majority of the independence tests, in the bulk of the range, there appears to be a trend for the p-value to decrease with greater N. Therefore, we can hypothesize that for larger N the two sets of fluctuations become more correlated. That is, with larger N there is more bias of the C^2_α's towards $n_{1,\alpha\alpha}$'s with greater deviation from the mean. We therefore conclude that the weak ETH is not applicable to our case.

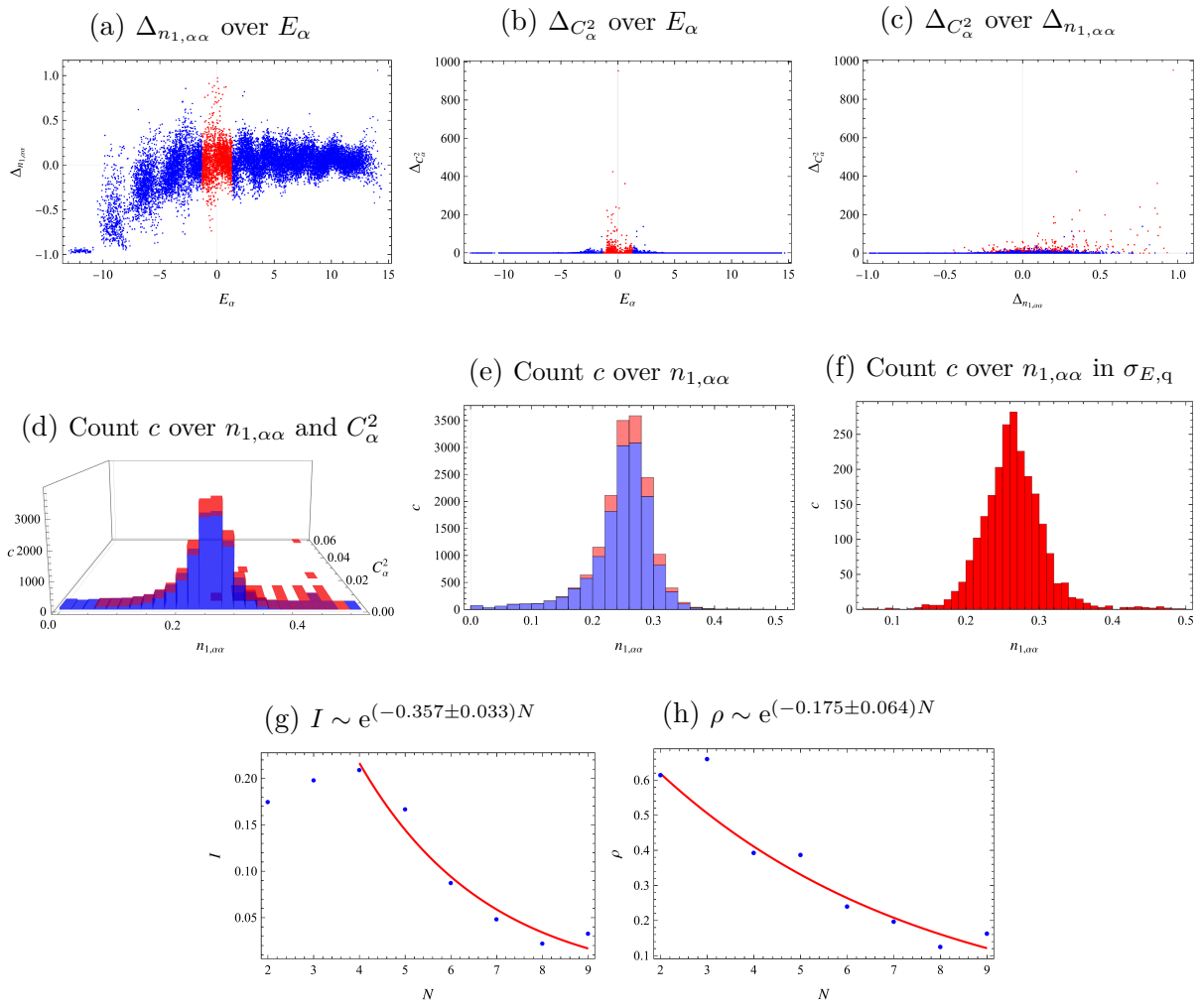

Figure 4.6: Thermalization despite correlation. The individual subfigures show: (a) an exemplary plot of $\Delta_{n_{1,\alpha\alpha}}$ over E_α for $N = 8$, (b) an exemplary plot of $\Delta_{C^2_\alpha}$ over E_α for $N = 8$, (c) an exemplary plot of $\Delta_{C^2_\alpha}$ over $\Delta_{n_{1,\alpha\alpha}}$ for $N = 8$, (d) an exemplary histogram of count c over $n_{1,\alpha\alpha}$ and C^2_α for $N = 8$, (e) an exemplary histogram of count c over $n_{1,\alpha\alpha}$ for $N = 8$, (f) an exemplary histogram of count c over $n_{1,\alpha\alpha}$ within $\sigma_{E,\mathrm{q}}$ for $N = 8$, (g) the mutual information I of $\Delta_{n_{1,\alpha\alpha}}$ and $\Delta_{C^2_\alpha}$ over N, (h) the Pearson correlation coefficient ρ between $\Delta_{n_{1,\alpha\alpha}}$ and $\Delta_{C^2_\alpha}$ over N. In subfigures (a), (b) and (c) the points within the microcanonical energy window are marked in red, the rest are marked in blue. Likewise, in subfigure (d) the bins corresponding to points within the microcanonical energy window are marked in red and the rest are marked in blue. The bins over identical $n_{1,\alpha\alpha}$ and C^2_α are stacked for the sake of clarity. Similarly, in subfigure (e) the bins corresponding to points within the microcanonical energy window are marked in red and the rest are marked in blue, with the bins over identical $n_{1,\alpha\alpha}$ stacked as well. In subfigures (g) and (h) the numerical data is represented by points and the corresponding fits are depicted by solid lines. The fit of $I(N)$ was performed only over the data points with $N \geq 4$. For $\rho(N)$ the data point $N = 3$ was excluded from the fit.

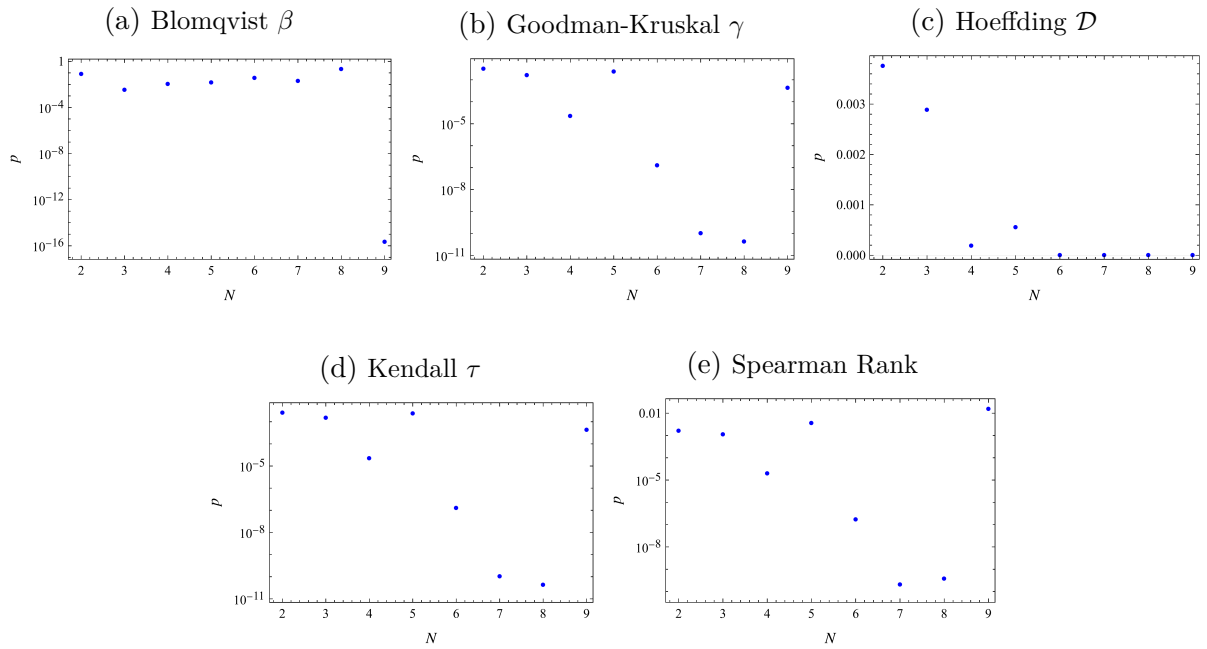

Figure 4.7: The p-value plotted over N for various independence tests for $\Delta_{n_{1,\alpha\alpha}}$ and $\Delta_{C^2_\alpha}$. The panels and the corresponding tests are: (a) Blomqvist β, (b) Goodman-Kruskal γ, (c) Hoeffding $\mathcal{D}$, (d) Kendall τ, (e) Spearman Rank. The Pearson Correlation, Pillai Trace and Wilks $\mathcal{W}$ independence tests were not applicable. Note the logarithmic scale for p in panels (a), (b), (d) and (e). For the test in panel (c), the values of the data points for $N \geq 6$ were lower than numerical accuracy and were returned as zero. Except for the two data points corresponding to $N = 2$ and $N = 8$ in (a), all data points lie clearly below the significance level of $\alpha = 0.05$.

Note that altering the conditions of the mechanisms to, for example, consider only the eigenstates with E_α within the microcanonical energy shell will, most likely, not reduce the amount of correlation. Specifically, the points within that energy window appear to be more correlated (see Fig. 4.6 (c)). We therefore expect that excluding these will only increase the correlation between the fluctuations. We conclude that our system thermalizes not via the mechanism (i) of [55] or the ERH, but instead by a new mechanism.

4.6 Discussion

4.6.1 A new thermalization mechanism

As discussed in Sec. 4.1.1, the only two conditions required for the few-body observable $\hat{A}$ to thermalize within an isolated N-body system evolved from a non-equilibrium state are that

(i)

$$\sum_\alpha |C_\alpha|^2 A_{\alpha\alpha} = \frac{1}{\mathcal{N}_{\sigma_\mathrm{w}}} \sum_{\substack{\alpha \\ |\overline{E}-E_\alpha|<\sigma_\mathrm{w}}} A_{\alpha\alpha} \text{ for an appropriate energy window } \sigma_\mathrm{w}, \text{ and} \tag{4.24}$$

(ii)

$$\sigma_t = \left[\sum_{\substack{\alpha,\beta \\ \alpha\neq\beta}} |C_\alpha|^2 |C_\beta|^2 |A_{\alpha\beta}|^2 \right]^{1/2} \text{ is small at most later times.} \tag{4.25}$$

Here, $\mathcal{N}_{\sigma_\mathrm{w}}$ denotes the number of eigenstates with eigenenergies E_α that lie within the microcanonical energy window $(\overline{E}-\sigma_\mathrm{w}, \overline{E}+\sigma_\mathrm{w})$. How specifically these are achieved does not influence the validity of the result. That is, there may exist fluctuations in $A_{\alpha\alpha}$ and/or $|C_\alpha|^2$, however large and correlated, and the observable may still thermalize. Ultimately, it not surprising that there are correlations between the distributions of the two quantities: $A_{\alpha\alpha} = \langle\alpha|\,\hat{A}\,|\alpha\rangle$ and $C_\alpha = \langle\alpha|\mathrm{in}\rangle$ are both computed from the same eigenvectors $|\alpha\rangle$ of the system.

Naturally, the simpler the additional conditions on the coefficients and the matrix elements are, the more elegant and intuitive the thermalization mechanism is, such as the ETH. Nevertheless, the ETH conditions, although sufficient for thermalization, are not a necessary set of conditions, as demonstrated by the various mechanisms mentioned previously as well as many others. One of the goals of this chapter is to provide a new variant of thermalization conditions. Namely, that despite the fact that the observable thermalizes, there may still exist correlations between the quantities from which the value of the same thermalized observable is calculated.

To summarize, we considered the observable $\hat{n}_1$ in the system of Eq. (3.6), evolved from the initial state in Eq. (3.5). We provided numerical evidence that this observable approaches thermalization in the thermodynamic limit according to the definition in Sec. 4.1.1. That is, the infinite-time average of the expectation value of the observable is equal to its microcanonical average and the temporal fluctuations of the observable about the microcanonical average are small at most later times in the limit of large N.

We find that the initial state is a superposition of eigenstates that are sufficiently close in energy, with the quantum energy uncertainty $\sigma_{E,\mathrm{q}}$ vanishing relative to the half-range of all eigenenergies ΔE in the thermodynamic limit. This fulfills ETH condition (0). The average absolute value of the off-diagonal elements $n_{1,\alpha\beta}$ decays exponentially to zero with increasing N, thus fulfilling ETH condition (2). This ensures that the thermalization condition (ii) on the temporal fluctuations of the observable is satisfied.

However, we find that the diagonal elements $n_{1,\alpha\alpha}$ do not vary smoothly over E_α, exhibiting large fluctuations instead. Moreover, the maximal difference between neighboring diagonal elements within the microcanonical energy window approaches a value slightly larger than that of the microcanonical ensemble average $n_{1,\mathrm{mc}}$ itself. Therefore, the ETH condition (1) is not fulfilled, as well as similar requirements in other thermalization mechanisms. Furthermore, the weak ETH, the mechanism (i) of [55] and the ERH are also not responsible for thermalization in our case, as the fluctuations $\Delta_{n_{1,\alpha\alpha}}$ and $\Delta_{C_\alpha^2}$ are correlated, with few diagonal elements $n_{1,\alpha\alpha}$ that are farther from and greater than their mean biased towards by the C_α^2's. Nevertheless, $\overline{n}_1 = n_{1,\mathrm{mc}}$ still holds, as on the left-hand side the fluctuations of the two quantities are correlated in such a way that the many diagonal elements $n_{1,\alpha\alpha} < n_{1,\mathrm{av}}$ which have smaller weights counteract the above bias collectively and balance it out, while on the right-hand side the diagonal elements within the microcanonical energy window average out to $n_{1,\mathrm{mc}}$, see Figs. 4.6 (d), (e) and (f). This fulfills condition (i) of thermalization. It is important to note that both the large fluctuations of $n_{1,\alpha\alpha}$ and the strong bias of the coefficients towards them persist in the thermodynamic limit. Therefore, $\overline{n}_1 = n_{1,\mathrm{mc}}$ is fulfilled precisely because of the specific distribution of the fluctuations of the two quantities and the way they are correlated.

As the expression $\overline{n}_1 = n_{1,\mathrm{mc}}$ is the only requirement needed to fulfill thermalization condition (i), we can allow for an arbitrary amount of bias in calculating its left-hand side, as long as the equality holds. Moreover, many variations of the mechanism, complementary to the version presented above, are possible. For example, alternatively, the few diagonal elements that are farther from and *smaller* than their mean could be biased towards by the C_α^2's. Or, in a further variation, the diagonal elements that deviate strongly from the mean in general could be biased towards by the coefficients. The latter variant would allow for many diagonal elements to exhibit large fluctuations. In this case the fraction of the non-thermal states would not vanish in the thermodynamic limit, however with an appropriately correlated distribution of C_α^2's, $\overline{n}_1 = n_{1,\mathrm{mc}}$ could still be achieved. Note that then δ_1 and $\delta_{1,\mathrm{mc}}$ would not vanish in the large-N limit, in contrast to the results shown in Figs. 4.4 (c) and (d). An intriguing question is whether it would be possible to arrange for a system and an observable with such fluctuations in the respective quantities, that it would thermalize for a finite-size, instead of in the large-N limit.

Consequently, two natural questions arise here: First, what is the maximum amount of bias allowed for the observable to still be able to thermalize? And second, how much control of the correlations do we realistically have? In principle, the fluctuations can be maximally correlated, as long as the thermalization conditions (i) and (ii) are fulfilled. However, for the black hole scaling regime, the number of free parameters that we can control for a given system realization in Eq. (3.6) is $N(2N-1) \sim \mathcal{O}(N^2)$ couplings, whereas the dimension of the Hilbert space grows exponentially with N. It therefore becomes unlikely for us to have full control of the distributions of the two quantities in the large-N limit.

Regarding thermalization in isolated quantum systems, we have achieved two goals: First, we proposed a new thermalization mechanism and demonstrated it on a specific model in which observables could thermalize via this mechanism where $\Delta_{n_{1,\alpha\alpha}}$ and $\Delta_{C_\alpha^2}$ are allowed to be co-dependent. Second, this provides an indication that there could exist a thermalization mechanism that would operate on a set of more general conditions on the coefficients and the diagonal elements.

4.6.2 Application to black holes

Regarding black holes, our results may provide further insight into how these objects process information. Building on previous works, this can help us to improve the formulations of old hypotheses and to define new ones, which may be testable for real black holes. Based on the prototype model of Eq. (3.6), we have suggested a possible mechanism of how the information stored within the memory modes of a black hole may spread out and thermalize. This improves our understanding of the interior information dynamics of a black hole at a microscopic level. If however, we find evidence that black holes are supposed to thermalize via a different mechanism, such as, for example, the ETH, this would allow us to modify the prototype model accordingly and refine our understanding of the corresponding processes at a quantum level.

4.7 Summary

In this chapter we have proposed a novel thermalization mechanism for few-body observables in isolated quantum many-body systems. We have based our arguments on the numerical analysis of finite-size scaling of a quantum prototype system of enhanced memory capacity designed to model the information processing properties of a black hole. We have found that the infinite-time averages of the occupation number operators of the information carrying modes within this model approach their respective microcanonical ensemble averages in the thermodynamic limit and thus thermalize.

The key novelty of the proposed mechanism is that the diagonal matrix elements $A_{\alpha\alpha}$ of a few-body observable $\hat{A}$ in the eigenstate basis $\{|\alpha\rangle\}$ and the squared coefficients C_α^2 fluctuate considerably, but not randomly. Instead, these two sets of fluctuations are correlated to such an extent, that the null hypothesis that they are independent is rejected at 0.05 significance level in favor of the alternative hypothesis that they are co-dependent. Therefore,

the infinite-time average, expressed in the diagonal ensemble as $\overline{\langle \hat{A}(t) \rangle} = \sum_\alpha |C_\alpha|^2 A_{\alpha\alpha}$, is performed with a bias. That is, the various diagonal elements $A_{\alpha\alpha}$ in the sum possess weights $|C_\alpha|^2$ that are not randomly assigned. However, the equality between the infinite-time and the microcanonical ensemble averages, $\overline{\langle \hat{A}(t) \rangle} = A_{\mathrm{mc}}$, still holds, and as that is the only criterion we demand for $\overline{\langle \hat{A}(t) \rangle}$ to fulfill, the amount of bias is irrelevant. The above equality is achieved due to the specific form of the distributions of both the diagonal elements and the coefficients. Namely, on the left-hand side of the above equality, the few diagonal elements much larger than their average are biased towards by the higher values of the coefficients-squared. Nevertheless, the fluctuations and the correlations are such, that the smaller diagonal elements with smaller weights $|C_\alpha|^2$ counterbalance the above bias collectively. At the same time, on the right-hand side, the diagonal elements within the microcanonical energy window average out to A_{mc}. As mentioned previously, further variations of this mechanism are possible.

An additional feature is that the prototype model in Eq. (3.6) could potentially be realized in ultracold atom experiments [106–109], as was previously suggested in [34] among other works. The experimental actualization of this system would possibly allow the above thermalization mechanism, as well as the other information-processing phenomena predicted in previous works, to be tested. This is an especially interesting prospect, as first, the corresponding enhanced memory capacity model would be realized in the realistic setting of large occupation numbers $N \gg 1$, and second, the various hypothesized effects could be tested in real laboratory experiments on systems of ultracold quantum gases. Moreover, this could open a window to be able to observe new phenomena, which could lead to new testable hypotheses for black hole physics. This direction of research appears to be promising, as the prototype model in Eq. (3.6) is quite similar to the Bose-Hubbard model (BHM) [110,111], which has been successfully realized experimentally (see references above). Namely, to realize the above prototype model, the following modifications of the BHM would have to be made: First, two sites would have to be singled out as the master mode $\hat{a}$ and the external mode $\hat{b}$, and second, the hopping amplitude, the on-site interaction and the chemical potential within the BHM would have to be tuned separately for the individual sites. The memory modes do not necessarily have to be truncated to qubits. Finally, a further interesting question is whether the nearest-neighbor hopping interactions would suffice to replicate the general behavior of the prototype model, or if the memory modes necessarily need to possess direct all-to-all couplings.

Chapter 5

Conclusions and Outlook

In this dissertation we studied the information processing and storing properties of black holes. We addressed the task from two different perspectives: First, we considered a renormalizable $SU(N)$-invariant theory of a scalar field in $(3 + 1)$ space-time dimensions from [22], given in Eq. (2.12). We demonstrated that the spectrum of this theory contains a tower of vacuum bubbles that represent self-sustained bound states of $SU(N)$ Goldstone bosons. Despite the absence of gravity in the theory, there exist certain vacuum bubbles that exhibit the information-processing properties of black holes. As has been proposed recently [20–22], such objects are called "saturons", as they saturate the entropy bounds of Eqs. (2.1) and (2.2) set by unitarity in the respective theories. Second, we considered a specific quantum prototype model of enhanced memory capacity (that is, it can store large amounts of information) of [35], given in Eq. (3.6). This microscopic model was designed according to the quantum N-portrait of a black hole [14], in which a black hole is viewed as a bound state of weakly interacting soft gravitons. Within the framework of the quantum prototype model of Eq. (3.6) we investigated the dynamics of the system and how it processes the information that it contains. Let us elaborate on the findings of the two respective directions.

First, in chapter 2, which is based on [1], we obtained supportive evidence for the proposition of [22] in a specific setting of the theory in Eq. (2.12). The entropy of the vacuum bubbles within this theory obeys the unitarity bounds of Eqs. (2.1) and (2.2). Moreover, a saturated bubble exhibits the exact same properties as those of a black hole: Its entropy is given by the Bekenstein-Hawking area-law formula; semiclassically, the bubble possesses a strict information horizon and evaporates at a thermal rate with a temperature set by its inverse radius; and the timescale of information retrieval is similar to the Page time. This establishes a further concrete example of the black hole–saturon correspondence. This underlying connection is best described via the trans-theoretic notion of a Goldstone boson of spontaneously broken Poincaré symmetry. The above properties, written in terms of the universal quantities of the corresponding Goldstone coupling $G_{\rm Gold}$ or the dimensionless effective Goldstone coupling $\alpha_{\rm Gold} = G_{\rm Gold}/Area$ have the same respective expressions for a black hole and a saturated bubble.

Another universal phenomenon that we observed at play is that of memory burden [30,

35], which occurs generically in systems of enhanced memory capacity. Via this effect the quantum information stored within such a system is able to stabilize it and prevent it from leaving a state of enhanced memory capacity. Other works have previously suggested that black holes are so long-lived because of the memory burden effect. Within the framework of the $SU(N)$ theory we have demonstrated the influence of this effect on the time-evolution and stability of vacuum bubbles. Specifically, a bubble is stabilized because it is energetically more favorable to contain the quantum information stored in terms of the occupation numbers of the massless Goldstone modes within it, than in excitations of the asymptotic quanta of the exterior vacuum with a nonzero energy gap.

Next, in chapter 3, based on [2], we considered a specific example of a microscopic prototype system with enhanced memory capacity from [35], designed to model the information-processing characteristics of a black hole. For this model, given in Eq. (3.6), we considered its early-time dynamics on timescales smaller than scrambling [36, 37]. Due to this phenomenon of scrambling, the information contained within the system is "mixed up" despite the unitary time-evolution of its state. That is, the information originally contained only in the initial state gradually diffuses over the entire Hilbert space. Studying the "prescrambling" regime of the system we defined a corresponding measure for the diffusion of the state in terms of a minimum probability threshold for the states in the system's Hilbert space. This measure is independent of the specific definition of scrambling. From our findings we proposed a series of conjectures, similar to those of [37]. In particular, these include that the most rapid prescramblers take a time logarithmic in the number of degrees of freedom, that the model in Eq. (3.6) is a fast prescrambler and that black holes are fast prescramblers. That is, we observe that, at the level of prescrambling, the considered prototype model fulfills the requirements on scrambling for a black hole.

Last, in chapter 4 we studied how the same prototype model thermalizes. Specifically, for this system, prepared in a pure initial state far from equilibrium, we found an explicit mechanism by which under unitary time-evolution few-body observables equilibrate to their respective microcanonical ensemble averages. This result is twofold: On the one hand it proposes a new microscopic mechanism by which isolated quantum many-body systems thermalize. On the other hand, it suggests a mechanism via which the prototype model of a black hole in Eq. (3.6) thermalizes. This allows us to adapt and fine-tune our microscopic models of black holes according to any additional information that we may obtain on thermalization within astrophysical black holes.

In our analysis we provide evidence that the investigated system does not thermalize via the mechanisms reviewed in chapter 4, including the Eigenstate Thermalization Hypothesis [44, 45], but instead via a different mechanism. The novelty is in thermalization despite correlations between the fluctuations of the eigenstate expectation values of a few-body observable and the fluctuations of the coefficients-squared $|C_\alpha|^2$.

In total, this thesis contributes to the general program of improving the understanding of the behavior of physical black holes in two ways. First, by providing a further specific example of the black hole–saturon correspondence we strengthen the evidence that the above information-processing features are not specific to black holes or gravity. Our results support the idea that instead the fundamental origin of these properties for generic

saturons within a given theory lies in the theory's saturation of its unitarity bound. Second, we provide supporting evidence of new phenomena for black hole physics. These include the memory burden effect, prescrambling and the proposed novel thermalization mechanism. Although it may currently be challenging to test these on astrophysical black holes, performing corresponding experiments on ultracold bosonic systems in laboratory settings that are available today appears to be a promising direction of research and an achievable task.

As an outlook we mention two projects that are in preparation. The first [4] expands on vortex formation in black holes and saturons [26]. The formation and stability of vortices in black holes may have significant observational implications for astrophysical black holes. The second [5] studies the saturation of entropy by *vortons*: Stable configurations of superconducting strings [112, 113]. The production of stable vortons at a high energy phase transition can have a substantial effect on the predictions of standard cosmology. Meanwhile, their formation at lower energies can contribute to the dark matter content of the universe [114].

Appendix A

Tables of Fit Functions

t_f	$\overline{R}^2$	RMSE	a	σ_a	b	σ_b	c	σ_c
$a + b\ln(N)$	$9.9991 \cdot 10^{-1}$	$6.00 \cdot 10^{-2}$	-9.645	$4.3 \cdot 10^{-2}$	3.6420	$9.8 \cdot 10^{-3}$	n/a	n/a
$a + b\ln(K)$	$9.88 \cdot 10^{-1}$	$4.80 \cdot 10^{-2}$	$1.97 \cdot 10^{-1}$	$2.8 \cdot 10^{-2}$	$7.92 \cdot 10^{-2}$	$8.8 \cdot 10^{-3}$	n/a	n/a
$a + b\exp(cN_m)$	$9.77 \cdot 10^{-1}$	$2.86 \cdot 10^{-1}$	$-1.3 \cdot 10^{-1}$	$4.3 \cdot 10^{-1}$	$1.9 \cdot 10^{-1}$	$1.9 \cdot 10^{-1}$	$4.3 \cdot 10^{-1}$	$1.3 \cdot 10^{-1}$
$a + b\exp(c\Delta)$	$9.9996 \cdot 10^{-1}$	$2.44 \cdot 10^{-3}$	$3.183 \cdot 10^{-1}$	$1.0 \cdot 10^{-3}$	$7.7 \cdot 10^{-6}$	$2.7 \cdot 10^{-6}$	2.373	$8.7 \cdot 10^{-2}$
$a + bC_b^c$	$9.98 \cdot 10^{-1}$	$7.81 \cdot 10^{-2}$	$1.76 \cdot 10^{-1}$	$3.8 \cdot 10^{-2}$	$7.2 \cdot 10^{-3}$	$2.2 \cdot 10^{-3}$	-1.177	$5.9 \cdot 10^{-2}$
$a + bC_m^c$	$9.9993 \cdot 10^{-1}$	$6.10 \cdot 10^{-3}$	$5.34 \cdot 10^{-2}$	$7.5 \cdot 10^{-3}$	$1.086 \cdot 10^{-1}$	$4.1 \cdot 10^{-3}$	$-3.847 \cdot 10^{-1}$	$5.1 \cdot 10^{-3}$

t_c	$\overline{R}^2$	RMSE	a	σ_a	b	σ_b	c	σ_c
$a + bN^c$	$9.996 \cdot 10^{-1}$	$4.52 \cdot 10^{-2}$	$9.25 \cdot 10^{-1}$	$5.9 \cdot 10^{-2}$	22.9	1.9	$-9.66 \cdot 10^{-1}$	$4.4 \cdot 10^{-2}$
$a + b\exp(cK)$	$9.94 \cdot 10^{-1}$	$3.97 \cdot 10^{-1}$	3.54	$3.2 \cdot 10^{-1}$	19.2	6.3	$-8.3 \cdot 10^{-2}$	$1.9 \cdot 10^{-2}$
$a + b\exp(c\Delta)$	$9.99994 \cdot 10^{-1}$	$1.69 \cdot 10^{-2}$	8.205	$7.2 \cdot 10^{-2}$	-2.662	$5.3 \cdot 10^{-2}$	$-3.23 \cdot 10^{-1}$	$1.9 \cdot 10^{-2}$
$a + bC_b^c$	$9.991 \cdot 10^{-1}$	$7.01 \cdot 10^{-2}$	$9.72 \cdot 10^{-1}$	$7.2 \cdot 10^{-2}$	$3.9 \cdot 10^{-3}$	$2.7 \cdot 10^{-3}$	-4.41	$4.8 \cdot 10^{-1}$
$a + bC_m^c$	$9.9998 \cdot 10^{-1}$	$5.55 \cdot 10^{-2}$	$3.0 \cdot 10^{-2}$	$4.7 \cdot 10^{-2}$	$5.288 \cdot 10^{-1}$	$9.4 \cdot 10^{-3}$	-1.0734	$4.4 \cdot 10^{-3}$

Table A.1: Tables of best obtained fit functions for the numerical analysis of prescrambling in chapter 3. The tables of fit functions for t_f and t_c are on the top and bottom, respectively. The corresponding coefficients of determination $\overline{R}^2$ and unbiased root-mean-square errors (RMSE) are both adjusted for the number of fit-model parameters. The values of the free fit-model parameters are given with the corresponding standard errors. No dependence of t_c on N_m could be extracted from the corresponding data points.

Object	$\overline{R}^2$	RMSE	a	σ_a	b	σ_b	c	σ_c
* $\overline{n}_1(N) = a + b\exp(cN)$	$9.966 \cdot 10^{-1}$	$1.96 \cdot 10^{-2}$	$2.7 \cdot 10^{-1}$	$1.5 \cdot 10^{-1}$	$1.5 \cdot 10^{-1}$	$1.1 \cdot 10^{-1}$	$-1.4 \cdot 10^{-1}$	$3.2 \cdot 10^{-1}$
$\overline{n}_1(N) = a + bN^{-1/2}$	$9.968 \cdot 10^{-1}$	$1.91 \cdot 10^{-2}$	$2.58 \cdot 10^{-1}$	$2.8 \cdot 10^{-2}$	$1.78 \cdot 10^{-1}$	$6.1 \cdot 10^{-2}$	n/a	n/a
* $n_{1,\mathrm{mc}}(N) = a + b\exp(cN)$	$9.998 \cdot 10^{-1}$	$3.47 \cdot 10^{-3}$	$2.53 \cdot 10^{-1}$	$1.5 \cdot 10^{-2}$	$7.9 \cdot 10^{-2}$	$1.0 \cdot 10^{-2}$	$-2.5 \cdot 10^{-1}$	$1.6 \cdot 10^{-1}$
$n_{1,\mathrm{mc}}(N) = a + bN^{-1}$	$9.997 \cdot 10^{-1}$	$4.56 \cdot 10^{-3}$	$2.538 \cdot 10^{-1}$	$4.7 \cdot 10^{-3}$	$9.5 \cdot 10^{-2}$	$1.6 \cdot 10^{-2}$	n/a	n/a
$n_{1,\mathrm{mc}}(N) = a + bN^{-1/2}$	$9.999 \cdot 10^{-1}$	$3.33 \cdot 10^{-3}$	$2.273 \cdot 10^{-1}$	$6.3 \cdot 10^{-3}$	$1.04 \cdot 10^{-1}$	$1.2 \cdot 10^{-2}$	n/a	n/a
$\sigma_{1,t}(N) = a + b\exp(cN)$	$9.96 \cdot 10^{-1}$	$5.45 \cdot 10^{-3}$	$8.9 \cdot 10^{-3}$	$9.9 \cdot 10^{-3}$	$4.10 \cdot 10^{-1}$	$4.7 \cdot 10^{-2}$	$-4.70 \cdot 10^{-1}$	$7.4 \cdot 10^{-2}$
* $\sigma_{E,\mathrm{q}}(N) = a + bN^{-1}$	$9.9990 \cdot 10^{-1}$	$1.36 \cdot 10^{-2}$	1.378	$1.0 \cdot 10^{-2}$	$-1.60 \cdot 10^{-1}$	$3.9 \cdot 10^{-2}$	n/a	n/a
$\sigma_{E,\mathrm{q}}(N) = a + bN^{-1/2}$	$9.9989 \cdot 10^{-1}$	$1.45 \cdot 10^{-2}$	1.416	$2.1 \cdot 10^{-2}$	$-1.62 \cdot 10^{-1}$	$4.3 \cdot 10^{-2}$	n/a	n/a
$\sigma_{E,\mathrm{q}}(N) = a + b\exp(cN)$	$9.9989 \cdot 10^{-1}$	$1.43 \cdot 10^{-2}$	1.3536	$7.6 \cdot 10^{-3}$	$-4.1 \cdot 10^{-1}$	$4.9 \cdot 10^{-1}$	$-9.4 \cdot 10^{-1}$	$5.9 \cdot 10^{-1}$
$\sigma_{E,\mathrm{q}}(N) = a + bN^c$	$9.9989 \cdot 10^{-1}$	$1.42 \cdot 10^{-2}$	1.359	$1.5 \cdot 10^{-2}$	$-2.7 \cdot 10^{-1}$	$2.6 \cdot 10^{-1}$	-2.0	1.5
* $\mathcal{N}_{\sigma_{E,\mathrm{q}}}(N) = a + b\exp(cN)$	$9.75 \cdot 10^{-1}$	248	-107	160	6.7	7.4	$7.1 \cdot 10^{-1}$	$1.2 \cdot 10^{-1}$
$\mathcal{N}_{\sigma_{E,\mathrm{q}}}(N) = a + bN^c$	$9.80 \cdot 10^{-1}$	221	-34	118	$9 \cdot 10^{-3}$	$1.6 \cdot 10^{-2}$	5.93	$8.5 \cdot 10^{-1}$
* $\Delta E(N) = a + bN^c$	$9.97 \cdot 10^{-1}$	$5.60 \cdot 10^{-1}$	0.9	1.3	$7.4 \cdot 10^{-1}$	$4.7 \cdot 10^{-1}$	1.35	$2.6 \cdot 10^{-1}$
$\Delta E(N) = a + b\exp(cN)$	$9.97 \cdot 10^{-1}$	$5.69 \cdot 10^{-1}$	-19	21	19	20	$6.4 \cdot 10^{-2}$	$4.9 \cdot 10^{-2}$
* $\sigma_{E,\mathrm{q}}/\Delta E(N) = a + bN^{-1/2}$	$9.96 \cdot 10^{-1}$	$1.59 \cdot 10^{-2}$	$-2.53 \cdot 10^{-1}$	$2.3 \cdot 10^{-2}$	$9.97 \cdot 10^{-1}$	$4.7 \cdot 10^{-2}$	n/a	n/a
$\sigma_{E,\mathrm{q}}/\Delta E(N) = a + b\exp(cN)$	$9.96 \cdot 10^{-1}$	$1.44 \cdot 10^{-2}$	$6.4 \cdot 10^{-2}$	$1.9 \cdot 10^{-2}$	$8.43 \cdot 10^{-1}$	$7.6 \cdot 10^{-2}$	$-3.85 \cdot 10^{-1}$	$5.3 \cdot 10^{-2}$
$\sigma_{E,\mathrm{q}}/\Delta E(N) = a + bN^c$	$9.95 \cdot 10^{-1}$	$1.72 \cdot 10^{-2}$	$-1.8 \cdot 10^{-1}$	$1.7 \cdot 10^{-1}$	$9.55 \cdot 10^{-1}$	$9.2 \cdot 10^{-2}$	$-5.9 \cdot 10^{-1}$	$2.4 \cdot 10^{-1}$
$\sigma_{E,\mathrm{q}}/\Delta E(N) = a + bN^{-1}$	$9.93 \cdot 10^{-1}$	$2.00 \cdot 10^{-2}$	$-1.0 \cdot 10^{-2}$	$1.5 \cdot 10^{-2}$	$9.59 \cdot 10^{-1}$	$5.7 \cdot 10^{-2}$	n/a	n/a
$n_{1,\mathrm{av}}(N) = a + bN^{-1}$	1.	$4.45 \cdot 10^{-16}$	$2.5 \cdot 10^{-1}$	$5.6 \cdot 10^{-16}$	$-2.5 \cdot 10^{-1}$	$2.6 \cdot 10^{-15}$	n/a	n/a
$\delta_1(N) = a + b\exp(cN)$	$9.98 \cdot 10^{-1}$	$1.74 \cdot 10^{-2}$	$-2 \cdot 10^{-2}$	$7.9 \cdot 10^{-1}$	1.7	1.9	$-2.9 \cdot 10^{-1}$	$6.6 \cdot 10^{-1}$
$\delta_{1,\mathrm{mc}}(N) = a + b\exp(cN)$	$9.99 \cdot 10^{-1}$	$1.31 \cdot 10^{-2}$	$-5 \cdot 10^{-1}$	8.2	1.5	6.9	$-1.0 \cdot 10^{-1}$	$8.9 \cdot 10^{-1}$
* $\delta_{1,\max}^{\mathrm{mc}}(N) = a + bN^c$	$9.99995 \cdot 10^{-1}$	$3.00 \cdot 10^{-3}$	1.0442	$9.2 \cdot 10^{-3}$	1.620	$4.1 \cdot 10^{-2}$	-1.451	$5.5 \cdot 10^{-2}$
$\delta_{1,\max}^{\mathrm{mc}}(N) = a + b\exp(cN)$	$9.9998 \cdot 10^{-1}$	$5.44 \cdot 10^{-3}$	1.1157	$6.3 \cdot 10^{-3}$	1.831	$9.3 \cdot 10^{-2}$	$-6.29 \cdot 10^{-1}$	$2.8 \cdot 10^{-2}$
$\mu_{\lvert n_{1,\alpha\beta}\rvert}^{\alpha\neq\beta}(N) = a + b\exp(cN)$	$9.94 \cdot 10^{-1}$	$2.49 \cdot 10^{-3}$	$-5 \cdot 10^{-4}$	$2.8 \cdot 10^{-3}$	$2.66 \cdot 10^{-1}$	$4.0 \cdot 10^{-2}$	$-6.54 \cdot 10^{-1}$	$8.2 \cdot 10^{-2}$
$I(N) = a + \exp(bN)$	$9.80 \cdot 10^{-1}$	$1.67 \cdot 10^{-2}$	$-2.4 \cdot 10^{-2}$	$2.2 \cdot 10^{-2}$	$-3.57 \cdot 10^{-1}$	$3.3 \cdot 10^{-2}$	n/a	n/a
$\rho(N) = a + \exp(bN)$	$9.88 \cdot 10^{-1}$	$3.79 \cdot 10^{-2}$	$-9 \cdot 10^{-2}$	$1.2 \cdot 10^{-1}$	$-1.75 \cdot 10^{-1}$	$6.4 \cdot 10^{-2}$	n/a	n/a

Table A.2: Table of best obtained fit functions for the numerical analysis of thermalization in chapter 4. The corresponding coefficients of determination $\overline{R}^2$ and unbiased root-mean-square errors (RMSE) are both adjusted for the number of fit-model parameters. The values of the free fit-model parameters are given with the corresponding standard errors. The fits plotted in the figures of chapter 4 are marked with a "*". For $\overline{n}_1(N)$ the data point $N = 3$ was excluded from the fits. The fits of $n_{1,\mathrm{mc}}(N)$ were performed only over the data points with even N. The fit of $n_{1,\mathrm{av}}(N)$ was performed only over the data points with odd N. The fit of $\delta_1(N)$ was a weighted fit with weights $\sigma_1^{-2}(N)$ and was performed only over the data points with even N. The fit of $\delta_{1,\mathrm{mc}}(N)$ was a weighted fit with weights $\sigma_{1,\mathrm{mc}}^{-2}(N)$ and was performed only over the data points with even N. The fits of $\delta_{1,\max;\mathrm{mc}}(N)$ were performed only over the data points with even N. The fit of $I(N)$ was performed only over the data points with $N \geq 4$. For $\rho(N)$ the data point $N = 3$ was excluded from the fit.

List of Figures

List of Tables

Bibliography

[1] G. Dvali, O. Kaikov, and J. S. Valbuena-Bermúdez, *How special are black holes? Correspondence with objects saturating unitarity bounds in generic theories*, Phys. Rev. D **105**, 056013 (2022).

[2] O. Kaikov, *Fast prescramblers*, Phys. Rev. D **107**, 116008 (2023).

[3] O. Kaikov, *Thermalization despite correlation*, in preparation.

[4] G. Dvali, O. Kaikov, F. Kühnel, and J. S. Valbuena-Bermúdez, in preparation.

[5] G. Dvali, O. Kaikov, H. Liu, and J. S. Valbuena-Bermúdez, in preparation.

[6] K. Schwarzschild, *Über das Gravitationsfeld eines Massenpunktes nach der Einsteinschen Theorie*, Sitzungsber. Königl. Preuss. Akad. Wiss. Berlin, Phys.-Math. Kl., 189 (1916), translated to English in arXiv:physics/9905030.

[7] J. Droste, *The field of a single centre in Einstein's theory of gravitation, and the motion of a particle in that field*, Koninkl. Ned. Akad. Wetenschap. Proc. **19**, 197 (1917), translated to English in https://dwc.knaw.nl/DL/publications/PU00012325.pdf.

[8] J. D. Bekenstein, *Black holes and entropy*, Phys. Rev. D **7**, 2333 (1973).

[9] S. W. Hawking, *Particle creation by black holes*, Commun. Math. Phys. **43**, 199 (1975).

[10] S. W. Hawking, *Black hole explosions?*, Nature **248**, 30 (1974).

[11] S. W. Hawking, *Breakdown of predictability in gravitational collapse*, Phys. Rev. D **14**, 2460 (1976).

[12] S. W. Hawking, *The unpredictability of quantum gravity*, Commun. Math. Phys. **87**, 395 (1982).

[13] G. Dvali, *Non-thermal corrections to Hawking radiation versus the information paradox*, Fortschr. Phys. **64**, 106 (2016).

[14] G. Dvali and C. Gómez, *Black hole's quantum N-portrait*, Fortschr. Phys. **61**, 742 (2013).

[15] G. Dvali and C. Gómez, *Black hole's* $1/N$ *hair*, Phys. Lett. B **719**, 419 (2013).

[16] G. Dvali and C. Gómez, *Black holes as critical point of quantum phase transition*, Eur. Phys. J. C **74**, 2752 (2014).

[17] G. Dvali and C. Gómez, *Black hole macro-quantumness*, arXiv:1212.0765.

[18] D. N. Page, *Particle emission rates from a black hole: Massless particles from an uncharged, nonrotating hole*, Phys. Rev. D **13**, 198 (1976).

[19] D. N. Page, *Information in black hole radiation*, Phys. Rev. Lett. **71**, 3743 (1993).

[20] G. Dvali, *Area law saturation of entropy bound from perturbative unitarity in renormalizable theories*, Fortschr. Phys. **69**, 2000090 (2021).

[21] G. Dvali, *Unitarity entropy bound: Solitons and instantons*, Fortschr. Phys. **69**, 2000091 (2021).

[22] G. Dvali, *Entropy bound and unitarity of scattering amplitudes*, J. High Energy Phys. 03 (2021) 126.

[23] G. Dvali and R. Venugopalan, *Classicalization and unitarization of wee partons in QCD and gravity: The CGC-black hole correspondence*, Phys. Rev. D **105**, 056026 (2022).

[24] G. Dvali, *Bounds on quantum information storage and retrieval*, Phil. Trans. A Math. Phys. Eng. Sci. **380**, 20210071 (2021).

[25] G. Dvali and O. Sakhelashvili, *Black-hole-like saturons in Gross-Neveu*, Phys. Rev. D **105**, 065014 (2022).

[26] G. Dvali, F. Kühnel, and M. Zantedeschi, *Vortices in black holes*, Phys. Rev. Lett. **129**, 061302 (2022).

[27] G. Dvali, *Saturon dark matter*, arXiv:2302.08353.

[28] J. D. Bekenstein, *Universal upper bound on the entropy-to-energy ratio for bounded systems*, Phys. Rev. D **23**, 287 (1981).

[29] G. Dvali, *Area law microstate entropy from criticality and spherical symmetry*, Phys. Rev. D **97**, 105005 (2018).

[30] G. Dvali, *A microscopic model of holography: Survival by the burden of memory*, arXiv:1810.02336.

[31] G. Dvali, *Critically excited states with enhanced memory and pattern recognition capacities in quantum brain networks: Lesson from black holes*, arXiv:1711.09079.

[32] G. Dvali, *Black holes as brains: Neural networks with area law entropy*, Fortschr. Phys. **66**, 1800007 (2018).

[33] G. Dvali, L. Eisemann, M. Michel, and S. Zell, *Universe's primordial quantum memories*, J. Cosmol. Astropart. Phys. 03 (2019) 010.

[34] G. Dvali, M. Michel, and S. Zell, *Finding critical states of enhanced memory capacity in attractive cold bosons*, Eur. Phys. J. Quantum Technol. **6**, 1 (2019).

[35] G. Dvali, L. Eisemann, M. Michel, and S. Zell, *Black hole metamorphosis and stabilization by memory burden*, Phys. Rev. D **102**, 103523 (2020).

[36] P. Hayden and J. Preskill, *Black holes as mirrors: Quantum information in random subsystems*, J. High Energy Phys. 09 (2007) 120.

[37] Y. Sekino and L. Susskind, *Fast scramblers*, J. High Energy Phys. 10 (2008) 65.

[38] L. Susskind, *Addendum to fast scramblers*, arXiv:1101.6048.

[39] D. N. Page, *Average entropy of a subsystem*, Phys. Rev. Lett. **71**, 1291 (1993).

[40] G. Dvali, A. Franca, C. Gómez, and N. Wintergerst, *Nambu-Goldstone effective theory of information at quantum criticality*, Phys. Rev. D **92**, 125002 (2015).

[41] G. Dvali, D. Flassig, C. Gómez, A. Pritzel, and N. Wintergerst, *Scrambling in the black hole portrait*, Phys. Rev. D **88**, 124041 (2013).

[42] G. Dvali, C. Gómez, D. Lüst, Y. Omar, and B. Richter, *Universality of black hole quantum computing*, Fortschr. Phys. **65**, 1600111 (2017).

[43] J. v. Neumann, *Beweis des Ergodensatzes und des H-Theorems in der neuen Mechanik*, Z. Phys. **57**, 30 (1929), translated to English in Eur. Phys. J. H **35**, 201 (2010).

[44] J. M. Deutsch, *Quantum statistical mechanics in a closed system*, Phys. Rev. A **43**, 2046 (1991).

[45] M. Srednicki, *Chaos and quantum thermalization*, Phys. Rev. E **50**, 888 (1994).

[46] M. Srednicki, *Does quantum chaos explain quantum statistical mechanics?*, arXiv:cond-mat/9410046.

[47] M. Srednicki, *Thermal fluctuations in quantized chaotic systems*, J. Phys. A **29**, L75 (1996).

[48] M. Srednicki, *The approach to thermal equilibrium in quantized chaotic systems*, J. Phys. A **32**, 1163 (1999).

[49] R. Nandkishore and D. A. Huse, *Many-body localization and thermalization in quantum statistical mechanics*, Ann. Rev. Cond. Matt. Phys. **6**, 15 (2015).

[50] C. Gogolin and J. Eisert, *Equilibration, thermalisation, and the emergence of statistical mechanics in closed quantum systems*, Rep. Prog. Phys. **79**, 056001 (2016).

[51] L. D'Alessio, Y. Kafri, A. Polovnikov, and M. Rigol, *From quantum chaos and eigenstate thermalization to statistical mechanics and thermodynamics*, Adv. Phys. **65**, 239 (2016).

[52] T. Mori, T. N. Ikeda, E. Kaminishi, and M. Ueda, *Thermalization and prethermalization in isolated quantum systems: A theoretical overview*, J. Phys. B **51**, 112001 (2018).

[53] J. M. Deutsch, *Eigenstate Thermalization Hypothesis*, Rep. Prog. Phys. **81**, 082001 (2018).

[54] J. Berges, Sz. Borsányi, and C. Wetterich, *Prethermalization*, Phys. Rev. Lett. **93**, 142002 (2004).

[55] M. Rigol, V. Dunjko, and M. Olshanii, *Thermalization and its mechanism for generic isolated quantum systems*, Nature **452**, 854 (2008).

[56] G. Biroli, C. Kollath, and A. M. Läuchli, *Effect of rare fluctuations on the thermalization of isolated quantum systems*, Phys. Rev. Lett. **105**, 250401 (2010).

[57] T. N. Ikeda, Y. Watanabe, and M. Ueda, *Eigenstate randomization hypothesis: Why does the long-time average equal the microcanonical average?*, Phys. Rev. E **84**, 021130 (2011).

[58] F. Anza, C. Gogolin, and M. Huber, *Eigenstate thermalization for degenerate observables*, Phys. Rev. Lett. **120**, 150603 (2018), supp. mat., sect. A.

[59] F. Li, V. Y. Chernyak, and N. A. Sinitsyn, *Quantum annealing and thermalization: Insights from integrability*, Phys. Rev. Lett. **121**, 190601 (2018).

[60] G. Dvali and C. Gómez, *Quantum compositeness of gravity: Black holes, AdS and inflation*, J. Cosmol. Astropart. Phys. 01 (2014) 023.

[61] D. J. Gross and A. Neveu, *Dynamical symmetry breaking in asymptotically free field theories*, Phys. Rev. D **10**, 3235 (1974).

[62] R. F. Dashen, B. Hasslacher, and A. Neveu, *Semiclassical bound states in an asymptotically free theory*, Phys. Rev. D **12**, 2443 (1975).

[63] A. V. Manohar, *Large N QCD*, arXiv:hep-ph/9802419.

[64] S. R. Coleman, *1/N*, Report No. SLAC-PUB-2484, 1980.

[65] F. Gelis, E. Iancu, J. Jalilian-Marian, and R. Venugopalan, *The color glass condensate*, Annu. Rev. Nucl. Part. Sci. **60**, 463 (2010).

[66] G. 't Hooft, *A planar diagram theory for strong interactions*, Nucl. Phys. **B72**, 461 (1974).

[67] T. D. Lee and Y. Pang, *Nontopological solitons*, Phys. Rep. **221**, 251 (1992).

[68] S. R. Coleman, *Q-Balls*, Nucl. Phys. **B262**, 263 (1985).

[69] A. Kusenko, *Small Q balls*, Phys. Lett. B **404**, 285 (1997).

[70] G. R. Dvali, A. Kusenko, and M. E. Shaposhnikov, *New physics in a nutshell, or Q-ball as a power plant*, Phys. Lett. B **417**, 99 (1998).

[71] C. Barcelo, S. Liberati, and M. Visser, *Analogue gravity*, Living Rev. Relativity **8**, 12 (2005).

[72] *Quantum analogues: From phase transitions to black holes & cosmology*, edited by R. Schützhold and W. G. Unruh, Springer Lecture Notes in Physics, Vol. 718 (Springer, Berlin, Heidelberg, 2007).

[73] *Artificial black holes*, edited by M. Novello, M. Visser, and G. Volovik (World Scientific, Singapore, 2002).

[74] U. Leonhardt and P. Piwnicki, *Relativistic effects of light in moving media with extremely low group velocity*, Phys. Rev. Lett. **84**, 822 (2000).

[75] M. Visser, *Comment on "Relativistic effects of light in moving media with extremely low group velocity"*, Phys. Rev. Lett. **85**, 5252 (2000).

[76] U. Leonhardt and P. Piwnicki, *Reply to the "Comment on 'Relativistic effects of light in moving media with extremely low group velocity' " by M. Visser*, Phys. Rev. Lett. **85**, 5253 (2000).

[77] R. Schützhold, G. Plunien, and G. Soff, *Dielectric black hole analogues*, Phys. Rev. Lett. **88**, 061101 (2002).

[78] F. Belgiorno, S. L. Cacciatori, M. Clerici, V. Gorini, G. Ortenzi, L. Rizzi, E. Rubino, V. G. Sala, and D. Faccio, *Hawking radiation from ultrashort laser pulse filaments*, Phys. Rev. Lett. **105**, 203901 (2010).

[79] W. G. Unruh and R. Schützhold, *Hawking radiation from "phase horizons" in laser filaments?*, Phys. Rev. D **86**, 064006 (2012).

[80] G. Dvali and A. Kovtun, in preparation.

[81] A. Kitaev, *A simple model of quantum holography*, Talks at KITP, 2015 http://online.kitp.ucsb.edu/online/entangled15/kitaev/ (part 1); https://online.kitp.ucsb.edu/online/entangled15/kitaev2/ (part 2).

[82] J. Maldacena, S. H. Shenker, and D. Stanford, *A bound on chaos*, J. High Energy Phys. 08 (2016) 106.

[83] S. H. Shenker and D. Stanford, *Black holes and the butterfly effect*, J. High Energy Phys. 03 (2014) 67.

[84] O. Kaikov, *Scrambling burdened by memory*, in preparation.

[85] G. Dvali and M. Panchenko, *Black hole type quantum computing in critical Bose-Einstein systems*, arXiv:1507.08952.

[86] G. Dvali and M. Panchenko, *Black hole based quantum computing in labs and in the sky*, Fortschr. Phys. **64**, 569 (2016).

[87] G. Dvali and C. Gómez, *Black hole's information group*, arXiv:1307.7630.

[88] G. Dvali, C. Gómez, and S. Zell, *Quantum break-time of de Sitter*, J. Cosmol. Astropart. Phys. 06 (2017) 028.

[89] G. Dvali and S. Zell, *Classicality and quantum break-time for cosmic axions*, J. Cosmol. Astropart. Phys. 07 (2018) 064.

[90] A. Kovtun and M. Zantedeschi, *Breaking BEC*, J. High Energy Phys. 07 (2020) 212.

[91] A. Kovtun and M. Zantedeschi, *Breaking BEC: Quantum evolution of unstable condensates*, Phys. Rev. D **105**, 085019 (2022).

[92] M. Bukov and P. Weinberg, *QuSpin: A Python package for dynamics and exact diagonalisation of quantum many body systems part I: Spin chains*, SciPost Phys. **2**, 003 (2017).

[93] M. Bukov and P. Weinberg, *QuSpin: A Python package for dynamics and exact diagonalisation of quantum many body systems. Part II: Bosons, fermions and higher spins*, SciPost Phys. **7**, 020 (2019).

[94] M. Bukov, M. Schmitt, and P. Weinberg, QuSpin documentation, http://quspin.github.io/QuSpin/.

[95] S. Sachdev and J. Ye, *Gapless spin-fluid ground state in a random, quantum Heisenberg magnet*, Phys. Rev. Lett. **70**, 3339 (1993).

[96] O. Kaikov, *Is the Eigenstate Thermalization Hypothesis equivalent to fast scrambling?*, in preparation.

[97] F. Anza, C. Gogolin, and M. Huber, *Eigenstate thermalization for degenerate observables*, Phys. Rev. Lett. **120**, 150603 (2018).

[98] M. Rigol and M. Srednicki, *Alternatives to eigenstate thermalization*, Phys. Rev. Lett. **108**, 110601 (2012).

[99] C. Murthy and M. Srednicki, *Bounds on chaos from the Eigenstate Thermalization Hypothesis*, Phys. Rev. Lett. **123**, 230606 (2019).

[100] C. Murthy, A. Babakhani, F. Iniguez, M. Srednicki, and N. Y. Halpern, *Non-abelian Eigenstate Thermalization Hypothesis*, Phys. Rev. Lett. **130**, 140402 (2023).

[101] M. V. Berry, *Regular and irregular semiclassical wavefunctions*, J. Phys. A **10**, 2083 (1977).

[102] M. V. Berry, *Chaotic behaviour of deterministic systems*, Les Houches XXXVI, eds. G. Iooss, R. H. G. Helleman, and R. Stora (North-Holland, Amsterdam, 1983), course 3: Semiclassical mechanics of regular and irregular motion.

[103] J.-S. Caux and J. Mossel, *Remarks on the notion of quantum integrability*, J. Stat. Mech. **02**, P02023 (2011).

[104] R. Steinigeweg, J. Herbrych, and P. Prelovšek, *Eigenstate thermalization within isolated spin-chain systems*, Phys. Rev. E **87**, 012118 (2013).

[105] W. Beugeling, R. Moessner, and Masudul Haque, *Finite-size scaling of eigenstate thermalization*, Phys. Rev. E **89**, 042112 (2014).

[106] I. Bloch, *Ultracold quantum gases in optical lattices*, Nat. Phys. **1**, 23 (2005).

[107] I. Bloch, J. Dalibard, and W. Zwerger, *Many-body physics with ultracold gases*, Rev. Mod. Phys. **80**, 885 (2008).

[108] I. Bloch, J. Dalibard, and S. Nascimbène, *Quantum simulations with ultracold quantum gases*, Nat. Phys. **8**, 267 (2012).

[109] J. F. Wienand, S. Karch, A. Impertro, C. Schweizer, E. McCulloch, R. Vasseur, S. Gopalakrishnan, M. Aidelsburger, and I. Bloch, *Emergence of fluctuating hydrodynamics in chaotic quantum systems*, arXiv:2306.11457.

[110] H. A. Gersch and G. C. Knollman, *Quantum cell model for bosons*, Phys. Rev. **129**, 959 (1963).

[111] M. P. A. Fisher, P. B. Weichman, G. Grinstein, and D. S. Fisher, *Boson localization and the superfluid-insulator transition*, Phys. Rev. B **40**, 546 (1989).

[112] E. Witten, *Superconducting strings*, Nucl. Phys. **B249**, 557 (1985).

[113] R. L. Davis and E. P. S. Shellard, *Cosmic vortons*, Nucl. Phys. **B323**, 209 (1989).

[114] R. A. Battye, S. J. Cotterill, and J. A. Pearson, *A detailed study of the stability of vortons*, J. High Energy Phys. **2022**, 5 (2022).

Acknowledgements

First and foremost I would like to express my gratitude to Gia Dvali for the support and supervision that he has provided over the past years. I am grateful to him for the opportunity to freely explore the topics I found interesting and for the many discussions in which he shared his deep insights and intuition with me. His focus to understand and explain physics from the perspective of simple fundamentals has deeply shaped the way I approach research.

I am very grateful to Georg Raffelt for his support as a member of the advisory panel. I would like to thank him for the many valuable insights into the academic world that he provided.

It is also a pleasure to thank all my collaborators from both completed and ongoing projects. I am grateful to them for the countless insights and numerous fruitful discussions.

Many thanks go out to the former and current members of the group, who developed a productive working atmosphere, and with many of whom I have had the pleasure to discuss matters related and unrelated to physics. In particular I would like to thank Ana Alexandre, Maximilian Bachmaier, Lasha Berezhiani, Giordano Cintia, Giacomo Contri, Lukas Eisemann, Manuel Ettengruber, Anna Jankowsky, Georgios Karananas, Emmanouil Koutsangelas, Florian Kühnel, Andrei Kovtun, Marco Michel, Otari Sakhelashvili, Goran Senjanović, Dimitris Skliros, Anja Stuhlfauth, Juan Sebastián Valbuena-Bermúdez, Max Warkentin and Michael Zantedeschi.

A special word of gratitude is due to all who have supported me in the search for a postdoc position, in particular Gia Dvali, Georg Raffelt, Milada Margarete Mühlleitner and Lasha Berezhiani. Moreover, I am grateful to Gia Dvali, Andreas Weiler, Allen Caldwell and Georg Raffelt for being part of my PhD committee. Furthermore, I would like to thank Andreas Weiler for agreeing to be the second referee of my dissertation.

I would like to express my gratitude to Corinna Brunnlechner, Vera Kudrin, Alexandra Stankovic, Frank Steffen and Herta Wiesbeck-Yonis for the outstanding administrative support. I am indebted to Maximilian Bachmaier and Marco Michel for their help with the hardware for numerical simulations.

I would like to thank the Ludwig Maximilian University of Munich (LMU) for the many interesting seminars, schools, block courses and lectures that were and continue to be organized. Furthermore, I am obliged to the International Max Planck Research School on Elementary Particle Physics at the Max Planck Institute for Physics for the academic and financial support.

It is a pleasure to thank Houssem Amami, whom I have had the privilege to co-supervise for his Master's thesis. Moreover, I am grateful to the students at LMU who remained highly motivated despite the circumstances of the COVID-19 pandemic and made it a pleasure to give tutorials.

Last but not least, I am incredibly grateful to my family. I would like to thank my loving parents for the unconditional moral support and encouragement throughout all this time. Finally, I would like to thank my wonderful wife for her scientific and mental support, advice, honesty, optimism, positivity and love.

Thank you.